Influence of Nano- and Microtopography on the Attachment Behavior of Pseudomonas fluorescens

Inaugural-Dissertation
to obtain the academic degree
Doctor rerum naturalium (Dr. rer. nat)

submitted to the Department of Biology, Chemistry, Pharmacy
of Freie Universität Berlin

by

Jan David Schütter

2023

This work was accomplished from 01.01.2018 to 31.08.2023 under the supervision of Prof. Anna A. Gorbushina at the Federal Institute for Materials Research and Testing (BAM) in Berlin.

1st Reviewer: Prof. Dr. Anna A. Gorbushina

2nd Reviewer: Prof. Dr. Jens Rolff

Date of defense: 27.2.2024

Acknowledgements

Declaration of Independence

I hereby declare that I have completed the submitted dissertation independently and without the use of sources and aids other than those indicated. I have marked as such all statements that are taken literally or in content from other writings. This dissertation has not yet been presented to any other examination authority in the same or a similar form and has not yet been published.

Summary

Bacteria mostly prefer to live as biofilms on surfaces rather than in flowing environments. However, biofilms are mostly unwanted by humans and preventing possibilities besides biocides and antibiotics are urgently needed. One strategy is to prevent the bacteria directly from attaching to the substrate.

This study aims to investigate the effect of nano- and microstructures on bacterial attachment and pursues two approaches whether such surfaces reduce bacterial attachment under flow conditions. The first approach involves ZnO nanorods to design surfaces with varying topographies in the nano- and micrometer range, while the second uses 3D printed microstructures to induce microflows that repel bacteria from the surface. The tailored substrates were integrated into a specially developed flow chamber and exposed to a flowing suspension of *P. fluorescens* under in-situ conditions. Additionally, the attached bacteria were subjected to higher shear forces by increased flow velocities. For evaluation, the attached bacteria were imaged using fluorescence microscopy and automated counted on a single-cell level. The cell counts were compared between different substrates and a control surface to assess the effectiveness of the surfaces in preventing bacterial attachment. Lower cell numbers indicated a surface that better prevented bacterial attachment.

However, it was found that none of the investigated surfaces reduced the attachment of *P. fluorescens.* These findings and additionally made observations have the potential to alter the current perspective of the believed capability of nano and microstructures for preventing microbial attachment. Remarkably, it was found that although accompanying computational fluid dynamic simulations predicted uniform flows in the channels, anomalies in the flows occurred, resulting in uneven distribution of the bacteria. Furthermore*, P. fluorescens* revealed the ability to attach to any surface studied and rapidly establish irreversible attachment there. Thus, this study also suggests using those microorganism types that perform best in attachment for benchmarking surfaces that are intended to have a bacteria-repellent effect in the future.

During the project, a method for a lipopolysaccharide encapsulated polystyrene (LPS-PS) microparticle system was developed as a further approach. The easy-to-use method was developed to mimic bacteria for attachment studies. A variety of analytical techniques were used to detect the LPS on the polystyrene microparticles. Among others, a procedure for labeling the particles for fluorescence microscopy is presented. The data from the analyses offers a reference for future applications of the LPS-PS microparticles, whose use goes far beyond bacterial attachment studies; they are attractive for vaccine research and serological tests.

Zusammenfassung

Bakterien bevorzugen in einem Biofilm auf Oberflächen zu leben, statt frei in fließenden Umgebungen. Biofilme sind jedoch für den Menschen meist unerwünscht und Möglichkeiten diese, statt mit dem Einsatz von Bioziden und Antibiotika, zu verhindern, werden dringend benötigt. Eine Strategie besteht darin, die Bakterien direkt daran zu hindern, sich an das Substrat anzuheften.

Diese Studie zielt darauf ab, die Wirkung von Nano- und Mikrostrukturen auf die bakterielle Anhaftung zu untersuchen und verfolgt zwei Ansätze, ob solche Oberflächen die bakterielle Anhaftung unter Strömungsbedingungen reduzieren. Der erste Ansatz verwendet ZnO-Nanostäbchen, um Oberflächen mit unterschiedlichen Topografien im Nano- und Mikrometerbereich zu gestalten, während der zweite Ansatz 3D-gedruckte Mikrostrukturen verwendet, um Mikroströmungen zu induzieren, die Bakterien von der Oberfläche abweisen. Die speziell angefertigten Substrate wurden in eine eigens entwickelten Strömungskammer integriert und einer fließenden Suspension von *P. fluorescens* ausgesetzt um so eine in-situ Analyse zu ermöglichen. Außerdem wurden die anhaftenden Bakterien höheren Scherkräften, durch erhöhte Strömungs-geschwindigkeiten, ausgesetzt. Zur Auswertung wurden mit Hilfe der Fluoreszenzmikroskopie Bilder der angehefteten Bakterien aufgenommen und diese automatisch auf Einzelzellniveau ausgezählt. Die Zellzahlen wurden zwischen verschiedenen Substraten und einer Kontrollfläche verglichen, um so zu bewerten, wie wirksam die Oberflächen eine Anhaftung von Bakterien verhindern. Geringere Zellzahlen wiesen dabei auf eine Oberfläche hin, die das Anhaften von Bakterien besser verhinderte.

Es wurde jedoch festgestellt, dass keine der untersuchten Oberflächen die Anhaftung von *P. fluorescens* reduzierte. Diese Ergebnisse und zusätzliche Beobachtungen haben das Potenzial, die derzeitige Sichtweise auf die vermutete Wirkung von Nano- und Mikrostrukturen gegenüber Mikroben zu verändern. Bemerkenswerterweise wurde festgestellt, dass Anomalien in den Strömungen auftraten, die zu einer ungleichmäßigen Verteilung der Bakterien führten. Dieses Verhalten widerspricht computergestützten fluiddynamischen Simulationen, die begleitend durchgeführt wurden: diese prognostizierten gleichmäßige Strömungen in den Kanälen. Darüber hinaus zeigte sich, dass *P. fluorescens* die Fähigkeit besitzt, sich an jede untersuchte Oberfläche anzuheften und dort schnell eine irreversible Anhaftung zu entwickeln. Daher schlägt diese Studie auch vor, in Zukunft diejenigen Mikroorganismenarten, die am besten anhaften, zur Messung der bakterienabweisenden Wirksamkeit von Oberflächen zu verwenden.

Im Rahmen des Projekts wurde zusätzlich eine Methode für ein Lipopolysaccharid- verkapseltes Polystyrol (LPS-PS) Mikropartikel-system entwickelt. Die einfach anzuwendende Methode wurde

entwickelt, um Bakterien für Anhaftungsstudien zu imitieren. Zum Nachweis des LPS auf den Polystyrol-mikropartikeln wurden verschiedene Analysetechniken eingesetzt. Unter anderem wird ein Verfahren zur Markierung der Partikel für die Fluoreszenzmikroskopie vorgestellt. Die Analysedaten bieten eine Referenz für künftige Anwendungen der LPS-PS Mikropartikel, deren Einsatz weit über Studien zur Anheftung von Bakterien hinausgeht; sie sind attraktiv für die Impfstoffforschung und serologische Tests.

Outline

List of Abbreviations

AFM	Atomic force microscope
AFM-IR	Infrared Nanospectroscopy
ANOVA	Analysis of variance
aNR-glass	Coverslip with arrays of nanorods and a zinc oxide thin film in between
CFD	Computational fluid dynamics
DF	Degree of Freedom
diH_2O	Deionized water
DLE	Deep-level emission
EPS	Extracellular polymeric substance
FITC	Fluorescein isothiocyanate
GFP	Green fluorescent protein
LPS	Lipopolysaccharide
LPS-PS	Lipopolysaccharide encapsulated polystyrene
iaDS	Data set of bacterial numbers in an image area
MMM	Minimum Mineral Medium
MPL	Multiphoton lithography
NBE	Near-band edge excitonic emission
NR-glass	Coverslip with a homogeneous layer of zinc oxide nanorods
OD_{600}	Optical density at 600 nm
PBS	Phosphate-buffered saline
PDMS	Polydimethylsiloxane
PE	Polyethylene
PET	Polyethylene terephthalate
PS	Polystyrene
rDS	Data set of bacterial numbers of one replicate
SEM	Scanning electron microscope
stDS	Data set of bacterial numbers of one substrate type
TF-glass	Coverslip with a homogeneous layer of zinc oxide thin film
XPS	X-ray photoelectron spectroscopy

1   Motivation and Aim of the Project

The formation of a biofilm with bacteria often has problematic implications for humans (Jia et al., 2019). In different fields of industry, biofilms cause damage to equipment and infrastructure, leading to major economic losses. One phenomenon is microbiologically influenced corrosion, which is the deterioration of metals due to direct or indirect microbial activity. Another phenomenon is biofouling, which is the settlement of organisms of different sizes on solid surfaces causing limited functionality of the device or component (de Carvalho, 2018). In the food industry, biofilms are associated with food spoilage and foodborne diseases (Rather et al., 2021). In human healthcare, biofilms affect the functionality of medical implants and are associated with bacterial infections (Yu, Wu and Chen, 2015). A common treatment is the use of biocides and antibiotics. However, their employment leads to unwanted consequences, such as the development of antibiotics resistances (Sharma, Misba and Khan, 2019). Therefore, solutions to control biofilm formation are needed. The development of a biofilm is a stepwise process, which at an early stage is characterized by the initial attachment of bacteria from the environment to the substrate (Garrett, Bhakoo and Zhang, 2008). Various approaches solving the problem of biofilm formation focus on this early stage. However, no promising solution exists yet. Therefore this study presents alternative experimental strategies which open new perspectives in dealing with biofilms.

An evident approach to reduce or completely prevent the attachment of bacteria is to change the surface properties (Romling and Balsalobre, 2012). These changes can either affect the chemical properties (Wei et al., 2017) or target the structure in the micro- and nanometer range of the surface (Wu et al., 2018). Such surface structure modifications can be nanostructures or microstructures, which range from a few to hundreds of nanometers or micrometers, respectively. Nano- and microstructures can have a direct effect or indirect effect in preventing bacterial attachment (Cheng, Feng and Moraru, 2019). A direct effect acts through a single causal relation of the treatment and the outcome, with the outcome being the bacterial attachment. While for an indirect effect a causal pathway with intermediate factors exists. This means that the treatment leads to a phenomenon which then changes the outcome.

As a direct effect is considered the killing of bacteria by nanostructures that pierce the membrane of attached cells (Linklater et al., 2021). Other direct effects act via altered physicochemical forces at nanosurfaces or cell membrane deformation (Cheng, Feng and Moraru, 2019). Nevertheless, doubts have arisen recently whether these direct effects exist or whether their observations are a

consequence of the experimental method and cannot be transferred to real situations in nature (Luan et al., 2018; Senevirathne et al., 2021; Valiei et al., 2022).

The reason why many studies on bacterial attachment should be viewed critically is the experimental procedure (Busscher and van der Mei, 1995). During the sample preparation for ex-situ evaluation, which is the evaluation of bacterial attachment after the experiment, large forces occur that can detach bacteria. Experimental approaches with "washing" or "slightly rinsing" the sample cause phase boundaries, which exert high forces while moving over the surface (Bos, van der Mei and Busscher, 1999). Such a phase boundary is the evaporation front that occurs during surface drying. Suppose a phase boundary detaches bacteria before they are evaluated. In that case, an underestimation of the actual bacterial count is the consequence, leading to an exaggerated impression of the surfaces' preventing properties. Although this problem has been known for more than 20 years, many present studies still use ex-situ experimental approaches (Luan et al., 2018). The reason for applying an ex-situ evaluation is its simplicity compared to a laborious in-situ evaluation (Busscher and van der Mei, 2006). For in-situ evaluation, flow chambers are state-of-the-art. They allow the observation of the attached cells during the experiment by means of light microscopy. Today, we face the situation that many studies carried out in the past had an ex-situ approach which means they are of poor significance. A systematic investigation of nanostructures and microstructures is still pending (Hawi et al., 2022).

An indirect effect of microstructures originates from micro-hydrodynamic situations in the vicinity of microstructures in flowing environments (Schumacher et al., 2008; Weisse et al., 2011; Halder et al., 2013; Lee et al., 2013; Choi et al., 2015; Choi et al., 2018b). In this case, the microstructures act as obstacles in the bulk volume flow and cause turbulences or regions of highly fluctuating wall shear stress, which are considered to repel the bacteria before they can settle. Investigating effects of micro-hydrodynamics can be done precisely with a flow chamber, which is yet another advantage of this device. However, computational fluid dynamic (CFD) simulations are required to link the micro-hydrodynamics with the microscopic observations of bacterial behavior. Flowing environments where micro-hydrodynamic situations can occur are so important because they occur in many applications, such as pipelines, and in the human body. Moreover, many aqueous environments in nature are in motion at the scale of bacteria. Therefore, studying bacterial attachment in flowing environments is more relevant than bacterial attachment in static, non-moving environments.

This project aims to investigate the direct and indirect influences of nano- and microstructures at the stage of initial bacterial attachment. This topic is discussed in the first two parts of this paper. This will be the focus of parts I and II of this dissertation: the first one focuses on direct influences, the second one on indirect influences. For the first part, surfaces with a homogeneous nano-roughness and surfaces with equally alternating smooth and nano-roughened areas were created. Zinc oxide (ZnO)

nanorods and ZnO thin film deposition were chosen to create these surfaces, as both methods are robust, easy to handle, and applicable on large scales. For the second part, CFD simulations on simple cuboidal-shaped microstructures were done. The findings were used to create microstructures with high definition by multiphoton lithography (MPL). An in-situ experimental procedure was applied in both parts using a custom-built flow chamber. Specifically, this means that both surfaces with ZnO structures and MPL printed structures were exposed to a flowing bacterial suspension. Subsequently, the attachment and retention of the bacteria could be determined.

The model bacterium *Pseudomonas fluorescens* SBW25 was used for the experiments since it is a pioneer colonizer and has already been used in other attachment studies. The bacterial attachment on a single-cell level was evaluated by fluorescence microscopy in-situ. The comparison of cell numbers on the different surfaces was used to conclude the effectiveness of preventing bacterial attachment. In summary, the project will contribute to elucidate the factors that govern initial bacterial attachment with a methodological approach that reflects the situation in industrial and natural habitats of microorganisms.

Part III of this dissertation highlights a further approach of the project. Approaches to mimic bacteria were made in past studies in bacterial adhesion experiments. For this purpose, the adhesion of polystyrene beads with the size of bacteria was compared to the adhesion of bacteria (Sjollema, Busscher and Weerkamp, 1988; Yang et al., 1999). Also, the surface of polystyrene beads was altered with chemical groups typical of bacteria (Mercier-Bonin et al., 2009) to create a system that does not require the cultivation of bacteria. However, it became evident that such model systems are still not sufficiently designed to mimic bacteria. Therefore, a step further was taken in this project and within the surface of polystyrene microparticles, LPS was incorporated. LPS represents more than three-quarters of the bacterial surface (Gnauck, Lentle and Kruger, 2016). The aim is to develop a particle system that more closely resembles real bacteria and can be used for adhesion tests.

2   Scientific Background

2.1 Biofilm Formation and Prevention

Biofilms are assemblies of microbial cells enclosed in a matrix, adhering to surfaces (Flemming and Wingender, 2010). The matrix consists mainly of polysaccharides and fulfills several functions. Among others, it improves adhesion to the substrate, protects the microorganisms, and is involved in metabolism. The matrix material is produced by the cells and is called extracellular polymeric substance (EPS) (Flemming and Wingender, 2010).

Biofilms can develop on almost any surface and are ubiquitously distributed (Donlan, 2002). They occur on living tissue, implants and in oil and potable water pipes. Biofilms are undesirable, with a few exceptions, such as in biomining, where microorganisms break down ores (Schippers et al., 2014). In the medical field, they are associated with infections (Fux et al., 2005), and in the industrial field, they cause material damage that can lead to total system failure. One term in this context is microbially influenced corrosion, which specifically describes the deterioration of metal due to microbial activity (Beech and Sunner, 2004).

The development of biofilms follows a stepwise process (Garrett, Bhakoo and Zhang, 2008) and is schematically presented in Figure 2-1. Before planktonic microbial cells from the fluid phase, often an aqueous liquid, adhere to the substrate, a conditioning layer has already formed. In this layer, organic and inorganic particles are accumulated, which adsorb by physical forces or sink to the substrate by gravitation. Bacteria can now adhere to the conditioned surface or to already attached cells; the latter is called cohesion (Garrett, Bhakoo and Zhang, 2008).

Initial adhesion is a step governed by physicochemical forces between the substrate and cell surfaces (2 in Figure 2-1). Besides surface charges, ionic strength and flow conditions also play a role (Berne et al., 2018). Many bacteria also possess appendages, such as flagella and pili, which assist them in initial adhesion. If present, the long flagella, which also participate in locomotion, often provide the first contact of the cell with the surface. At this stage, the bacterium is still loosely adhered at the surface and can detach (Conrad et al., 2011). The further fate of the bacterium, which remains in close surface contact, depends on the chemical interactions. If the bacterium can overcome the potential energy barrier, it reaches the deep primary energy minimum and is in direct contact with the substrate surface (Carniello et al., 2018). If not, it remains in the secondary minimum above the surface and rotates or tethers to the flagellum. The so-called tether-coupled bacterium can now use pili, which are able to

penetrate into the first minimum to connect itself with the substrate surface strongly (Carniello et al., 2018).
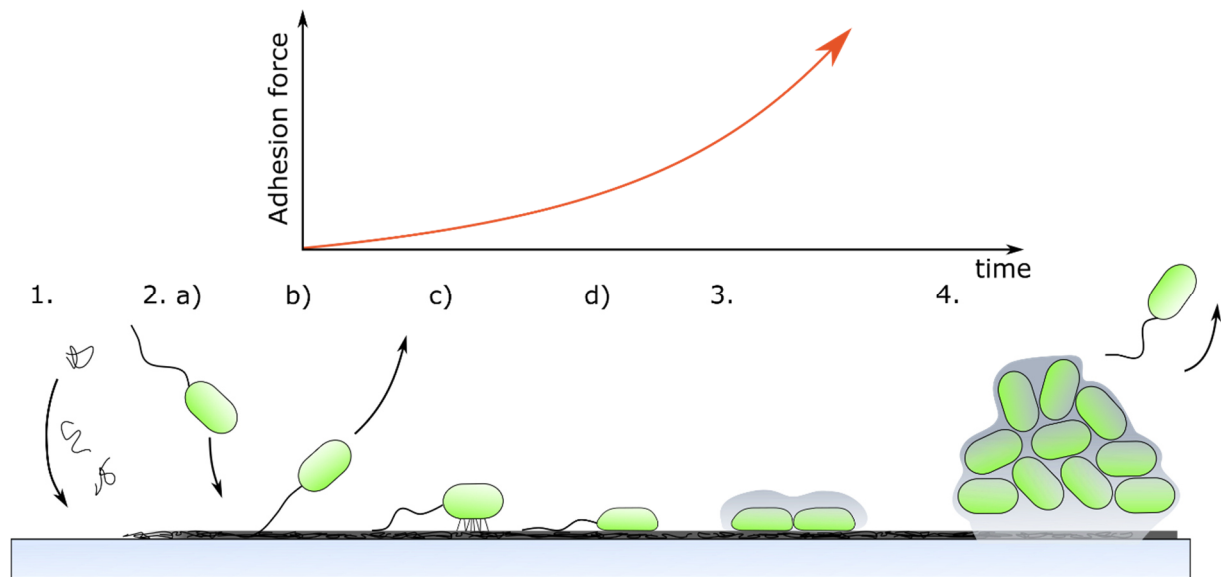
Figure 2-1: The development of a biofilm is stepwise and the adhesion force of adhered bacteria increases with each step. First, inorganic and organic material from the environment accumulates on the substrate and forms a conditioning layer (1). It can contain ions and molecules as well as larger particles. Attachment begins with the initial contact of the bacterium with the surface (2 a). If it has a flagellum, it causes tethering of the bacterium (2 b). Pili enable the energy barrier at the surface to penetrate and, in combination with bond maturing, provide a more irreversible attachment of the cell (2 c). The cell wall deformation flattens the bacterium and increases the contact area between cell and substrate surface (2 d). The now attached cells form an EPS matrix and cell division starts (3). As the cells continue to divide, the biofilm matures, and individual bacteria leave and can repopulate other sites (4). According to Carniello et al. (2018).

Then, a bacterium on the surface undergoes bond-strengthening by forming attractive interactions at connection sites (Busscher et al., 2010). This purely physico-chemical bond-strengthening is the transition of the reversible adhesion to a more irreversible attachment (Carniello et al., 2018). The post-attachment behavior until irreversible attachment of the bacteria is very diverse and depends on the bacteria, flow conditions, and surface properties (Santore, 2022). Common is that this phase generally takes place in the timescale of minutes. After only a few minutes, the adhesion force of bacteria amounts to 0.5–1 nN (Busscher et al., 2010; Aguayo et al., 2015). The adhesion force is further enhanced by the deformation of the cell wall, which flattens the bacterium and presses it closer to the surface (Li et al., 2014). This process increases the contact area between substrate and cell surface and proceeds on the time scale of several minutes to hours. Simultaneously, the release of EPS leads to a fixating slime which also increases the bacterial resistance against detachment forces (Carniello et al.,

2018). Since the bacteria actively contribute, the adhesion to a substrate will be referred to as attachment in the following.

With an irreversibly attached bacterium, the biofilm begins to grow by cell division (3 in Figure 2-1) (Kaplan, 2010). At the same time, the continuously secreted EPS forms the matrix between the cells (Flemming et al., 2016). The matrix can incorporate suspended solids if available in the liquid (Kaplan, 2010). Biofilms form mushroom-like structures to ensure a sufficient supply of nutrients (4 in Figure 2-1). In the final stage of biofilm development, bacterial cells detach into the liquid. These planktonic cells can colonize new surfaces and give rise to a new biofilm. In this way, the cycle of biofilm development is completed (Kaplan, 2010).

In forming a biofilm, the initial attachment stage plays a crucial role (Zhong, Song and Zhou, 2020). Consequently, research strives to elucidate the underlying mechanisms and parameters. However, no consistent answers have been found until now. Indeed, it is a matter of fact that there are many perspectives to consider for bacterial attachment.

One model used to describe physical interactions between cells and surface is the DLVO (Derjaguin-Landau-Verwey-Overbeek) Theory (Hermansson, 1999). It was initially developed to describe the stability of colloidal systems and can be transferred to the microbial system to state whether an interaction is attractive or repulsive. The total net interaction between the particles of the system is the sum of van-der Waals and double layer interactions. The van-der Waals interactions summarize the dipole-dipole interactions between the particles and are attractive. The double layer interactions are usually repulsive and result from electrostatic interaction between the charged particles and their counterions in solution. The mobile counterions form a dense layer around the particles, the Stern layer, and outside a diffuse electrical double layer with restricted mobility. When two particles meet, their double layers repel each other due to repulsive osmotic pressure between the counterions (Hermansson, 1999). The total interaction between two particles is characterized by a primary and secondary energy minimum with an energy barrier in between and depends on the distance (Elimelech et al., 1995). In the primary energy minimum the particles are in contact and in the secondary they are stabilized as a colloid. The energy barrier can be reduced by an increased ion concentration. At some point the particles can overcome the barrier and aggregate, which leads to precipitation (Elimelech et al., 1995).

However, the predictions of DVLO Theory regularly diverged from the results obtained with bacteria experiments (Hermansson, 1999). Therefore van Oss (1989) added a term with acid-base interactions to the overall interactions leading to the extended DLVO theory (van Oss, 1993). The latter was

introduced to account for the influence of Lewis acids (electron acceptor) and Lewis bases (electron donor) in the medium. Acid-base interactions can be attractive or repulsive.

From these models, it can be deduced that the properties of the aqueous medium matter for the attachment of bacteria. Indeed, it has been found a temperature dependency (Gallardo-Moreno et al., 2002), pH dependency (Sheng, Ting and Pehkonen, 2008), and ion concentration dependency (Rijnaarts et al., 1999). Besides the medium, the surface governs bacterial attachment. Besides the influence of the substrate material (Meinders, van der Mei and Busscher, 1995), it was observed that single molecular hydrophilic and hydrophobic layers had an influence on bacterial attachment (Boks et al., 2008). Furthermore, their attachment could be changed with defined positive and negative surface charges (Böhmler et al., 2015).

The observed attachment of microorganisms often deviates from the predictions of the above described models (Hori and Matsumoto, 2010). These approaches have demonstrated their effectiveness in studying specific groups of strains (Bos, van der Mei and Busscher, 1999). However, they have not yet produced a universal explanation that encompasses all aspects of microbial attachment across all strains. In fact, homogeneous bare surfaces assumed in this model do not exist in reality (Hori and Matsumoto, 2010). They are often heterogeneous in structures and composition on the dimension of the bacteria and covered by a conditioning layer. Moreover, the cell surface of bacteria is chemically and structurally heterogeneous. Contributing to these characteristics are surface proteins such as pili and other so-called adhesins (Klemm and Schembri, 2000). Thus, the pili are able to penetrate the bilayer with its small diameter. They take advantage of the fact that the energy barrier of the double layer interaction can be reduced by a smaller radius of the contact region (Kimkes and Heinemann, 2020). In gram-negative bacteria, lipopolysaccharides (LPS) are an outer membrane component (El-Taboni et al., 2020). Another factor that is not satisfactorily represented by DLVO and extended DLVO theory is physical forces due to the flowing medium, such as shear stress, as studies from Katsikogianni and Missirlis (2010) suggest. In summary, the intricate surface of bacterial cells, coupled with the usual complex nature of the substrate and physical forces in the medium, signifies restrictions in creating a cohesive theory for bacterial attachment (Cheng, Feng and Moraru, 2019). Thus, when it comes to preventing biofilm formation, focusing research on these three aspects is required.

The formation of a biofilm is, in most cases, unwanted (Simões, Simões and Vieira, 2010). It is believed that the most effective method of controlling biofilms is to prevent settlement and forming colonies of several cells. Once the bacteria have firmly attached to the surface and produced EPS, efforts to remove the biofilm are elaborate. Then the device needs mechanical treatment to clean it, or chemicals such as antibiotics are used. At this point, it should be noted that biofilms are much more

resistant to these substances than individual cells (Koo et al., 2017). Surface modifications can potentially prevent the initial attachment of bacteria or directly target single colonizing bacteria (Cheng, Feng and Moraru, 2019). As such a surface modification, the incorporation of biocidal compounds on the surface or in reservoirs from which they can be selectively released has been studied for a long time (Koo et al., 2017). However, questionable efficiency and potential deleterious side effects have raised doubts about this approach.

A different strategy in combating bacterial settlement pursues topographical surface modifications (Li et al., 2021). This modification aims to tailor roughness, geometry, and other physical configurations in the nano and micrometer scale, which strongly determine the attachment behavior of microorganisms.

2.2 Bacterial Attachment on Micro- and Nanostructures

The topography, i.e. the relief of a surface, is difficult to classify (Gadelmawla et al., 2002). Unless it is smooth or can be defined by regular periodic features, such as spacing and height difference, few possibilities remain to describe a complex three-dimensional heterogeneity and thus make surface topographies comparable with each other. One possible way to deal with this problem is to use roughness parameters. The large number of parameters illustrates that there is no universal approach quantifying the roughness of a surface with one value. A common roughness parameter is the root mean square roughness. R_q is defined as

$$R_q = \sqrt{\frac{1}{l} \int_0^l z(x)^2 dx}$$

(1)

with z being the height at position x in a cross section of length l. In experiments on the adsorption behavior of bacteria, the arithmetic average height roughness is often used (Bollenl, Lambrechts and Quirynen, 1997). However, roughness can only describe the height difference (Crawford et al., 2012). It is not suitable for describing spatial information and geometric details. This issue could be one of the reasons why studies report contradictory results regarding the influence of roughness on bacterial attachment.

Since roughness parameters are insufficient to describe a surface's topography, an increasing number of studies use surfaces with defined tailored topography (Cheng, Feng and Moraru, 2019). A repetitive nano- and microtopography, whose dimensions can be unambiguously described, allows the underlying parameters of bacterial attachment to surface structures to be systematically investigated. A nanotopography ranges in height from a few nm to less than one µm and is smaller than a bacterial

cell. A microtopography has height differences of one or a few hundred μm and can be in the same dimension as cells, which are one μm to a few μm long. To derive parameters regarding bacterial attachment to the topography, defined repetitive nanostructures are often used for a nanotopography and defined microstructures for a microtopography (Wu et al., 2018).

As for publications studying bacterial detachment depending on roughness parameters, no general trend from studies on the attachment of bacteria to defined patterned microstructures could have been concluded so far. The initial attachment of two *Escherichia coli* strains to defined microstructures was investigated by Hsu et al. (2013) and compared to the attachment to a nanoporous and smooth surface. The microstructures were wells with sizes of 500 nm, 1.5 μm, and 2 μm and the same spacings. In the case of the wells, the bacteria of both strains preferentially attached to the surfaces with microstructures than to the smooth control. Furthermore, the authors determined that the bacteria prefer the upper smooth surface between the wells. This finding contradicts the outcome of Perera-Costa et al. (2014), who revealed that *E. coli* preferred the recessed spaces between microstructures. Ge et al. (2015) pointed out that the dimensions of structures influence bacterial attachment. They produced 3 μm high micropillars with a square profile, with the same width and spacing. The attachment of *E. coli* to surfaces with microstructures was reduced for spacings smaller than the bacteria. Micropillars that were larger respectively had a larger spacing than the size of the bacteria, provided increased attachment compared to a smooth control. One possible reason for these contradictory results are the experimental parts (Busscher and van der Mei, 2006). In the experimental procedure ex-situ evaluations are used, which cause high forces that can detach the attached bacteria in a non-controllable way. Since these forces are not quantifiable, they often vary depending on the individual experimentalist's sample handling and are not considered in the methodology (Busscher and van der Mei, 2006).

An emerging field of research are nanostructures, which possibly reduce bacterial attachment or even have a biocidal effect (Luan et al., 2018). The attachment of bacteria to nanostructured surfaces was reduced compared to a smooth or flat control in most studies. However, Luan et al. (2018) stated that many experiments were carried out under conditions that did not allow any conclusions to be drawn about the forces acting on the bacteria. For this reason, care should be taken by drawing a general conclusion from this kind of studies. The authors noted that it is at least safe to conclude that a nanostructured surface facilitates detachment.

A biocidal effect of nanostructures was observed in nature. Instead of preventing *Pseudomonas aeruginosa* cells from attaching, Ivanova et al. (2012) found that the surface of cicada wings destroyed the bacteria. Responsible for this effect were small nanopillars of 200 nm height, 60 nm tip diameter, and 170 nm spacing. The nanopillars killed the bacteria by rupturing the cell membrane. Therefore,

efforts were made to artificially create nanostructures with a bactericidal effect (Elbourne et al., 2019). However, with the advent of possible biocidal nanostructures, another problem arises: the remaining cell material of the lysed bacteria stays on the nanostructures offering an ideal attachment site for new incoming cells (Senevirathne et al., 2021). Hence, the aspect of self-cleaning for biocidal nanostructured surfaces must always be considered. The bactericidal mechanism of action of the nanopillars is still under debate (Valiei et al., 2022). However, recent studies suggest that the ex-situ evaluation is also problematic in studying biocidal effects of nanostructures. This methodology leads to external forces associated with moving air-liquid interfaces which play a role in killing bacteria by nanopillars (Valiei et al., 2022).

In conclusion, the methodological part turns out to be a general problem in studies dealing with aspects of bacterial attachment and biocidal features of nanostructures. Incubating a sample with the substrate surface of interest in a bacterial suspension seems to be an intuitive approach to tackle questions regarding biofilm formation. Depending on the research objective, the bacteria can be in a nutrient medium, the medium can be stirred, or a constant supply of nutrients can be achieved by a continuous flow reactor design (Bos, van der Mei and Busscher, 1999). Usually, the sample is taken after a certain time, "slightly rinsed" or "lightly and carefully cleaned", optionally prepared for an analytical method, and finally examined. During that sample post-treatment occur inevitable liquid-liquid or liquid-gas phase boundaries that move across the substrate surface. As a consequence, artifacts are introduced in the results of such ex-situ studies. Especially liquid-gas phase boundaries cause strong detachment forces that have been calculated to be up to 200 nN (Gomez-Suarez, Busscher and van der Mei, 2001). The detachment force can remove bacteria before they are determined, leading to an underestimation of the attached bacterial count.

In light of Deupree and Schoenfisch (2008) and experiments, it is evident that the adhesion force between bacteria and the substrate increases over time (compare adhesion force vs. time in Figure 2-1). Thus, bacteria may indeed resist the strong detachment forces due to moving phase boundaries. Otherwise, bacterial attachment in ex-situ studies would not have observed attached bacteria. However, at this stage of irreversible attachment, it is no longer possible to speak of the initial attachment of bacteria; instead, the bacteria are in the transition to a biofilm.

One way to overcome the methodological shortcoming of ex-situ evaluation approaches is in-situ measurement using flow chambers (Christersson et al., 1987). Furthermore, such devices offer investigation of biofilm development under controlled hydrodynamics (Senevirathne et al., 2021). These situations have more practical relevance as industrial components, and medical implants are mainly exposed to flowing liquids.

Using flow chambers, the effectiveness of the substrates in preventing bacterial attachment can be either determined from bacterial coverage of the surface or the attached cells can be counted (Wang et al., 2014). Both quantified values allow comparison among studies. The number of attached cells depends on the attachment time and bacterial density of the liquid, hence it is common to use the adsorption rate coefficient (Camper et al., 1993)

$$j = \frac{J}{C_0} = \frac{\text{overall adsorption rate (cells m}^{-2}\cdot\text{s}^{-1})}{\text{bulk fluid cells (cells m}^{-3})}. \tag{2}$$

So far, few studies on the influence of micro and nanostructures on bacterial attachment have been done so. Hizal et al. (2015) investigated the initial attachment of *Staphylococcus aureus* to various 2D structures and 3D nanostructures but observed for all substrate types no differences. In another study, Hizal et al. (2016) evaluated the attachment and retention of non-EPS producing *Staphylococcus epidermidis* and EPS producing *S. aureus* to different Si nanopillars. For both strains, no difference in attachment after 30 min was observed between the nanopillars and a smooth control. Furthermore, the authors concluded that they observed no influence of nanostructures on bacterial attachment. In contrast, previous studies, which had used ex-situ evaluation, had counted fewer bacteria on the nanostructures as the surface-cell linkage is reduced and consequently forces due to sample preparation detach more cells. The implications of microtopographies on bacterial attachment in flowing systems were investigated by Scheuerman, Camper and Hamilton (1998). They employed *Pseudomonas aeruginosa* as well as motile and non-motile *Pseudomonas fluorescens* and fabricated microgrooves that were perpendicular to the flow, 10 µm deep, and 10 to 40 µm wide. The motile bacteria occurred equally on the smooth surfaces and in the trenches. The non-motile bacteria, on the other hand, were more abundant on the smooth surface. Thus, the authors pointed out the importance of the bacteria's locomotion and suggested that the bacteria's mobility predominated physicochemical effects on the attachment behavior. Other studies investigating the bacterial attachment to microstructures with contradictory results found the cause in the different species being employed (Ling, Graham and Cady, 2012; Graham et al., 2013).

2.3 Micro-hydrodynamics and its Influence on Bacterial Attachment

A different approach than directly using nano- and microtopography to control the attachment of bacteria is taken by indirect uses of such structures leading to micro-hydrodynamic situations at the surface (Halder et al., 2021). Vortices, alternating shear stresses on a confined scale, and upward flows are supposed to keep the bacteria away from the surface. Studies on this approach require flow chambers and are few so far.

Observations that fluid micro-hydrodynamics near the surface may affect fouling were done by Petronis et al. (2000). The authors examined the attachment behavior of macrofouling organisms, in this case barnacles, to a pattern of pyramids and riblets of various sizes. A directed investigation of micro-hydrodynamics on a surface with micropillars was made by Weisse et al. (2011). They observed that microparticles in a flow were driven away from the surface and attributed this to "lift forces" induced by the micropillars. Kumar et al. (2012) designed a microfluidic channel with baffles on the sidewalls. These created circular flows in their interspaces. Due to these vortices, biofilm development of *Shewanella oneidensis* at the baffles could be prevented. Micro-hydrodynamic conditions were also assumed to be closely linked with altered biofilm formation of *P. fluorescens* around microposts in a microfluidic channel (Valiei et al., 2012). Lee et al. (2013) attributed a significant role to shear stress distribution and vortex formation in controlling microorganism attachment. Both micro-hydrodynamic effects occurred on a pattern of repeating prisms, oriented transverse to the flow. At the upper ridges of the prisms, the flow velocities were higher, resulting in higher shear stress and thus reducing bacterial attachment. Between the prisms, the authors assumed the formation of vortices that blocked the overflowing liquid. This phenomenon, termed flow separation, disturbed the entry of microorganisms into the valley on the one hand and prevented the export of the remaining microorganisms out of the valley on the other. From these observations, the study concluded that the microstructure patterns designed to control microbial attachment should be optimized for effective local flows (Lee et al., 2013).

The idea of designing microstructures in a systematic manner to improve the effectiveness of local fluid flows was picked up by Halder et al. (2013). They chose different diameters and spacing of wells in the bottom channel wall and investigated how the attachment of *E. coli* differed. The coverage of the bacteria was lowest for the largest diameters of 10 µm and the smallest spacing of 2 µm. The authors assumed the higher wall shear stress zones along the smaller peripheries of the wells being a reason. In a subsequent study, Halder et al. (2014) investigated how individual bacteria behaved in the microfluidic environments developed in the vicinity of wells. They verified "lift forces" by observing bacterial trajectories directed upward from the microstructured surface beneath, while trajectories over a flat surface for comparison showed no upward trends. The authors supported their observations with CFD simulations. Based on the results, they assumed local flow perturbations at the microstructures, which did not exist on the flat surface, causing the "lift forces" (Halder et al., 2014).

Vortices that formed between pyramidal substrate were examined in more detail by Choi et al. (2015). They found that the bulk flow velocity and size influenced microparticle deposition. Particles of 5 µm size were more likely to be deposited in the bottom of the recesses, whereas particles of 2 µm were entrained with the bulk flow. The bulk flow is the main liquid flow apart from sidewalls and obstacles.

Various and more complex microstructures were fabricated by Choi et al. (2018b) and investigated for their antifouling properties resulting from flow behavior near the pattern features. The authors found that the biomimetic Sharklet pattern, which was designed to resemble shark skin, exhibited the best antifouling properties. The Sharklet structure consisted of alternating blocks with a rhombic superstructure of six consecutive blocks with different lengths. The blocks were positioned transverse to the flow and had small, staggered gaps between them. The fluid flowed through the staggered gaps at increased velocities and caused higher shear stresses there (primary flow). Between the triangular Sharklet structures, vortices occur, which had a net upward deflection and thus displaced particles, as well as bacteria, away from the surface (secondary flow). It was hypothesized that both primary and secondary flow contributed to the antifouling properties of the patterned microstructures, with the secondary flow being attributed to a more potent effect.

Most of nowadays studies on micro-hydrodynamics include CFD simulations (Yang et al., 2021). Their implementations are also advantageous because the surface structures can be simulated first and then selected and designed for their effectiveness. In CFD simulations, fundamental mathematical equations, essentially partial differential equations, are solved with numerical methods and algorithms using the calculation power of computers (Tu, Yeoh and Liu, 2018). It involves breaking down the fluid domain into discrete elements to predict the behavior of the fluid and heat within the domain. The simulated results can be used to optimize designs, identify issues, and make informed decisions about fluid systems.

2.4 Aspects of Flow Chamber Construction and Combination with Light Microscopy

A flow chamber, flow cell, or generally flow displacement system allows in-situ observation and evaluation of biofilm development at all stages (Busscher and van der Mei, 2006). They are the methodical means of choice, while procedures with ex-situ evaluation are not advisable since the sample treatment after the colonization experiment can cause uncontrollable biases. Flow chambers are usually combined with light microscopy. A variety of labeling strategies allow the use of fluorescence microscopy.

A special design is the parallel plate flow chamber (Sjollema, Busscher and Weerkamp, 1989). It consists of two plates, at least one of which is made of a transparent material, arranged parallel over each other (Busscher and van der Mei, 2006). The distance between the plates is not more than a few millimeters. Usually it is chosen to be in the order of tenths of a millimeter. The horizontal extension of the plates is much larger than the separating distance. The plates are confined by spacers at the

sides, allowing a liquid to flow between them. For this purpose, the parallel plates are embedded in a casing, with an inlet and outlet. The entire flow chamber can be disassembled and cleaned, or the plates can be replaced with new ones. The transparent plate, usually made of glass, allows observation of the flowing liquid within a field of observation with a microscope. In addition to their function as a flow boundary and window, the plates serve as a substrate. For example, the attachment behavior of cells and biofilm formation of microorganisms can be observed on the substrate.

Microfluidic or lab-on-a-chip devices take a slightly different approach (Kim, Park and Chung, 2012). By means of microfluidics, it is possible to translate conventional laboratory methods into a micrometer scale, thus reducing overall costs and efforts (Bohr, Colombo and Jensen, 2019). Besides biofilm observation (Pousti et al., 2018), it offers many other possible applications (Squires and Quake, 2005). Microfluidic devices are often made of polydimethylsiloxane (PDMS) and are equipped with channels with cross sections of 10 µm - 100 µm (Wu et al., 2013). PDMS microfluidic devices are processed with lithographic methods such as photolithography and soft lithography. The production starts with a master mold fabricated by using photolithography. In this process, a photoresist is coated onto a silicon wafer and irradiated with a photomask in a defined manner. After removing the photoresist, which has not crosslinked, the negative of the flow chamber channels and possible geometries are cured in an oven. In the second step, soft lithography is applied. Therefore, PDMS precursors are cast in the master mold and after curing, the PDMS positive is ready for bonding (Wu et al., 2013).

By using one master mold, many microfluidic elements can be replicated (McDonald et al., 2000). The PDMS replicas have an inlet and outlet. The channels in between have only three walls as a result of the manufacturing process. Many materials can serve as the fourth wall, like polystyrene, polyethylene, silicon, and glass. A connection between the PDMS and the glass, which additionally seals the microfluidic replica, can be achieved by PDMS bonding (Duffy et al., 1998). For bonding, the surfaces to be joined are activated in an oxygen plasma. This treatment converts $-Si(CH_3)_2O-$ groups of PDMS to $-O_nSi(OH)_{4-n}$ at the surface. On the counterpart, functional polar oxygen groups, such as OH groups, are introduced. The surface of the PDMS part and counterpart are joined by a condensation reaction which forms (Si–O–Si) bonds. Usually, a coverslip is used as a bonding counterpart for the final PDMS microfluidic device as it offers advantages for light microscopic applications (Duffy et al., 1998).

The inlet and outlet of the flow chamber or microfluidic systems, respectively, are connected to different equipment (Busscher and van der Mei, 1995). A pulse-free pump provides a continuous supply of bacterial suspension, nutrition medium, buffer, or cleaning solution via incompressible tubing. A valve can be placed between the pump and the inlet to allow switching between solutions. The outlet is connected via tubing to a collection vessel. Care must be taken to ensure complete tightness throughout the assembly; otherwise, the system will draw in air (Gomez-Suarez, Busscher

and van der Mei, 2001). Air bubbles in the system provide moving liquid-air phase boundaries that can detach microorganisms, as described above.

The flow behavior in parallel plate flow chambers and microfluidic systems is similar (Brewer and Bianco, 2008). Due to the approaches' geometry, the flow is laminar (Busscher and van der Mei, 2006). Nevertheless, channel shape and cross section affect important parameters such as flow velocity and shear stress acting on the microorganisms. The flow rate specification, which is often determined by the pump settings, has limited significance. More precisely, velocity profiles and the shear stresses acting on the microorganisms must be presented. These values allow comparison with other experimental systems (Busscher and van der Mei, 2006).

Flow chambers with a thin channel are suitable for combination with light microscopy. Small wall distance ≤100 μm enables the use of small working distance objectives and imaging of both the top and bottom wall (Choi et al., 2018a). Small working distance objectives have high numerical apertures, which increase the resolution in the field of view; the higher the numerical aperture, the better individual spots can be identified from each other. Thus, individual cells can also be distinguished from each other more clearly. However, these objectives require a special glass with a thickness of 0.17 mm (Stoodley and Warwood, 2003). The use of coverslips with a precise thickness must be considered when developing a flow chamber. Here, microfluidic systems are advantageous because there are no other components between the coverslip and the objective. Components of other flow chambers, like the casing, may obstruct the movement of the objective.

2.5 Physics of Fluids in a Flow Chamber
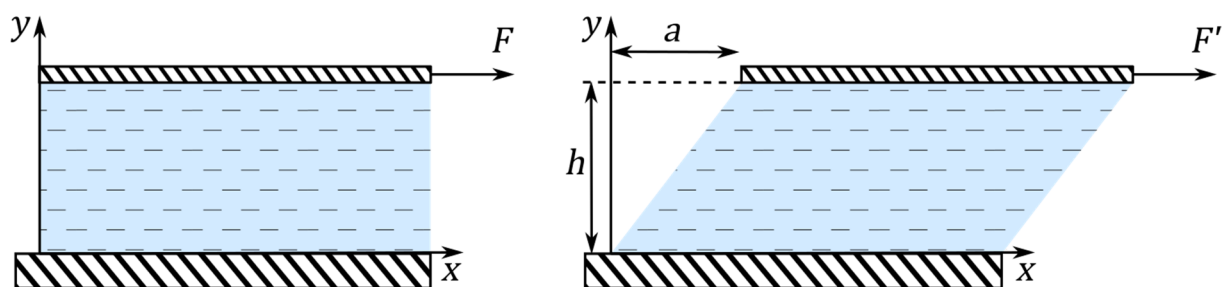
Figure 2-2: Shearing between two parallel plates, according to Aksel and Spurk (2019). The shearing is plotted in a coordinate system. y can be exchanged with the plate distance h. x is the length of the liquid column between the lower and upper plate. The deformation is expressed by a.

Fluids in a flow chamber can be described with the Couette flow model (Aksel and Spurk, 2019). A viscous fluid is located between two parallel plates as shown in Figure 2-2. If one plate is displaced tangentially with force F, shear stress τ acts on the fluid. The force is proportional to the rate of change

of the displacement, which is the velocity of deformation $u = \mathrm{d}a/\mathrm{d}t$, with $\mathrm{d}t$ being the timestep difference. The quotient of the velocity of deformation and plate distance h is the shear rate:

$$\dot{\gamma} = \frac{u}{h} = \frac{\mathrm{d}u}{\mathrm{d}y}. \tag{3}$$

The shear stress is then defined as:

$$\tau(y) = \eta \cdot \dot{\gamma} = \eta \cdot \frac{\mathrm{d}u}{\mathrm{d}y}. \tag{4}$$

The proportionality factor η is the dynamic viscosity which is further defined as:

$$\eta = \frac{F}{A} \cdot \frac{y}{u}, \tag{5}$$

with F being the force created tangentially on a plane of area A. For Newtonian fluids, the dynamic viscosity is constant, while for non-Newtonian fluids, it depends on the shear rate. Equations (3) to (5) show that the shear stress on the wall increases proportionally with higher flow velocities. Thus, bacteria that attach to the wall experience a higher displacement force with increasing flow velocities.

In the flow chamber, the static plate is the wall of the channel where bacteria might settle. When a liquid flow replaces the other plate Poiseuille flow occurs (Mory, 2013). Poiseuille's law applies if a pressure difference between the inlet and outlet generates a motion of the fluid. This pressure difference can result from pumping the liquid through the channel. For Newtonian incompressible fluids, the laminar flow profile is shown in Figure 2-3. Such a flow profile should occur in a flow chamber. With the width of the flow chamber much longer than the height, the flow profile will form between the top and bottom walls.
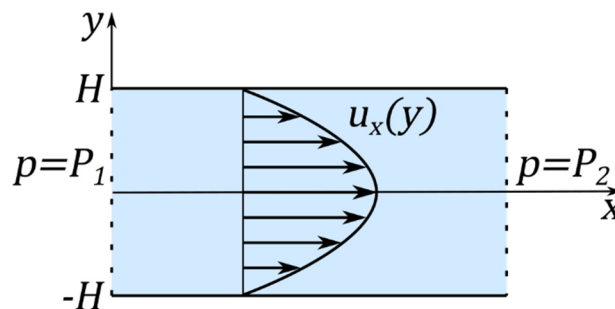
Figure 2-3: Plane Poiseuille laminar flow between parallel plates, according to (Mory, 2013). The top and bottom walls are positioned at *H* and *-H* in a flow chamber. The abscissa indicates the center of the bulk stream with the highest flow velocity. A parabolic velocity profile forms between the plates, where the velocity u_x depends on the distance to the center y. For a flow to establish between the plates, a pressure difference between the pressure P_1 at the beginning of the channel and P_2 at the end of the channel is necessary. To ensure that the current flows in the direction of P_2: $P_2 < P_1$.

As the velocity of a bacteria suspension changes from the central part to the walls of the flow chamber, so does the number of cells passing a position per time (Busscher, Bos and van der Mei, 1995). At the walls, the number is much lower than in the center. This transport of bacteria by flow is termed convection. If bacteria settle on the walls, depletion can occur within a zone in the vicinity of the surface. This zone is called the diffusion boundary layer. The attached bacteria must be replaced by bacteria originating from more central fluid layers. That is possible due to microbial diffusion. Therefore, a combination of diffusion and convection always occurs in a flow chamber. Additionally to microbial diffusion, bacteria are often capable of locomotion, which means an advantage as they can actively move within the flow and can reach the surface (Krsmanovic et al., 2021).

The two models presented above apply to laminar flows, in which fluid particles move in smooth layers. Interaction between adjacent layers occurs only by diffusion for fluid particles (Fang, 2019). To characterize the flow, the Reynolds number can be considered:

$$R_e = \frac{\rho u D_H}{\eta},$$ (6)

where ρ is the density of the fluid and D_H is defined as the hydraulic diameter. The hydraulic radius $R_H = D_H/4$ is the quotient of the channel cross section area and the wetted perimeter. The Reynolds number provides information on whether the flow is turbulent or laminar. For values $R_e < 2000$ a smooth laminar behavior is valid.

Velocity vectors and streamlines can be used to visualize the flow behavior in a flow channel. A velocity vector is part of an overall velocity field in the channel: at each position in the channel, there is a velocity vector at each point in time (Aksel and Spurk, 2019). Each velocity vectors points in the direction, where an infinitesimal fluid particle will move. Streamlines are curves whose tangent direction is the same as the direction of the velocity vectors at a given time. In the case of static flow, when the vector field no longer changes, the streamlines indicate which path a massless fluid particle takes (Landau and Lifshitz, 1987). Streamlines thus allow a visual description of the flow.

A flow chamber should be designed to have homogeneous flow characteristics in the region of interest (Busscher and van der Mei, 2006). Thereby the probability of a bacterium attaching is the same at each location for homogeneous substrate characteristics. As soon as bacteria have attached themselves, they change the flow behavior in their environment and thus the probability of new bacteria attaching. Now, a force acts on the attached bacteria parallel to the flow direction. The shear stress can cause attached bacteria to be pushed or to roll over the surface (Busscher and van der Mei, 2006).

From the described correlations follow that the parameters determining the flow characteristics of a flow chamber are fixed by its design, except for the flow rate. Variation in the pumping speed changes the flow rate, which causes a change in velocities and shear stresses in the channel. Thus, the flow rate

can be used to expose the microorganisms to various defined forces during an experiment. If, after a period of bacterial attachment, a higher flow rate increases the wall shear stress, bacterial retention can be determined (Bos, van der Mei and Busscher, 1999).

2.6 Multiphoton Lithography for 3D Printed Microstructures in Bacterial Attachment Studies

Multiphoton lithography or multiphoton polymerization is a 3D fabrication technique, which is especially suitable for creating high-resolution structures in the nano- and micrometer range (Huang et al., 2020). This is achieved by initiating local polymerization in a monomer resin using a femtosecond pulsed laser (Selimis, Mironov and Farsari, 2015). The laser is focused on a volume spot in the material via a lens system. There, consecutively arriving photons lift an electron of a molecule from the ground state to an excited state. The energy difference between the states is equal to the sum of the photon energies. After one photon has transferred its energy to the electron, the electron is elevated to a virtual energy level. Only a fast second arriving photon is able to lift the electron to the excitation band before it jumps back to the ground state. If the molecule is a photoinitiator, it forms radicals. These lead to confined radical polymerization. By shifting the focus spot, polymers can be generated in a controlled manner and three-dimensional structures can be formed. The non-crosslinked monomer is subsequently removed with a solvent, leaving only the 3D scaffold (Selimis, Mironov and Farsari, 2015).

The volume spot (voxel) in which the photo initiation happens is oval: along the beam axis (vertical), it is larger than perpendicular (lateral) to the beam (Malinauskas et al., 2016). A theoretical vertical resolution of 1/50th of the wavelength is possible. Wavelengths of lasers are typically in the near-infrared range at 780—800 nm. However, the vertical resolution is technically limited to 100—200 nm (Sugioka and Cheng, 2014). Due to the small voxel size and the high resolution, only small structures are practical to manufacture. Typical applications are Lab-on-a-chip devices and have a dimension of 1x1 cm^2.

Beyond that, the use of MPL printed structures in medical technology is promising. Focused research fields are cell and tissue engineering and medical microdevices (Huang et al., 2020). Conventional PDMS microfluidics devices, which are widely used as flow chamber systems for biofilm investigation, rely on soft lithographic methods and PDMS (Waheed et al., 2016). Here, with MPL, a new method has the potential to revolutionize the manufacturing of microfluidic devices and introduce new materials as substrates. Especially the fabrication of small structural elements like micro-sieves, micro-mixers, and micro-over-passes is interesting for microfluidic systems. Moreover, combining conventional PDMS devices with MPL techniques also opens up new (Bakhchova et al., 2020; Gonzalez et al., 2022).

Studies with microorganisms or cells using microfluidic flow devices in combination with MPL printed structures are scarcely described in the literature, although MPL has been used for microevolution (Harper et al., 2012), microbiorobotics (Hasselmann and Horn, 2018), or to study the fluid flow by flagella motion (Gao et al., 2015). Such experiments, however, were performed with single cells under static conditions and aspects of biofilm development have not yet been targeted. Nevertheless, they prove that MPL is a tool that can be used in flow systems studying bacteria. Naderi, Bhattacharjee and Folch (2019) pointed out that MPL is advantageous compared to surface structuring with PDMS. The benefits of MPL are the variability of printable materials, which offers a faster and more straightforward translation of research results and devices into commercial products. Among the few examples of MPL application in bacteria research to date is the work of Kaehr and Shear (2009). They used photomasks in concert with direct laser-write MPL to produce densely crosslinked protein matrices of different 3D geometries. Constructed as microenvironments for bacteria, exposed to a flow, the special design of the structures provided complex fluid manipulations and thus specific patterns of movement of the *E. coli* used. Lin et al. (2014) used MPL to create a bioprobe of the crosslinked proteins GFP-AcmA' and Eosin-Y. The green fluorescence protein (GFP) acted as an indicator to trace the AcmA' binding activity on peptidoglycan and allowed screening of the bacteria in flowing liquids. Barata et al. (2017) used microfluidics to investigate the influence of pyramidal structures on the spread of MG63 osteosarcoma cells. The structures were of cast polylactic acid. The required mold was made by combining MPL and soft lithography.

In summary, MPL is an innovative tool that has rarely been used in the study of microorganisms until now. Its application in bacterial attachment experiments has been completely lacking. However, results from medical field indicate that its use in bacterial attachment studies is promising. MPL opens new perspectives for the structuring of surfaces in the nano- and micrometer range and is therefore used in this study in addition to the deposition of ZnO nanorods.

2.7 Zinc Oxide: Properties and Nanostructures

ZnO nanorods have been investigated as a possible material to control the attachment of bacteria and cells (Makarona et al., 2016; Lin et al., 2022). The nanostructures are promising since tunable surface roughness can be achieved (Djurišić et al., 2012). Surfaces with ZnO nanostructures can be coated on a large scale with high homogeneity. Additionally, the cost-efficient processing makes the nanomaterial a potential bacteria repelling coating applicable on an industrial level (Aurang et al., 2013). However, some aspects have to be considered for using ZnO nanorods to study bacterial attachment. Therefore, in the following, the material properties of ZnO in general and the specific ZnO nanorod appearance, synthesis, photoluminescence, biocompatibility, and dissolution behavior will be discussed.

The world's main consumer of ZnO is rubber production (Mostoni et al., 2019). A large part of this accounts for the manufacture of tires in the automotive industry. ZnO is used in rubber production as an accelerator of sulfur vulcanization, thus reducing the processing time. Apart from that, it is used on a large scale in the ceramics, cement, and cosmetics industries and has many other applications (Moezzi, McDonagh and Cortie, 2012). For two decades, the range of applications of ZnO has continuously expanded (Wang, 2008). A contributing factor has been the fact that the material is subject to intensive research. Among other reasons, this is due to the properties of ZnO as a semiconductor. It has a broad energy band gap and is thermally and mechanically highly stable at room temperature. It has piezoelectric and pyroelectric properties, which makes it a potential material for sensors, energy generators, and photocatalysts for hydrogen production (Wang, 2008).

At the atomic level, ZnO has the lattice structure of wurtzite (Vayssieres et al., 2001). It is ionic and polar, and the atoms are arranged in a close hexagonal packing. Four oxygen ions tetrahedrally coordinate the zinc ions, and the oxygen ions are coordinated similarly by four zinc ions. This situation leads to a non-central geometrical structure which is the reason for the piezoelectric properties (Wang, 2004). In addition, polar surfaces are formed at the lattice boundaries since either exclusively zinc atoms or oxygen atoms are exposed. These are positively charged Zn-(0001) and negatively charged O-(000$\bar{1}$) facets.

ZnO offers many possibilities to create nanostructures. ZnO nanoparticles are among the three most produced metal-containing nanoparticles in the world, along with TiO_2 and SiO_2 (Bondarenko et al., 2013). ZnO one-dimensional nanostructures include belts, which were the first nanostructures created in 2001 (Pan, Dai and Wang, 2001), needles (Wahab et al., 2007), and rods (Greene et al., 2003). Examples of two-dimensional structures are nanoflakes (Wang et al., 2017) and nanowalls (Yu et al., 2016). Three-dimensional structures include ZnO nanoflowers (Liu et al., 2006) or nano snowflakes, as

shown in Figure 2-4. ZnO nanoparticles can be synthesized by various physical, chemical, and biological methods (Gharpure and Ankamwar, 2020). The reaction parameter greatly influences the shape and properties of the ZnO nanoparticles. Hence a knowledge and strict control over the reaction conditions is mandatory. For ZnO nanorods by a hydrothermal synthesis, a certain growth rates of the facets is favored (Wang, 2004). Since the growth rate is highest along the [0001] direction, the typical hexagonal nanorods are formed.
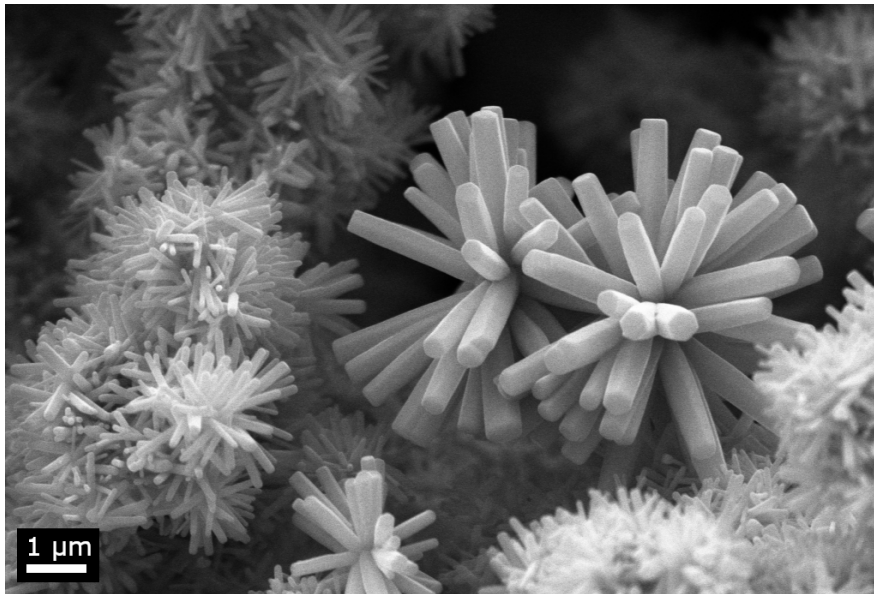
Figure 2-4: ZnO snowflakes, synthesized on glassy carbon foam with subsequent combustion. The synthesis was done similarly to the route described in chapter 3.2.7.

The first synthesis of ZnO rodlike nanocrystals in solution was done by Vergés, Mifsud and Serna (1990). However, it took more than ten years when Vayssieres et al. (2001) produced ZnO nanorods on silicon wafers using a hydrothermal method. At the same time, Huang et al. (2001) created nanowires with controlled diameters on Au-coated silicon substrate by vapor liquid solid growth, a typical vapor phase synthesis. Another vapor phase synthesis commonly used for ZnO nanorods is physical vapor phase deposition (Zhang et al., 2012). Both techniques require high temperatures around 400-650 °C or more and a vacuum. Thus, high-purity, well-aligned ZnO nanocrystals can be produced. On the other hand, the processes require technically sophisticated equipment. In contrast, solution phase syntheses require lower temperatures, are inexpensive, and easier to handle. Hydrothermal growth is the most frequently used liquid synthesis. Besides, the sol-gel method using concentrated zinc acetate suspension was established (Zhu et al., 2005).

The hydrothermal method for the growth of ZnO nanorods on various substrates is generally carried out in an aqueous solution at temperatures <100 °C (Baruah et al., 2010). The nanostructures have a high crystal defect density in the form of crystal structure defects and oxygen vacancies. The defects

can be healed by subsequent annealing. It increases the quality of the crystal lattice (Gao et al., 2010) and reduces the oxygen vacancies if sufficient oxygen is present from an O_2-containing atmosphere (Li et al., 2008). ZnO nanorods are usually produced on substrates in the following order (Zhang et al., 2012):

1) A thin layer of ZnO nanoparticles is deposited on the substrate. It serves as a nucleating agent and is termed the seed layer. It enables the growth of nanostructures by lowering the thermodynamic barrier.

2) Highly soluble Zn^{2+} salts, such as $Zn(NO_3)_2$ or $ZnCl_2$, are mixed with an alkaline reagent, such as NaOH or hexamethylenetetramine, in an aqueous solution. This mixture is termed the precursor or growth solution.

3) The substrate is kept in the growth solution for a certain period at a specific temperature.

4) The coated substrate is sufficiently washed and dried.

The seed layer can be created in many ways, such as by radio frequency sputtering (Song and Lim, 2007) or electroplating (Liu et al., 2009). Another possibility is the application of pre-synthesized ZnO nanoparticles or the coating with zinc acetate (Baruah and Dutta, 2009). Both the annealing temperature as well as the size, structure, and distribution of the seedlings influence the final appearance of the ZnO nanorods. That is, in particular, the orientation, the packing density, and the diameter of the nanostructures.

ZnO nanostructures have photoluminescence properties (Galdamez-Martinez et al., 2020). These properties strongly depend on the shape of the nanostructures, which in turn are influenced by the type of synthesis. A variety of optical properties is the consequence. The photoluminescence of ZnO nanostructures can be analyzed by photoluminescence spectroscopy. For this, the sample is excited with a UV laser or UV lamp. A suitable wavelength is 325 nm. Typically, two regions are observed where ZnO emits electromagnetic waves upon high-energy irradiation: the near-band edge excitonic emission (NBE) in the near UV range and the deep-level emission (DLE) in the visible light spectrum (Galdamez-Martinez et al., 2020).

The NBE is a direct consequence of the band gap in ZnO (Pearton et al., 2003). Excitation with electromagnetic radiation creates bound excitons in the material. These excitons can resolve by band-band recombination, emitting electromagnetic radiation approximately equal to the band gap. For ZnO, the band gap is 3.2 eV, which corresponds to a wavelength of 388 nm. A pronounced occurrence of NBE in ZnO nanorods is associated with high crystal quality (Bekeny et al., 2006). Moreover, enhanced vertical alignment of ZnO nanorods is considered an additional possibility for a prominent NBE. Furthermore the NBE can be used to characterize the size distribution of the nanorods (Ng et al.,

2003). A small width at half maximum is considered typical for a narrow size distribution of the nanorods.

The emission band between 3.1 eV and 1.65 eV is attributed to DLE (Djurišić et al., 2006). Its origin is associated with exciton transitions and defects in the crystal structure. The cause for these effects lies in the type of synthesis. Generally, different colored emissions of the DLE are distinguished. For a green emission, oxygen vacancies are considered responsible. As another possible source, impurities, for example copper, are considered. Yellow-orange emissions are associated with an excess of oxygen. The oxygen can be incorporated as interstitials resulting from a hydrothermal synthesis, for example. In addition, red-orange emission was reported. Often these three types of emission occur together (Djurišić et al., 2006).
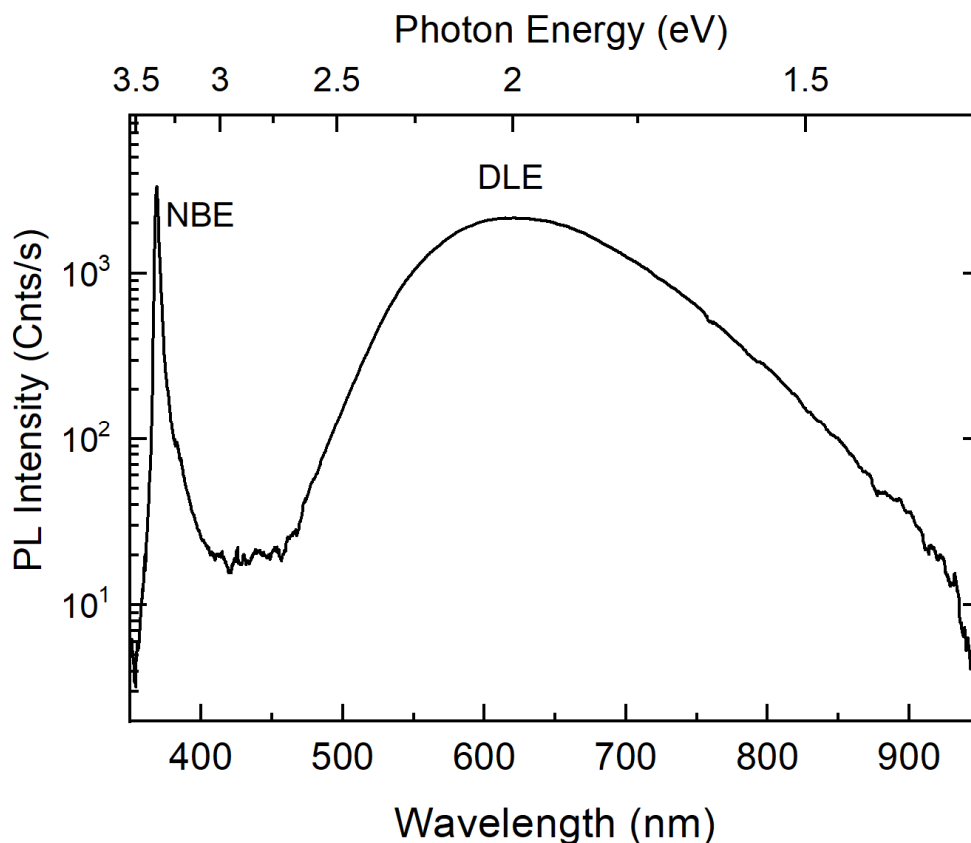
Figure 2-5: Photoluminescence spectrum of ZnO nanorods synthesized according to the procedure in chapter 3.2.7. The spectrum was recorded at a temperature of 10 K. Data was provided and published in Macková et al. (2022).

NBE and DLE for the ZnO nanorods used in the present project are shown in Figure 2-5 for a temperature of 10 K (Macková et al., 2022). The photoluminescence peaks of NBE and DLE are temperature dependent (Ahn et al., 2009). As the temperature increases, the intensities decrease, the peaks broaden, and a slight peak shift of a few 100ths of eV can occur. The extent of the NBE and DLE

peaks' change with rising temperature depends on the synthesis conditions of the nanorods. Wang and Gao (2003) reported a pronounced NBE and a very weak DLE photoluminescence at room temperature for ZnO nanorods prepared by hydrothermal synthesis.

The toxicity and biocompatibility of ZnO nanoparticles must be considered if they are applied in bacterial studies. Generally, the chemical compound ZnO has been attributed to low toxicity and biocompatibility (Kolodziejczak-Radzimska and Jesionowski, 2014). However, such statements must be considered critically for ZnO nanoparticles whose use has increased in recent years (Czyzowska and Barbasz, 2020). While human exposure to sunscreens on the skin is unlikely to be problematic, the situation is different for inhalation and ingestion of ZnO nanoparticles. In animal studies, changes in organs such as the lungs, liver, and kidneys have been observed when ZnO nanoparticles regularly enter the body. Toxicity possibly occurs in the form of oxidative stress, genotoxicity, inflammatory responses, and apoptosis. Cytotoxicity has been confirmed by experiments with cultured human cells. They trigger oxidative stress, which can lead to DNA damage (Czyzowska and Barbasz, 2020).

ZnO nanoparticles can have a damaging effect on microorganisms (Gharpure and Ankamwar, 2020). Three possible mechanisms are described. Reactive oxygen species are thought to be electrochemically generated by light, with ZnO acting as a photocatalyst. In addition to oxygen radicals, H_2O_2 can form, which enters the cells and has a variety of damaging effects there, leading to cell death. Another possibility is the adhesion and uptake of ZnO nanoparticles to the microorganism cell. Attachment results in strong interactions with the membrane, as the ZnO nanoparticles are positively and the cell membranes are negatively charged. Thus, defects are formed on the surface of the cell membrane, and nutrient exchange with the cytoplasm is blocked. Finally, possibly released zinc ions by dissociation of ZnO has an antimicrobial effect. As a matter of fact, Zn^{2+} ions disturb the activity of enzymes by blocking them. However, the impact on cell metabolism depends on the concentration of Zn^{2+} ions. The actual Zn^{2+} ion generation from ZnO nanoparticles depends on many factors, whose transferability to a natural environment is questioned (Jiang, Mashayekhi and Xing, 2009). Thus, the antimicrobial effect of Zn^{2+} ions released from ZnO nanoparticles is still under debate (Gharpure and Ankamwar, 2020).

ZnO is a salt that is very difficult to dissolve. In water, it dissolves to 0.0004% at room temperature (National Institute for Occupational Safety and Health, 2021). The solubility in acids and bases increases strongly (Richardson and Lange, 2009). The dissolution behavior of ZnO in aqueous solutions is very complex since various zinc hydroxides occur in addition to dissociated Zn^{2+} and O^{2-} ions (Richardson and Lange, 2009). In contrast to bulk ZnO, the solution behavior of ZnO nanoparticles may differ (David et al., 2012). The solubility increases exponentially with an increasing surface/diameter ratio. That is noticeable for nanoparticles of a few nm diameters. Reed et al. (2012) stated that the

solubility of ZnO bulk and nanoparticles depends on other components in an aqueous solutions . They observed increasing solubility for moderately hard water, nanopure water, and cell culture media. The reaction kinetics range from a few hours to days. Responsible for this are certain solution equilibria with participating anions. For example, zinc precipitates with carbonates in moderately hard water at lower concentrations. A similar reaction is described for phosphate ions (Herrmann, Garcia-Garcia and Reller, 2014). These attack ZnO independent of the pH value and form precipitates of zinc phosphates. For this reason, it is important to analyze and evaluate the dissolution behavior of ZnO in the experiment where the material is involved.

2.8 The Model Organism *Pseudomonas fluorescens*

Pseudomonas fluorescens is a gram-negative rod-shaped bacterium with a width of 0.5–0,7 µm and a length of 1.5–2 µm (Rhodes, 1959). It is anaerobic and chemoorganotrophic. The species' name is derived from a yellow-green, fluorescent, water-soluble pigment (Meyer and Abdallah, 1978). It is a so-called siderophore, which *P. fluorescens* biosynthesizes and releases into the medium to scavenge iron ions. The corresponding coloration is therefore pronounced under iron deficiency. *P. fluorescens* is motile by one or more single or double flagella (Blazevic, Koepcke and Matsen, 1973), which are polar arranged (Redondo-Nieto et al., 2013). It develops many pili (Vesper, 1987) as well as EPS (Kives, Orgaz and Sanjose, 2006), which contributes to the ability of *P. fluorescens* to form a biofilm under almost any condition (O'Toole, Kaplan and Kolter, 2000). The bacterium is ubiquitously distributed, especially abundant in water and soils, and commonly associated with plants (Bossis et al., 2000). It occurs in the rhizosphere and is part of the epiphyllous community of many plant species. *P. fluorescens* can promote plant growth and plant health. In the soil, it is part of the natural suppressiveness of various soilborne diseases. However, *P. fluorescens* is also an opportunistic plant pathogen (Bossis et al., 2000).

P. fluorescens was chosen as the model organism for the study because it is acknowledged to be a pioneer colonizer in the process of biofilm formation and is often found in the primary stage of biofilm formation in aquatic environments (Dogruoz et al., 2009). The bacterium is an great economic impact as it is involved in food spoilage, especially of dairy, poultry, and fresh products (Wang et al., 2018). It is widely non-pathogenic to humans (Scales et al., 2014). Reported infection cases were either due to transfusion of blood or contaminated blood products. *P. fluorescens* is classified in risk group 1 for biological agents (Ausschuss für Biologische Arbeitsstoffe, 2015). These reasons have led to the bacterium already being investigated in many bacterial attachment studies, besides *E. coli*, *P. aeruginosa* and *S. aureus* (Korber, Lawrence and Caldwell, 1994; Díaz et al., 2007; Valiei et al., 2012; Hsu et al., 2013; Spark et al., 2017).

The strain *P. fluorescens* SBW25 was isolated by Thompson et al. (1995) from sugar beet leaves. It has been genetically modified and used in field trials to study the spread of genetic material in the ecosystem. Its chromosome was sequenced entirely (Rainey and Bailey, 1996). *P. fluorescens* SBW25 was used as a model organism in evolution experiments (Pentz and Lind, 2021) as well as a model organism for the colonization of plant parts (Carroll et al., 2020). Noteworthy is its ability to fast and uniquely complex movements, which is enabled by a single flagellum on one of the cell poles (Ping, Birkenbeil and Monajembashi, 2013).

2.9 Lipopolysaccharides

Lipopolysaccharides are essential envelope components of the outer membrane of many Gram-negative bacteria (Whitfield and Trent, 2014). The outer membrane of these bacteria is a bilayer, with the inner leaflet consisting of phospholipids and the outer leaflet consisting of LPS as the main components (Gnauck, Lentle and Kruger, 2016). Three-quarter of the bacterial cell surface comprises LPS.

The single LPS molecule is built up of three components: the lipid A, the core oligosaccharide, and the O-antigen (Saier, 2019). A schematic illustration is presented in Figure 2-6. The hydrophobic lipid A serves as an anchor within the membrane. It consists of a glucosaminyl-b-(1→6)-glucosamine backbone, which is substituted with six or seven saturated fatty acyl residues. The lipid A component is linked to the core saccharide, which resides over the membrane and is connected to the O-antigen. The O-antigen protrudes into the environment around the cell. The LPS of a bacteria species is unique, which is why they serve as fingerprints (Sperandeo, Martorana and Polissi, 2019). The variability among the species rises from the components Lipid A to O-antigen. Hence, the O-antigen has been used for serological classification in immune response or antibody diagnostic (Fomsgaard, 1990). The O-antigen component comprises oligosaccharides which are made of 1–8 sugar species (Caroff and Novikov, 2020). The oligosaccharide units are linear or branched and often contain substituents like glycerol, phosphate groups, and acetyl groups. For example, the *P. aeruginosa* serotype 10 has O-antigens with repeating units of rhamnose, N-acetylgalactosaminuronic acid, and N-Acetyl-D-Quinovosamine (Knirel et al., 2006).

Lipopolysaccharides have a special significance in medicine. On the one hand, they take part in the defense mechanism of bacteria against antibiotics. On the other hand, free LPS from dead and lysed cells provides complex physiological effects in mammalians (Rietschel et al., 1994). Especially noteworthy are the immune responses as soon as free LPS is present, which is why they are also designated as endotoxin (Brandenburg, Schromm and Gutsmann, 2010). The LPS is recognized by

immune cells, which then initiate inflammatory processes (Heumann and Roger, 2002). As the structure of lipid A is essential for the LPS recognition of the cells, similar molecules have been developed which have inflammatory properties without the severe accompanying symptoms (Casella and Mitchell, 2008). They are used as a vaccine adjuvant, for instance.
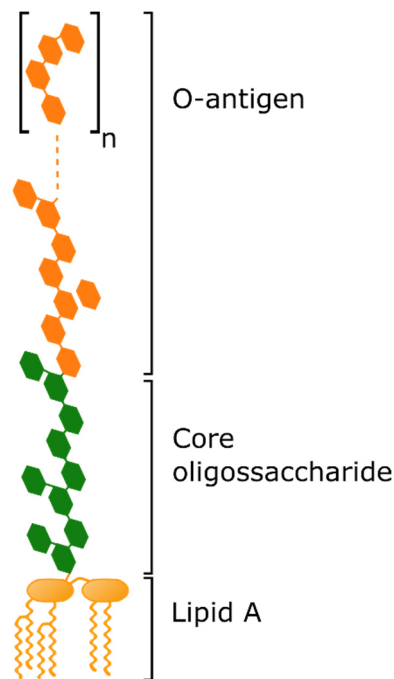
Figure 2-6: Schematic representation of a single LPS molecule according to Whitfield and Trent (2014).

2.10 Treatment of Particles with Lipopolysaccharides

Various strategies have been explored for the incorporation of LPS (lipopolysaccharides) into nano- and microparticles, as well as their encapsulation within these particles. For instance, the LPS derivative monophosphoryl lipid A was integrated into poly(lactide-co-glycolide) microparticles alongside HIV-1 protein and *Neisseria meningitidis* antigen (Kazzaz et al., 2006). This composite was then assessed for its potential as an immune enhancer. In a similar vein, LPS-covered nano- and microparticles composed of poly(lactic-co-glycolic acid) were devised to stimulate immune cells (Demento, Steenblock and Fahmy, 2009). LPS-treated latex (polystyrene) microparticles are important for the serological latex agglutination test (Hechemy, Stevens and Gaafar, 1976), exemplified by their application in the serodiagnosis of human brucellosis (Abdoel and Smits, 2007).

All of these presented studies have in common that they achieve one adsorption of LPS to the polymer microparticles. For example, LPS adsorption is favored due to hydrophobic interactions of lipid A to

the PS surface, which is associated with an entropic increase by dehydration of the PS' and LPS' hydrophobic zones (Peula-Garcia et al., 2002).

LPS has been shown to adsorb at long acyl chains with the lipid A domain. Taking advantage of this fact, Prasad et al. (2018) harnessed this feature to engineer a magnetic nanoparticle system capable of capturing free LPS from solutions. In the next step, the nanoparticles could be regenerated by desorption.

To control the orientation of LPS, Piazza et al. (2011) used hydrophobic brush nanoparticles coated with oleylamine. In that way, the nanoparticles mimic natural micelles or membranes with included LPS. They pursued this approach because they claim the physical adsorption of LPS on surfaces to be a highly unstable system with an arbitrary arrangement. By using a hydrophobic brush, lipid A was bond inwards and the O-antigen oriented outside.

Advancing the fixation of LPS to nanoparticles, Jang et al. (2017) achieved a strong interaction between LPS and poly(allylamine hydrochloride). Responsible for an electrostatic interaction were the phosphate groups of the LPS and the amine groups of the substrate. Likewise, the LPS were aligned as in bacteria.

In this study, a new approach was pursued to bind LPS tightly to microparticles adapted from a method which was developed by Behnke et al. (2010) and Behnke et al. (2012). PS particles in an aqueous solution swell by adding certain organic solvents. If the hydrophobic microparticle surface is penetrable, Lipid A might accumulate at the PS polymer chains. In the next step, the organic solvent is removed, causing the microparticles to shrink. The LPS is now anchored with lipid A within the PS microparticles and the rest of the core oligosaccharide is exposed to the environment.

3 Materials and Methods

3.1 Materials

DIN A4 sheets of Elastosil foil of 100 µm thickness on polyethylene terephthalate (PET) film as support were purchased from Wacker (Germany). Silgard 184 Silicone was ordered from Dowsil (Dow, U.S.), and the Monarch® Plasmid Miniprep Kit from New England Biolabs (U.S.). Plate count agar, Lysogene Broth, succinic acid ≥99%, K_2HPO_4 ≥99%, $(NH_4)_2SO_4$ ≥99%, $MgSO_4·7H_2O$ ≥99.5%, NaOH as pellets ≥98%, NH_3 (30 %), H_2O_2 (25 %) 2-Propanol ≥99.8%, phosphate-buffered saline (PBS, pH 7.4), borate buffer (pH 10.00), and tetrahydrofuran (THF) were purchased from Chemsolute (Th. Geyer, Berlin, Germany). KH_2PO_4 ≥99% and zinc nitrate hexahydrate ≥99.998% were ordered from Thermo Fisher Scientific (U.S). Gentamycin solution, kanamycin solution, hexamethylenetetramine ≥99.5%, methyl isobutyl ketone ≥99%, phenol extracted lipopolysaccharides from *P. aeruginosa* (strain ATCC 27316 serotype 10.22) and fluorescein-5(6)-isothiocyanate were purchased from Sigma-Aldrich (Merck, Germany). The Helper Plasmid pTNS2 was a gift from Herbert Schweizer (Addgene plasmid # 64968)(Choi et al., 2005). SZ2080 negative photoresist containing 1 wt% of Michler's ketone photoinitiator (IESL-FORTH, Heraklion, Greece) was used for MPL fabrication of 3D block patterns. Plain 1 µm diameter PS microparticles (2.5 %) were purchased from Kisker Biotech (Steinfurt, Germany). Mica sheets (V1 quality, 0.16 mm thickness) were procured from Plano GmbH (Wetzlar, Germany). Epoxy adhesive epo-tek 377 was purchased from Epoxy Technology Inc. (Billerica, Massachusetts, U.S).

3.2 Part I: Bacterial Attachment and Retention on Nano- and Microstructured Surfaces

This section starts with the general methods for studying the attachment and retention of bacteria in this project. From section 3.2.6 the methods address specifically the experiments with ZnO nano- and microstructured surfaces.

3.2.1 Development of a Microfluidic Flow Chamber

Already existing flow chambers could not meet the requirements for an in-situ flow system in the present project. Therefore, an appropriate custom-built flow chamber was developed, which was based on existing designs. Figure 8-1 in the Appendix depicts the technical drawing of the main

component of the flow chamber. The final setup of the microfluidic flow chamber is presented in Figure 3-1.
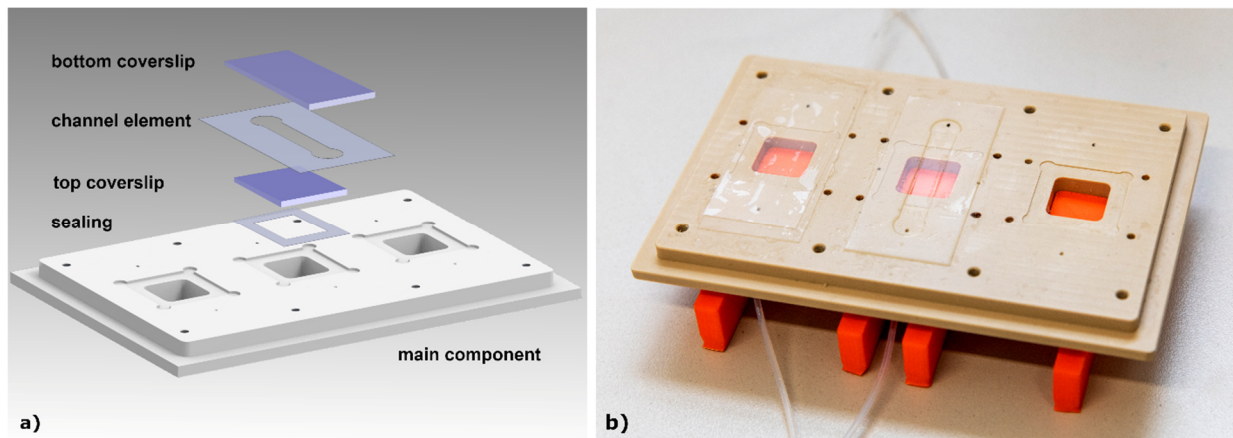
Figure 3-1: Schematic setup of the microfluidic flow chamber (a) and a photographic image of the flow chamber with partially assembled channels (b). The orange component is a 3D printed mounting device to simplify the assembly.

The exterior dimensions of the main component were given by the well plate holder, which was mounted in the Z-Galvo stage of the microscope (Leica SP8, Germany). This enabled a maximum of three separate channels to be installed. The bright-field was coupled in via the head of the microscope. Since it was an inverted microscope, the sample was illuminated in transmission mode. To allow light to pass the samples, illumination windows had to be included in the main component, and transparent materials had to be used. The transparent material glass was used in form of coverslips as it simultaneously served as the top and bottom confinement of the flow channels. With such a setup, viewing attached bacteria with and without the influence of gravity was possible. The flow chamber main component, which satisfied all requirements, was milled out of polyether ether ketone. This material withstands high temperatures and pressure and can thus be sterilized by autoclavation.

A Leica HC PL APO 63x/1.20 W CORR CS2 was chosen as the objective. With its 63x magnification and large numerical apparatus, individual bacteria could be clearly identified. However, the high resolution came at the expense of the maximum working distance, which amounted to 300 µm. Furthermore, only high-precision coverslips with a thickness of 170 µm could be used in combination with the objective. Theoretically, it was possible to focus to a maximum of 300 µm in the z-direction within the top and bottom confinement of the channel. However, this turned out to be not possible in the praxis, and a channel height (z-range) of 100 µm was chosen. The reason for this was that it was almost impossible to avoid a slight tilt of the coverslip, causing the top of the objective to collide with the coverslip, thus reducing the working distance. Furthermore, water was used as an immersion medium between the coverslip and the objective. Both restrictions implied that there had to be no elements

with >1 mm thickness below the bottom coverslip. Otherwise, the flow chamber would have interfered with the objective. These restrictions limited the use of a frame as a component for the flow chamber, as often implemented (Owens, Gingell and Rutter, 1987; Rath, Stumpp and Stiesch, 2017; Shurbaji et al., 2020). Such a frame is commonly used to press the coverslip against an elastic material, thereby sealing the flow channel. The first setup in the present project contained a frame that was used to press and seal the flow channels. The frame is depicted in Figure 8-2 in the Appendix. However, this setup was rejected as the thin frame did not seal the flow channels. Therefore, the channels were prepared with the bottom coverslips directly fixated on channel elements of 100 µm thickness using the plasma bonding method. The channel element served as vertical confinement of the flow channel and was made of PDMS.

Inlet and outlet holes were drilled at a 45° angle in the flow chamber's main component. The holes had a diameter of 0.9 mm where the inlet and outlet joined the flow channel. By means of the 45° fluid inlet and outlet, a quick adjustment of the laminar flow profile was achieved. The opposite sides of the inlet and outlet holes were threaded. MINSTAC® end connectors (The Lee Company, U.S.) were screwed in the thread. At the other side of the connectors, Teflon tubings of 0.8 mm joined, which enabled a fluid connection to appended fluid distribution system, pumps, and liquid waste collection.

3.2.2 Preparation of Flow Channels

A high-precision coverslip with dimensions 24 mm x 50 mm x 0.17 mm was treated with RCA cleaning for 10 min. For RCA cleaning, five volume parts of deionized water (diH$_2$O) were heated to 85 °C. Then one volume part of NH$_3$ and one volume part of H$_2$O$_2$ were added and tempered at 85 °C. A Teflon holder allowed the coverslip to be placed upright. After cleaning, the coverslip was rinsed with diH$_2$O, cleaned twice for 10 min in an ultrasonic bath in diH$_2$O, and dried under a stream of N$_2$. To increase the final bonding strength between PDMS and coverslip, hydrophilization was performed. For this purpose, 35 - 40 ml of an aqueous 10 mol/l NaOH solution was poured into a Petri dish with a diameter of 92.7 mm and heated to 45 °C. The coverslip could now be dipped vertically on all four sides for 10 s. Subsequently, it had to be rinsed vigorously with diH$_2$O and cleaned at least three times in an ultrasonic bath with diH$_2$O for 10 min. After drying under N$_2$, no crystalline NaOH should remain on the coverslip.

PDMS channel elements with 100 µm thickness were prepared by cutting an Elastosil foil according to a template with a Zing laser cutter (Epilog Laser, U.S.). A simple kitchen polyethylene (PE) foil shielded the unprotected side of the PDMS film from combustion products from the laser cutter. Settings for the laser cutter were: 20% power and 100% speed. The template was made up of a string of many individual channel elements, as shown in Figure 8-3 a) in the Appendix. The channel elements were

placed together with the prepared coverslips in the chamber of a Zepto plasma cleaner (Diener, Germany). Before, the PE film on the channel elements was peeled off to expose the PDMS on one side. Activation of surfaces was performed in the plasma cleaner under an air atmosphere of 1 mbar for 1 min. After removal from the chamber, a channel element was immediately placed centrally on a coverslip with the side of the activated PDMS facing the coverslip. Air was expelled between the PDMS and the glass by slightly smoothing. The coverslip was then placed on a hot plate at 100 °C for 1 min, followed by curing for 2 h at 80 °C in an oven.

The further assembly of the flow chamber can be seen in Figure 3-1. First, a sealing made of 100 μm Elastosil was inserted into the recess of the main component of the flow chamber, then a high-precision coverslip with the dimensions of 22 mm x 22 mm x 0.17 mm. The sealing was cut out like the channel element; the cutting design is shown in Figure 8-3 b) in the Appendix. The top coverslip was prepared in the same way as the bottom one. The top coverslip, sealing, and main component were bonded with Silgard 184. The application was carried out according to the manufacturer's instructions, but the ratio 8:2 elastomer base:curing agent was chosen. Silgard 184 was also applied as a thin film on the untreated side of the channel element to combine it with the main component. Prior to this, the PET film of the untreated side of the channel element was peeled off. Curing of the as-assembled flow chamber was carried out in the oven for 24 h at 80 °C, while a weight on the bottom coverslip applied pressure.

3.2.3 Culture Conditions of *Pseudomonas fluorescens* and its Genetical Transformation

Pseudomonas fluorescens SBW25 was a kind gift of the Microbial Population Biology group of Dr. F. Bertels (Max Planck Institute of Evolutionary Biology, Plön). Immediately after obtaining the culture, bacterial material was taken with an inoculating loop and struck out on plate count agar. The plates were incubated at 30 °C until colonies were visible. Bacteria were picked from one colony, and 40 ml of a liquid medium in an Erlenmeyer flask was inoculated. Incubation was done with a rotary shaker at 120 rpm and 30 °C. A minimum mineral medium (MMM) was used, according to Meyer and Abdallah (1978). In three separate bottles 6 g/l K_2HPO_4 with 3 g/l KH_2PO_4 and 1 g/l $(NH_4)_2SO_4$ with 0.2 g/l $MgSO_4 \cdot 7H_2O$ and 4 g/l succinic acid were dissolved in diH_2O and autoclaved. A pH of 6.9 was adjusted with NaOH before sterilization. The use of this MMM instead of a complex medium or bouillon had several advantages. Knowledge of potential cations is important in studying bacterial attachment and biofilm development. The cations adhere to the substrate in the conditioning layer and affect the cell substrate interaction. Even if the cations are largely removed by washing the bacterial suspension before the experiment, their existence cannot be excluded. Furthermore, the development of the

culture in the MMM, which is clear at the beginning, can be followed visually. The lack of nutrients that other organisms require was a natural protection against their contamination.

When the incubated liquid culture had an optical density at 600 nm (OD_{600}) of 0.2, 500 µl was added to a 500 µl mixture of 1:1 glycerol:diH₂0 in cryotubes. The cryotubes were stored at -80 °C. Random 10 µl of thawed frozen cultures were diluted, plated out, and incubated to determine the number of frozen bacteria that could be reawakened. After colonies became visible, the number of colony-forming units in the frozen culture could be estimated.

P. fluorescens SBW25 was transformed to *P. fluorescens* SBW25 attTn7::$P_{A1/04/03}$-*gfp2,* which expresses GFP and a gentamycin resistance. *P. fluorescens* SBW25 attTn7::$P_{A1/04/03}$-*gfp2* was used for the experiments with ZnO surfaces in part I of the present project. A liquid culture with 25 ml MMM was prepared from thawed *P. fluorescens* SBW25 and incubated at 120 rpm and 30 °C. When the culture had an OD_{600} of 2.0, it was washed five times with 10% glycerin in diH₂O. For this purpose, the culture was poured into a 50 ml centrifuge tube and centrifuged for 10 min at 7000 rcf and 4 °C. The supernatant was removed, the glycerin solution was replenished, and the pellet was resuspended. Simultaneously, a culture of *E. coli* XL1-Blue possessing the GFP donor plasmid pKB-mini-Tn7-gfp2 GmR 10 µg/ml, AmpR 100 µg/ml (Koch, Jensen and Nybroe, 2001) was grown from -80 °C stock in LB medium at 37 °C and 180 rpm overnight to an OD_{600} of 2.0. The plasmid extraction was done with the Monarch® Plasmid Miniprep Kit according to the manufacturer's protocol. After the last centrifugation cycle of *P. fluorescens* SBW25, the pellet was resuspended in 100 µl glycerin solution, and 70 ng of pKB-mini-Tn7-gfp2 and 90 ng of helper plasmid pTNS2 was added. All preparation steps had to be done with 4 °C cooled liquids and materials. The suspension was kept for a further 10 min in an ice bath. Penetration of the pKB-mini-Tn7-gfp2 plasmid into the recipient culture by the electroporation method was enabled by the aid of the Gene Pulser Xcell System (Bio Raid, California). The settings were 2500 V, 25 µF, and 200 Ω for 5 ms. Immediately after that, the suspension of electrocompetent cells was filled up to 1 ml with Super Optimal Broth and incubated for 1.5 h at 30 °C. The final step was the selection of the GFP-tagged bacteria by plating on selection plates. For this purpose, culture plates with plate count agar and 60 µg/µl gentamicin were prepared. Since the transferred donor plasmid also had a region of gentamycin resistance, only those bacteria that integrated the plasmid into their chromosomal DNA survived. After two days of incubation at 30 °C, a colony was picked and grown in MMM. The culture was used to make frozen cultures according to the procedure already described.

P. fluorescens SBW25 was transformed to *P. fluorescens* SBW25 pMRE-Tn7-155 to aid identification against the background of the 3D printed polymer SZ2080 by means of the protein mScarlet-I (Bindels et al., 2017). That was done as described for the treatment with pKB-mini-Tn7-gfp2 plasmid, without

the use of a helper plasmid. Thus, the genes were not integrated into chromosomal DNA but remained as plasmids in the receiving organisms. The donor organism was *E. coli* NEB5-alpha pMRE-Tn7-155. After the insertion of the plasmid by the electroporation method, the recovered culture was incubated on selection plates containing 50 µg/ml kanamycin since pMRE-Tn7-155 carried a kanamycin resistance. A colony was picked, grown in MMM, and used for making frozen cultures as described.

A liquid culture for the flow chamber experiment was prepared with MMM, as described above. For this purpose, either *P. fluorescens* SBW25 attTn7::P$_{A1/04/03}$-*gfp2* or *P. fluorescens* SBW25 pMRE-Tn7-155 was taken for the experiment with ZnO nano- and microtopographies or with 3D printed microstructures. A frozen stock was thawed, diluted to one cell, and the medium was inoculated. After about 2 days, the bacterial culture had an OD$_{600}$ between 0.15-0.2. Harvesting of the bacterial culture in this early to mid-exponential phase yielded single cells in the majority. At higher turbidities, more cells stick together, which complicates cell number evaluation with microscopy. Harvesting was done by washing the bacteria three times in PBS (7000 rcf, 30 °C, 10 min) and the bacterial suspension was adjusted to an OD$_{600}$ of 0.1 with PBS. This optical density corresponds to cell numbers of $\sim 1.3 \cdot 10^8$ cells/ml and $\sim 1.2 \cdot 10^8$ cells/ml for *P. fluorescens* SBW25 attTn7::P$_{A1/04/03}$-*gfp2* and *P. fluorescens* SBW25 pMRE-Tn7-155, respectively.

3.2.4 Characterization of the Samples with Imaging Techniques

Samples with ZnO nano and microtopography and MPL 3D printed microstructures were examined using a scanning electron microscope (SEM) and atomic force microscope (AFM). A simple light microscope with incident light was useful for a rough preliminary check to detect larger defects in the topography. SEM was used to evaluate the appearance, quality, and dimensions of the nano and microstructures. AFM was used to determine the roughness R_q.

Imaging using SEM was done with an Evo MA10 from Zeiss (Germany). The settings were 15 kV cathode voltage and a probe voltage of 9 pA at a working distance of 3 mm. Prior to this, the sample had to be sputtered with a layer of 15 nm gold.

AFM measurements of top and bottom coverslips before and after the flow chamber experiments were done with a NanoWizard 4 from JPK/Bruker. As cantilever, a ContGB-G (Budgetsensors, Bulgaria) was used in contact mode in air. It had a force constant of 0.3 N/m and a resonance frequency of 13 kHz. Calibration was done with the thermal noise method, which was implemented in the AFM software. The internal z-piezo was used; it moves the complete cantilever holder covering a height difference of 15 µm. A line rate of 0.2 Hz was selected, and the gain of the PID control around was 50. The setpoint

was adjusted to 25 nN. The mean square roughness R_q could be determined from the height profile with the JPK Processing software.

3.2.5 Experimental Setup and Procedure

The PBS bacterial suspension of OD_{600}=0.1 was transferred into a syringe with a Luer-Lock connection and 20 mm diameter under sterile conditions. The syringe was mounted in an Aladdin syringe pump (World Precision Instruments, U.S). Syringe pumps of this type were also loaded with isopropanol and PBS-filled syringes. Both liquid-filled syringes were previously degassed in an ultrasonic bath for 15 min. 0.8 mm diameter Teflon tubings were connected to a multi-way valve (Diba Industries, U.S.) via Luer-Lock and Omni-Lok connectors as shown in Figure 3-2 (b). The valve was also connected to the inlet of a channel of the flow chamber via 0.8 mm diameter tubing. The outlet was routed via tubing into a sealed waste collection bottle with pressure compensation using a 0.2 µm microfilter. The flow chamber was then placed in a well-plate holder of a Leica SP8 inverted confocal fluorescence microscope, as shown in Figure 3-2 (a).
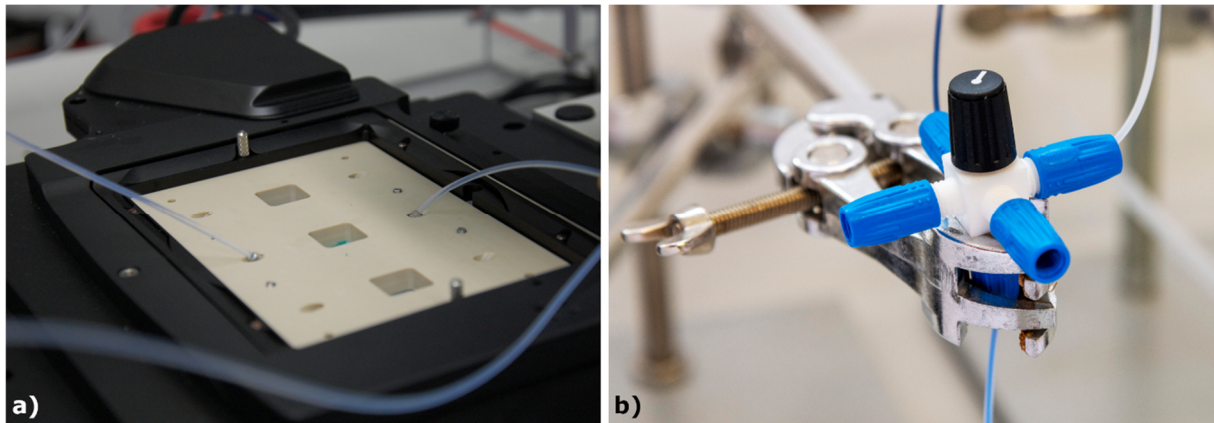
Figure 3-2: Assembled flow chamber in the well-plate holder of a Leica SP8 microscope (a). Five-way valve to switch between bacterial suspension, isopropanol, and PBS during the experiment. The outlet at the bottom is connected to the flow chamber. In the figure, ink was used for visualization (b).

The tubes had been filled with the corresponding liquid up to the valve before the experiment started. The connected flow channel was flushed with 0.2 ml/min isopropanol for 2 min to expel air bubbles. Then, the tubes were rinsed with 0.2 ml/min PBS for 10 min. In the meantime, the microscope was focused on the bottom coverslip with by using transmitted bright-field light. The valve was switched to the bacterial suspension, which was pumped at a 0.01 ml flow rate. After approximately 10 min, the first incoming bacteria could be identified by fluorescence with the objective camera. Two different illumination settings were used for the respective *P. fluorescens* strains and their specific fluorescence. For *P. fluorescens* SBW25 attTn7::P_{A1/04/03}-*gfp2*, excitation was done with a wavelength of 470 nm by a

LED at 30% power for 200 ms exposure time, and the filter cube DFT51010 (dichroic filter: 500 nm, emission: 506–532 nm, Leica, Germany) was chosen. This illumination setting is termed green channel in the following. For *P. fluorescens* SBW25 pMRE-Tn7-155, excitation was done with a wavelength of 550 nm at 30% power for 200 ms exposure, and the filter cube DFT51010 (dichroic filter: 572 nm, emission: 578–610 nm) was used. This illumination setting is termed yellow channel in the following.

After the bacteria arrived, it took another 30 seconds to reach the maximum cell density in the flow channel. The fluorescent light was switched off to prevent bleaching of the dye inside the bacteria. Pumping continued at 0.01 ml/min for the next 30 min. During this time, the bacteria attached continuously. In this time scale, a linear cell number vs. time relationship and the same adsorption rate coefficient can be assumed (Busscher and van der Mei, 2006). After 30 min, the flow channel was flushed for 7 min with PBS at a flow rate of 0.2 ml/min. The higher flow rate caused a higher shear stress acting on the bacteria. Thus, the following evaluation of attached cell numbers refers to the cells which attached to the substrate firmly enough to remain despite the detachment forces. As another consequence of the PBS purging, no bacteria were in the liquid column in the flow channel. Room temperature was maintained throughout the experiment.

Image acquisition was controlled with the microscope's own software LASx. Prior to imaging, the tilt of the coverslips had to be determined with the aid of focus points. It was essential to have a precise setting of each image's focus, otherwise the final automatic image analysis would not have been accurate. Automatic focus setting was done by the piezo driven z-galvo-stage of the microscope. Furthermore, the stage allowed image acquisition at different heights (z-position) to get a z-stack which is necessary for 3D microscopical analysis.

Three to five randomly selected areas of the top and bottom coverslips for ZnO nano- and microstructures and MPL 3D printed microstructures were acquired. That guaranteed sufficient image material with the correct focus set and a high statistical quality. The areas consisted of multiple adjacent images in x- and y-orientation of 211x211 μm² each. At each position, a green or yellow channel image was taken depending on the fluorescence dye of the modified *P. fluorescens* strain. Furthermore, ZnO nanorods were visualized by means of their NBE. ZnO was excited with a wavelength of 385 nm with 30% power for 150 ms exposure time, and the filter cube DFT51010 (dichroic filter: 572 nm, emission: 410 - 440 nm) was applied. This illumination setting will be referred to as the violet channel. Each channel was saved as a 16-bit grayscale image with increased fluorescence emissions displayed as a brighter gray value. The area scans on ZnO microstructures, and the orientation of the 3D printed microstructures are schematically presented in Figure 3-3 a) and b), respectively.
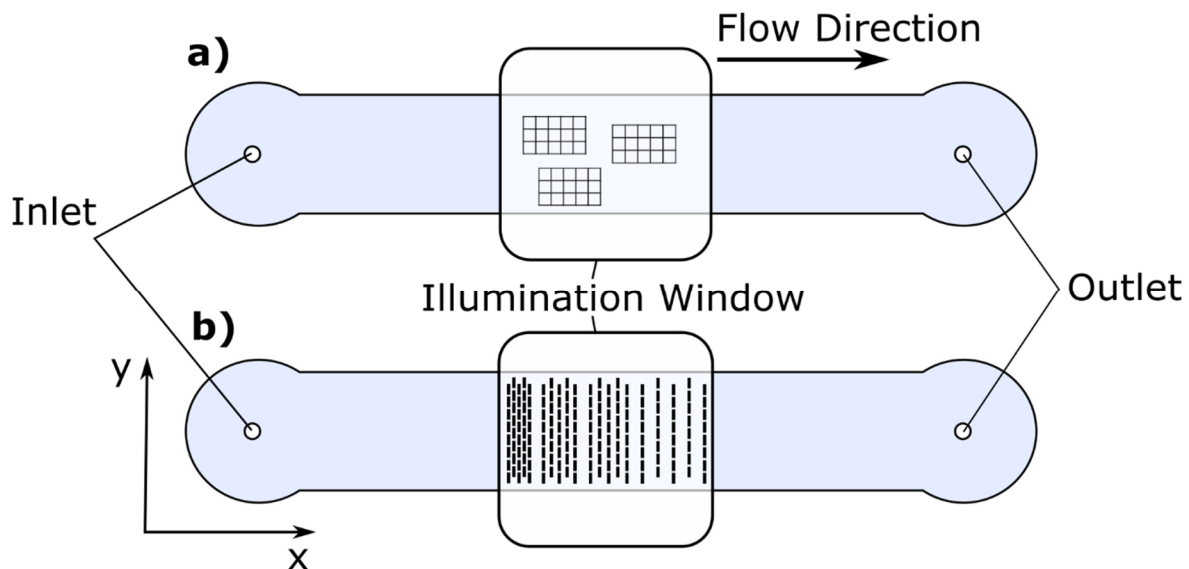
Figure 3-3: Schematic top view illustration of the flow channels. The axes indicate the direction longitudinal (x) and transverse (y) to the flow direction. Arbitrarily chosen area image scans on the substrate types with ZnO nanostructures are shown in a) in the illumination window. In the illumination window of b), four areas with 3D printed microstructures having different spacings are depicted.

3.2.6 CFD Simulation of the Flow Chamber

CFD simulations of the flow behavior in the flow chamber channels were modeled using Ansys 2019 R3 software. The Fluid Dynamics (Fluent) module was used for this purpose. The geometry of the flow channel was derived from the drawing Figure 8-3 (a) in the Appendix. Since the flow behavior is described by values of small volume elements, the flow channel model has to be split into many. That is done by the so-called meshing. The more volume elements represent the entire flow channel, the more accurately the overall flow behavior can be predicted. However, many volume elements require a lot of computer processing power. Since the height of the flow channel was very small in relation to its width and length, the volume elements also had to be flat. The calculation was performed with the Viscous(Laminar) model. Water at a temperature of 23 °C was assumed as the fluid medium. It is a Newtonian fluid with a dynamic viscosity of 0.001003 $kg \cdot s^{-1} \cdot m^{-1}$. The calculations were performed separately for an inlet flow rate of 0.01 ml/min and 0.2 ml/min, each for a steady state case (t→∞). Instead of the volumetric flow rate, the mass flow rate was used in Ansys. These were $1.663 \cdot 10^{-7}$ kg/s and $3.327 \cdot 10^{-6}$ kg/s, respectively. The two flow rates were chosen as parameters because both were selected for the experiment. The flow rate of 0.01 ml/min was used during the bacterial attachment phase and the flow rate of 0.2 ml/min afterwards to detach loosely adhering bacteria. Since the flow chamber design specified a 45° inlet to the flow channel, the inlet vector was also defined to be (1,0,-1). The parameters velocity, Reynolds number, and wall shear as well as the streamlines were considered.

3.2.7 Manufacturing of Tailored Substrates

Three different substrate types for the bacterial attachment experiment were created. These differed in nanoroughness or had edges in the dimension of 1 µm. The chemical composition for all substrate types was the same with ZnO. The substrates were deposited on coverslips which served simultaneously as the base and window for the flow chamber. The pure glass of a coverslip was considered as a reference substrate type. Both large coverslips for the bottom and small ones for the top confinement of the flow channel were prepared.

The first substrate type, ZnO thin films on glass (TF-glass), was developed by a dip coating and calcination procedure, according to Lee et al. (2007). Each coverslip was cleaned thoroughly, as described in section 3.2.2. A solution of 5 mmol/l $Zn(CH_3COOH)_2$ in isopropanol was prepared with $Zn(CH_3COO)_2 \cdot 2H_2O$ treated in an ultrasonic bath for 10 min. The dry coverslips were immersed for 20 s in the solution, cleaned with isopropanol, and dried with N_2. While the gas stream passed over the coverslip, it had to stand upright on tissue paper. This procedure was repeated 4 times. It ensured that a homogeneous layer of adsorbed zinc acetate seedlings was formed on the coverslip. Finally, the coverslip was calcined at 350 °C to form a thin film of ZnO.

A lawn of ZnO nanorods (NR-glass) on coverslips was coated by hydrothermal synthesis, according to Vayssieres (2003). TF-glass coverslips were placed in 50 ml centrifuge tubes. Silicone stoppers placed on the bottom of the centrifuge tube and on top of the coverslips ensured a slightly tilted position with the side of interest facing down. The centrifuge tubes were filled with an equimolar solution of 0.05 mol/l $Zn(NO_3)_2$ and Hexamethylenetetramine in diH_2O, closed, and placed in a heated water bath at 85 °C for 1 h. Finally, the coated coverslips were washed in an ultrasonic bath three times for 10 min in diH_2O.

Arrays of ZnO nanorods (aNR-glass) were prepared by a newly discovered route. It was based on microcontact printing. The required PDMS stamp had the design shown in Figure 3-4. With the stamp, the zinc acetate crystallization seeds could be placed on the coverslip in a precise manner. For this purpose, the PDMS stamp was first cleaned for 10 min in acetone and diH_2O ultrasonic bath. After the stamp was free of liquids by drying with N_2, it was immersed for 1 min in the zinc acetate solution described earlier. It was then compulsory to dry the stamp completely with N_2. Any remaining alcohol would cause blurring of the final pattern. The dry stamp was pressed in the center of the coverslip with a weight of 200 g for 1 min. The following procedure of calcination and nanorod synthesis was the same as for NR-glass. As a result, 10 µm x 10 µm arrays of ZnO nanorods were deposited on the glass surface with interspaces of 10 µm between the arrays. A top view resembled the contact surface of

the PDMS stamp. Finally, aNR-glass was coated with a ZnO thin film as for TF-glass to ensure the same chemical composition over the whole substrate.
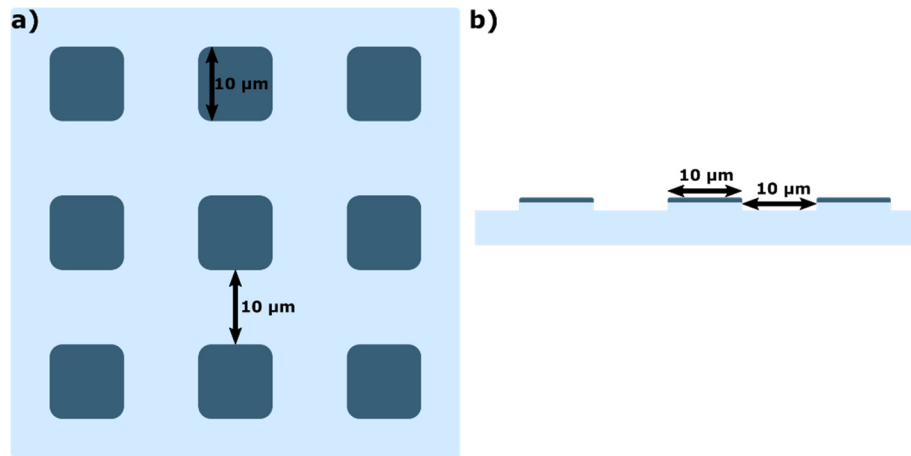
Figure 3-4: Schematic illustration of the PDMS stamp for microcontact printing loaded with the ZnO seed solution. The zinc acetate seed solution is shown in dark blue. Top view a) and cross section b).

All ZnO coated substrates had to be cleaned at the outsides with NaOH, as described in section 3.2.2. The reason for this procedure is ZnO nanostructures and nanoparticles, which grow without the specific ZnO seeds during the synthesis on the coverslips. Such particles prevent plasma bonding of the coverslip and channel element. Hence, all coverslips were stored in a dry and dust-free environment until assembly and use.

3.2.8 Evaluation with ImageJ and Statistical Data Analysis

The area scans of the fluorescence microscopic image acquisition were saved as .tif-stacks with 16-bit grey scale separated into their channels. The image stacks could be loaded into Fiji/ImageJ using the BioFormats importer plugin. A self-written ImageJ-macro script (see 8.2 in Appendix) was used to count the bacteria cells on each image of the green channel, and for aNR-glass, assign them to their corresponding substrate type: nanorods or interspace. The script with comments is attached in the Appendix. It was developed for the 64-bit version of ImageJ 1.53c. Loaded image stacks were first prepared for processing during the execution of the script. Various filters and plugins of the ImageJ toolbox were called for this purpose: background subtraction was done, followed by an optimization of the contrast. The images were finally converted into binary images so cells could be automatically counted with the *Find maxima* plugin. The data was written to a text file, which could be analyzed with software like Origin.
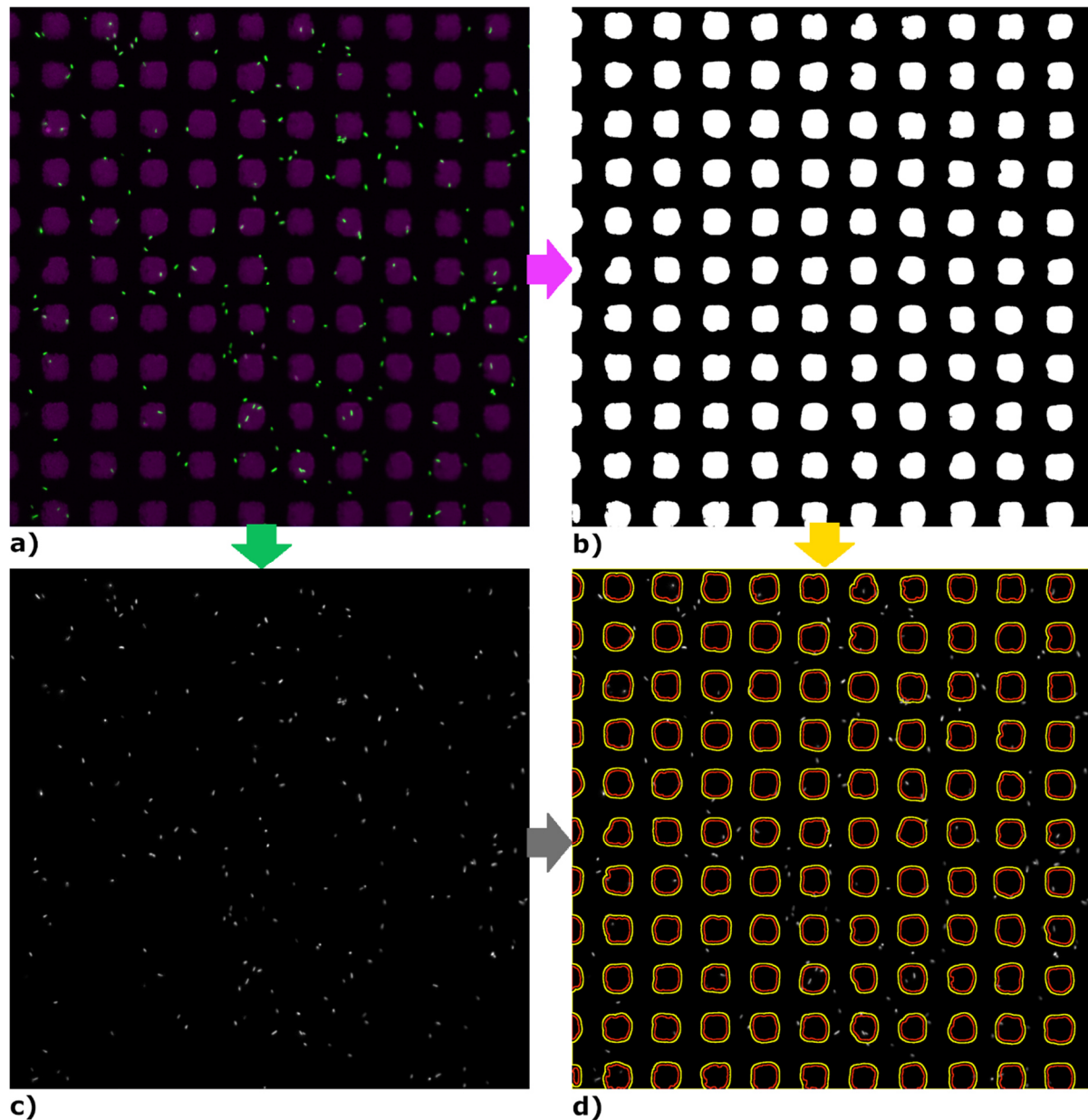
Figure 3-5: A single image from an area scan stack taken with a fluorescence microscope. The violet and green channel are colored and superimposed for visualization. Green are the bacteria and violet are the nanorod arrays (a). The fluorescence microscope captures the violet channel (b) and the green or yellow channel separately depending on the fluorescence dye of the bacterial strain (c). Both are already processed and binarized with the ImageJ macro script. The violet channel can be used to create a mask, which is assigned to the green channel (d). Regions outlined in red are used to evaluate the number of cells on the nanorods, and regions outlined in yellow are used to evaluate the number of cells in the interspace.

In the case of aNR-glass, the violet channel images are also processed as greyscale images, whereas brighter zones result from the nanorods' NBE emission. The thin film interspaces showed no NBE emission and thus occurred black. The processed greyscale images were converted into binary images. The violet channel, prepared in this way, could be used as a mask that was superimposed on the green

channel. The mask was reduced or enlarged by half the bacterial length, 0.5 μm, to count the bacteria on the nanorods and in the interspace, respectively. Due to the adjusted counting areas, the sharp border becomes a border region in the transition between the interspace and nanorod domain. This border region was introduced as bacteria could not be unambiguously assigned to a substrate type when overlapping with the nanorods and interspace at the same time. The cell count in the border region can be determined by subtracting the cell count on the nanorods and in the interspaces from the total cell count. The image manipulation steps in the evaluation procedure are shown graphically in Figure 3-5.

The bacterial counts of each image were normalized to mm². For illustration: if one bacterium appears in the image, the normalized cell number is approximately 22 per mm^2. This approach was necessary as the cell count scales generally with the field of view: more cells are counted with a larger size. The field of view's size depends on the used microscope's ocular and objective. In the case of this project each field of view or the image, respectively, had the dimensions of 211 x 211 μm^2. Furthermore, cell count normalization was necessary for the heterogeneous substrates of aNR-glass. The substrate types filled different amounts of area in each field of view. Generally, the interspace region was the largest and the border region the smallest. To eliminate the influence of the area, the number of bacteria had to be assigned to the substrate and related to this area.

The normalized cell numbers could be used to evaluate the substrate's effectiveness to inhibit the onset of biofilm formation. This was possible because the onset of biofilm development was determined by the bacteria that attached and withstood high shear stress (bacterial retention). Since the individual normalized cell counts had little meaning, they had to be combined in data sets, and these had to be compared using statistical methods. This procedure is described in the following paragraphs. However, during the data evaluation, it turned out that the systematic procedure had to be aborted at one step. This issue will also be addressed in the following. A summarized schematic illustration from data acquisition to result visualization is shown in Figure 3-6.

The cell number in an area was tested for outliers using a Grubbs outlier test followed by a Shapiro-Wilk test for normal distribution. Three areas of either the bottom or top coverslip were counted, giving in total six image area data sets (iaDS) for one replicate (2 in Figure 3-6). The three iaDSs for either the top or bottom coverslip were combined into one replicate data set (rDS). Subsequently, the rDS was again tested for normal distribution, but kernel regression was applied for data presentation (3 in Figure 3-6). The experiments with their two rDSs for the bottom and top coverslip of one substrate type are technical replicates. At least three replicates were analyzed for each substrate type.
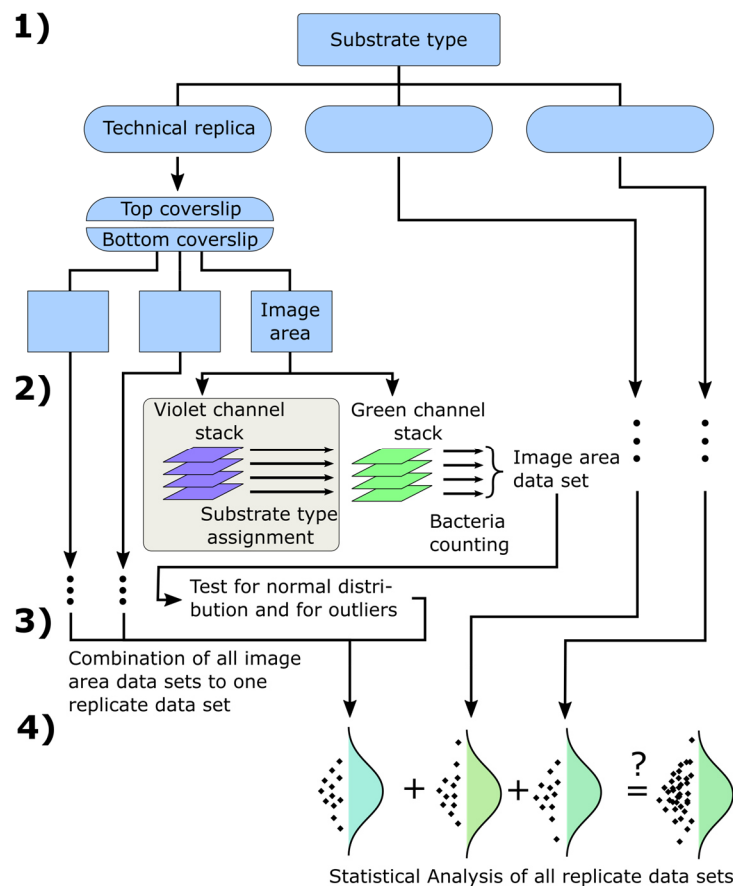
Figure 3-6: Schematic workflow illustration from data acquisition to result visualization for one substrate type. For each substrate type, 18 image areas in total were acquired for the bottom and top coverslips of all technical replicates 1). Each image area was processed in ImageJ to get a data set with the normalized bacterial counts. For aNR-glass, substrate type assignment was done additionally (greyed part) 2). The three data sets of one technical replicate were merged into a replicate data set 3). Similarity with the other replicate data sets, which were processed the same way, was tested with ANOVA, and if similarity holds, the three replicate data sets were combined to one substrate data set to allow comparison between different substrate types 4).

The rDS of the technical replicate were tested for similarity with analysis of variance (ANOVA) to identify if each replicate resembles the other. For this purpose, the null hypothesis should not be rejected. The null hypothesis is: the arithmetic mean cell numbers per mm² are significantly similar within one substrate type. Two different one-way ANOVAs were performed using the groups of bottom coverslips and top coverslips. The degree of freedom (DF) of a certain hypothesis test is given in the results section. The significance level was 0.05 for all hypothesis tests. The general ANOVA was done with an F-test. F-values higher than F≈1 increase the probability of denying the null hypothesis. Suppose F>>1, a post-hoc test was applied to check the pairwise group combinations.

After this evaluation step, it turned out that the next step to enable comparison on the level between the substrates could not be performed due to the actual data situation of the experiments. Hence, the later presented results will be based on the last evaluation step (3) using the individual rDSs. However, the intended next evaluation step will be addressed shortly.

To compare the effectiveness of the substrate types in reducing bacterial attachment and retention, significant differences in bacterial number had to be considered. Therefore the rDSs of all technical replicates needed similarity to merge all to one substrate type data set (stDS) reflecting the situation on the top or bottom coverslip of one substrate type. ANOVA of the stDSs could be used to test for non-similarity of the substrate types (4 in Figure 3-6).

3.2.9 Dissolution Analysis of ZnO

Since ZnO is considered to be toxic to some bacteria species due to the release of soluble Zn^{2+} ions, the zinc concentration in the flowing liquids had to be measured. The solubility of ZnO in the flow chamber experiment was measured for TF-glass and NR-glass. Both diH_2O and PBS were investigated as potential solubilizing media. For this purpose, the channel of the flow chamber was flushed for 2 min with the respective medium at 0.2 ml/min. This preliminary flow was discarded. Then, the channel effluent of 5 min at a flow rate of 0.01 ml/min was collected and measured five times for Zn^{2+} ion mass concentration and averaged. The effluents of two different channels, each of TF-glass and NR-glass, were taken.

The analysis was performed using a Thermo Scientific iCAP Qc inductively coupled plasma mass spectrometer. The sample introduction system used a standard Peltier cooled, quartz cyclonic spray chamber, a quartz concentric nebulizer, and a demountable quartz torch with a 2.5 mm ID quartz injector. Standard Ni samples and skimmer cones were also used. For interference-free detection of all stable Zn isotopes, all measurements were carried out in both standard mode and single collision cell mode, with kinetic energy discrimination, using pure He as collision gas. The instrument was operated using the following parameters: Forward power 1550 W, Nebulizer gas (STD/KED) 1.14/1.08 l/min, Auxiliary Gas 0.6 l/min, Cool Gas 14 l/min, Injector 2.5 mm ID, Cell gas flow 4.9 ml/min He and 140 Ce.16 O/140 Ce (Oxide rate) 1.5 %. $Zn(NO_3)_2$ was used for calibration, and the mass of zinc in the calibration solutions was adjusted to 1, 5, 10, 100, and 1000 µg/l.

3.3 Part II: Bacterial Attachment and Retention under Micro-hydrodynamic Effects

For the experiments with the 3D printed microstructures the general methods of sections 3.2.1 to 3.2.6 apply. The specific methods for this type of surface structures are addressed in the following.

3.3.1 CFD Simulation of Hydrodynamics at 3D Printed Microstructures

Micro-hydrodynamic situations on surfaces can be created by structures that present obstacles to a flowing fluid, leading to turbulence and increased shear stresses. CFD simulations can be used to provide information about such hydrodynamics, and on their basis, surface structures can be tailored. A systematic investigation can be ensured by simple structures with one variable parameter, which is supposed to have a significant influence, according to the literature. Based on the literature, cuboidal-shaped blocks positioned with the longest side transverse to the flow direction (y-direction) were chosen as a starting point. The dimensions of the blocks were: 10 µm length, 5 µm height, and 1 µm width. In the y-direction, gaps of 1.5 µm were provided to account for the influence of transverse flows as described in Choi et al. (2018b). After each row, the next was staggered by a half-length of the blocks and a half-gap in the x-direction. The spacing between each row was chosen as the variable parameter since it influences the turbulences between the blocks. CFD simulations were performed for the spacing of 1 µm, 2 µm and for each of the next 2 µm larger up to 16 µm. In the upper third, the blocks converged to form a ridge on the long side of the blocks. This sharp edge is intended to provide increased shear stresses and thus, additionally reduce the attachment of bacteria.

The fluid simulation was done with Ansys. For this purpose, the structures described above were designed as 3D elements with increasing spacings in the aforementioned channel element. The volume flow was set either to 0.01 ml/min ($1.663 \cdot 10^{-7}$ kg/s) or to 0.2 ml/min ($3.327 \cdot 10^{-6}$ kg/s), and liquid water was assigned as fluid. As for the simulation of the entire flow channel in section 3.2.6, two flow rates were chosen because the bacteria were affected differently by both. The low flow rate of 0.01 ml/min prevailed during the bacterial attachment phase and the flow rate of 0.2 ml/min induced higher shear stress affecting the attached bacteria. A standard k-omega model with low Reynolds number correction was used as it provides better treatment of the turbulences. For the turbulence, the intensity was chosen at 28%, and the hydraulic diameter with $1.3 \cdot 10^{-4}$ m. The dimensions of the calculated volume elements were smaller in the vicinity of the structures to increase the accuracy in this region of interest.

3.3.2 Fabrication of 3D Printed Microstructures

Structures in the shape of blocks with rounded ridges were fabricated with MPL Laser Nano Factory (Femtika Ltd., Lithuania) equipped with an Erbium-doped femtosecond fiber laser (Menlo, Germany) emitting at 780 nm at the repetition rate of 100 MHz. Beam focusing was achieved with an oil-immersion objective with a 1.4 numerical aperture (Plan Apochromat 63×, ZEISS, Germany). Laser power and scanning velocity were set at 7 mW and 5000 µm/s, respectively. Hatching of 0.1 µm and slicing of 0.2 µm were used to ensure high crosslink overlap of the patterns. The drop of SZ2080 photoresist was placed in the center of the coverslip, baked for 2 h at 60 °C, and then subjected to microstructuring applying the MPL technique. After printing, the non-crosslinked photoresist was removed by immersion of the coverslip in methyl isobutyl ketone for 40 min with multiple solvent exchanges.

The instructions for the MPL device were based on a .stl file with 3D models of the structures. The dimensions of the 3D models were adapted from the fluid simulation. The rounded top ridge was not modeled in the file but was a consequence of the MPL printing characteristic. Between the blocks in the longitudinal x-direction was a spacing of varying sizes (1 µm, 4 µm, 8 µm, and 14 µm). The instruction file contained repeated blocks of one uniform block spacing which extended 250 µm in the x-direction and 235 µm in the y-direction. In the y-direction followed, after a small blank area, the next area with increased spacing. Thus, the file contained four block spacings in y-extension, which sums up to 1100 µm. The x-y dimensions were chosen to match the microscopes field of view of 211x211 µm². For multiple image acquisition, the structures were stitched in the y-direction to those already printed by repeatedly executing the .stl file. The final y-dimension was 5 mm, which enabled the acquisition of 20 images for every four block-spacings. The microstructures were printed on the center of coverslips with 50 mm length, 24 mm width, and 0.17 mm thickness. In the experiment with the microfluidic flow chamber, the liquid flowed in the x-direction. Hence, the blocks were aligned transversely to the flow. A schematic top view of the 3D printed structures is presented in Figure 3-3 b).

The unreacted photoinitiator, which remained in the product, led to overexposure in fluorescence microscopy. Hence, photobleaching was chosen to reduce the overall fluorescence of the sample. That was done by illuminating with an LC8 UV-lamp (Hamamatsu, Washington, USA) at a distance of 10 mm for 16 h. An internal A9616-05 filter was used to restrict the bandwidth to 350-400 nm. It blocked short-wave UV radiation that may have a damaging effect on the polymer. Finally, the photobleached samples were imaged with fluorescence microscopy to evaluate whether the background emission by the photoinitiator was sufficiently reduced.

3.3.3 Evaluation with ImageJ and Statistical Data Analysis

The evaluation workflow for the attached *P. fluorescens* SBW25 pMRE-Tn7-155 on 3D printed microstructures was done for five technical replicates and resembled the one for the replicates of ZnO substrate types. The schematic illustration in Figure 3-6 also applies to this evaluation. However, imaging was done only for the yellow channel since the used strain was fluorescent in this band region. Furthermore, instead of randomly selected image areas with one image at each position, up to 20 z-stacks per microstructure area were acquired. Each z-stack consisted of two images in different heights or z-ranges, respectively. That led to a total stack of 2 x 20 images for each specific block spacing per experiment. The images taken at the surface between the structures are labeled z=0 μm, and those taken at the height of the block ridges are labeled z=5 μm (see markings in Figure 4-18 a).

The counted bacteria per image were compiled in two rDSs for one z-stack of each block spacing: one for z=0 μm and one for z= 5μm. ANOVA was used to test for the similarity of rDSs between replicates. Furthermore, the summarized bacterial number at each image position consisting of the count at z=0 μm and z=5 μm was evaluated. The effectiveness of preventing bacteria attachment of a certain spacing could be derived from comparing summarized bacterial numbers, where the lowest count indicated the most effective spacing. For this, the rDSs of the respective block spacings should be combined, as was intended for the substrate types in section 3.2.8 (4. in Figure 3-6). However, the actual data of the experiments with the 3D printed microstructures did not allow this either, as for the ZnO nano and microstructured surfaces. Hence, only the four rDSs within each technical replicate were compared.

3.4 Part III: Lipopolysaccharide Encapsulates Polystyrene Microparticles

3.4.1 Preparation

The as-delivered PS microparticle suspension was diluted with diH$_2$O to 10 mg/ml. The *P. aeruginosa* LPS was dissolved in diH$_2$O at a concentration of 4.33 mg/ml. 100 μl of the diluted PS suspension was mixed with different volumes (12–231 μl) of the LPS solution to reach LPS concentrations of 0.07 mg/ml, 0.14 mg/ml, 0.36 mg/ml, 0.71 mg/ml, 1.07 mg/ml, 1.43 mg/ml. Accordingly, the samples were designated as S1–S6. After filling up with diH$_2$O to 600 μl, 100 μl THF was added. The dispersion was shaken for 30 min at room temperature in 1.5 ml reaction tubes with a vortex-mixer (Select Vortexer, Select BioProducts, U.S.). Subsequently, separation was performed by centrifugation at 5000 rcf for 5 min using a Z 206 centrifuge (Hermle Labortechnik, Wehingen, Germany), removing supernatant and refilling with deionized water. This step was performed in total three times to obtain

LPS-PS particles s an aqueous suspension. In parallel, a PS microparticle suspension subjected to the same swell-capture cycle without the addition of LPS was used as a control sample designated as S0.

3.4.2 Characterization – ζ-potential, Surface Chemistry and Surface Topography

For the ζ-potential measurements, 100 µl of microparticle suspensions S0–S6 and LPS solutions with the same concentrations were mixed with 900 µl of PBS (pH 7.4). The measurements were performed at 25 °C with a Zetasizer Nano ZS (Malvern Instruments Ltd, U.K.).

X-ray photoemission spectroscopy (XPS) measurements were performed on drop-casted specimens. For this purpose, 15 µl dispersion of samples S0–S6 was dropped on a cleaned silicon wafer and dried under vacuum. The silicon wafers were previously cleaned by immersion for 10 min in a mixture of deionized water, NH_3, and H_2O_2 (in the ratios of 5:1:1) at 80 °C, rinsing two times in deionized water in an ultrasonic bath and drying with N_2. Analysis was performed at least on two replicates with an AXIS Ultra DLD photoelectron spectrometer manufactured by Kratos Analytical (Manchester, U.K.) with monochromatic Al Kα radiation (hv = 1486.6 eV) at a pressure of approximately $5 \cdot 10^{-7}$ Pa. The electron emission angle was 0° and the source-sample-analyzer angle was 60°. The binding energy scale of the instrument was calibrated following a Kratos Analytical procedure which uses ISO 15472 binding energy data. The XPS spectra were taken by setting the instrument to the hybrid lens mode and the slot mode providing approximately a 300 × 700 µm² analysis area. The survey and high-resolution detail spectra were measured with pass energies of 80 eV and 20 eV, respectively. All spectra were recorded in the fixed analyzer transmission mode. Furthermore, the charge neutralizer was used. The spectra were referenced to the main C1s peak at 284.9 eV. UNIFIT 2018 was used for data analysis (Hesse, 2018). Peak fitting was performed with a sum of the Gaussian-Lorentzian curves with a fixed Gaussian-Lorentzian ratio and a halfwidth. For the background subtraction, a modified Tougaard background was used. The quantification was performed with the survey spectra. Therefore, the peak areas of the main peaks after subtraction with a modified Tougaard background were normalized with the element-specific Scofield factor, the spectrometer-specific transmission function and the inelastic mean free pathways of the photoelectrons.

Fresh mica stripped gold was prepared according to Wagner et al. (2002) for AFM measurements. Therefore mica stripes were cleaved, and the inner freshly exposed layer was placed into a holder of a vacuum deposition machine (Creavac, Germany). At a pressure of 10^{-6} bar, Au was deposited at 1 Å/s to a thickness of 100 nm with the thermal evaporation device. Coverslips were glued with epo-tek 377 on the gold layer and heated for 1 hour at 150 °C. After cooling, they were stored until use. To cleave

the gold before usage, THF was dropped in between the gold-mica interphase and the mica was carefully stripped of.

Infrared Nanospectroscopy (AFM-IR) measurements were performed using a NanoIR2s (Bruker / Anasys Instruments) coupled with a multichip QCL source (MIRcat, Daylight Solutions; tunable repetition rate range of 0–500 kHz; spectral resolution of 1 cm^{-1}). The range from 900 cm^{-1} to 1900 cm^{-1} was analyzed using an Au-coated silicon probe (tapping AFM-IR cantilever, Anasys Instruments, spring constant 1-3 nN/m).The specimen was prepared by dropping 15 µl of the dispersion of samples S0–S6 on fresh mica stripped gold substrate and dried under vacuum to get areas of closely packed microparticles. At the upper curvature of individual particles, single point measurements were conducted.

AFM height measurements were performed with dried microparticles on Au. Therefore, freshly exposed Au surfaces were coated each with 15 µl of LPS-PS microparticle suspension of the samples S0–S6 or pure PS microparticle suspension. The coated surfaces were dried in a vacuum while being lightly swirled. Areas of densely packed microparticle monolayer were scanned through a series of AFM images that gradually increased in spatial resolution. High-resolution topography analysis was done by measuring areas of 500 x 500 nm^2 and 250 x 250 nm^2 on the upper sphere surface of individual microparticles within the grid. The high-resolution measurements were enabled by using a Nanowizard 4 system (JPK, Bruker Nano GmbH, Berlin, Germany) in higher overtone AC mode, employing AD-2.8-SS (Adam Innovations, Ireland) cantilevers. The cantilever was vibrated at its second resonance frequency, specifically at 325.16 kHz. Calibration was carried out using the thermal noise method incorporated into the Nanowizard 4 control software. The spring constant k_2 and sensitivity S_2 for the second resonance frequency were determined as 49.88 N/m and 8.2 nm/V, respectively. The power-law exponent ζ_2, according to Labuda et al. (2016), was calculated as 1.98. Scanning was conducted at a line rate of 0.6 Hz with a 2 nm drive amplitude. It was crucial to use low pressure with a relative setpoint of 85–90 % and a low gain. Data visualization was accomplished using JPK Data Processing 6.1.88 software. Here it should be mentioned that the flattening of a spherical top leads to distortion in the resulting projected 2D topography images. One way to overcome this problem is the first derivate image of the measured height.

3.4.3 Labeling of Encapsulated Microparticles with FITC

Fluorescein isothiocyanate (FITC) labeled microparticles were prepared by mixing a 20 µl stock solution of FITC (20 mg/ml in ethanol) with 100 µl of a microparticle suspension. Then, 380 µl borate buffer (0.1 M, pH 10.5) was added. The reaction tubes were placed in a Thermomixer-Mixer HC (Starlab,

Milton Keynes, U.K) and rotated at 800 rpm at 37 °C for 3 hours. After incubation, excess FITC was removed by centrifugation at 5000 rcf for 10 minutes using a MiniSpin plus centrifuge (Eppendorf, Germany), discarding the supernatant and refilling with ethanol. This step was performed three times. Subsequently, the same procedure was repeated with diH$_2$O to get an aqueous microparticle suspension.

Imaging of the FITC-labeled microparticles was done with a fluorescence microscope (Leica SP8, Germany). The liquid sample on a coverslip was excited with an LED light source with a wavelength of 470 nm and the filter cube DFT51010 (dichroic filter: 500 nm, emission: 506–532 nm, Leica, Germany) was used for detection.

4   Results and Discussion

4.1 Part I: Bacterial Attachment and Retention on Nano- and Microstructured Surfaces

4.1.1 Evaluation of the Flow Chamber CFD Simulation

The microfluidic flow chamber was modeled using Ansys software, and the flow behavior was simulated. Two volume flows were calculated separately. A low flow rate of 0.01 ml/min and a high flow rate of 0.2 ml/min.

Figure 4-1 a) and b) show the velocity distribution in a channel cross section of the central region. A velocity profile emerged independently of the flow rate's magnitude. The flow velocity was highest in the middle zone, while the velocity approached zero at the wall. For a flow rate of 0.01 ml/min, the average velocity in the channel was 0.28 mm/s. The flow velocity in $z = 50$ μm was 0.42 mm/s, and in $z = 0.5$ μm (nearby bottom coverslip) as well as $z = 99.5$ μm (nearby top coverslip) 0.016 mm/s. For a flow rate of 0.2 ml/min, the average velocity in the channel was 5.56 mm/s. The flow velocity in $z = 50$ μm was 8.35 mm/s, and in $z = 0.5$ μm as well as $z = 99.5$ μm, it was 0.317 mm/s.
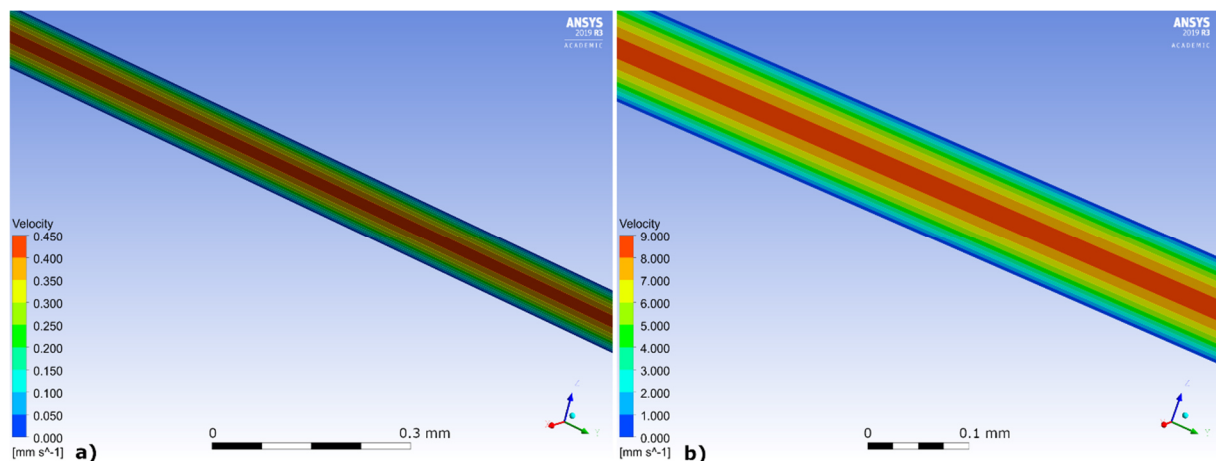
Figure 4-1: Flow velocity in the channel, steady state condition simulated with Ansys. Clipping of the channel cross section for flow rates 0.01 ml/min (a) and 0.2 ml/min (b). The cross section is from the center where the images of the attached bacteria were taken. The coverslips are adjacent at the top and bottom to the zones of slow flow rate.

With the flow velocity, the shear stress correlated. Larger differences in flow velocity between the wall and center lead to higher shear stress. Figure 4-2 shows the shear stress on the walls of the channel.

The wall shear stress was greater for the higher flow rate of 0.2 ml/min than for the lower flow rate of 0.01 ml/min. At the lower flow rate of 0.01 ml/min, the wall shear stress was weaker than for the higher flow rate of 0.2 ml/min. Attached bacteria on the coverslip, in z-position 0.5 µm or 99.5 µm, would have been exposed to a shear stress of 0.017 N/m^2 at 0.01 ml/min and 0.317 N/m^2 at 0.2 ml/min. Multiplication with the viscosity accounts for a shear rate of 18 s^{-1} and 356 s^{-1}, respectively. The shear stress was predominantly the same at the surfaces in the middle rectangular segment of the channel. Only at the side walls the shear stress decreased. However, this area was not considered in the experiment. The images with the microscope were taken in a region centrally on the top and bottom walls of the channel (compare also Figure 3-3). The uniform shear stress values suggest that attached bacteria in the examination region were exposed to the same forces.
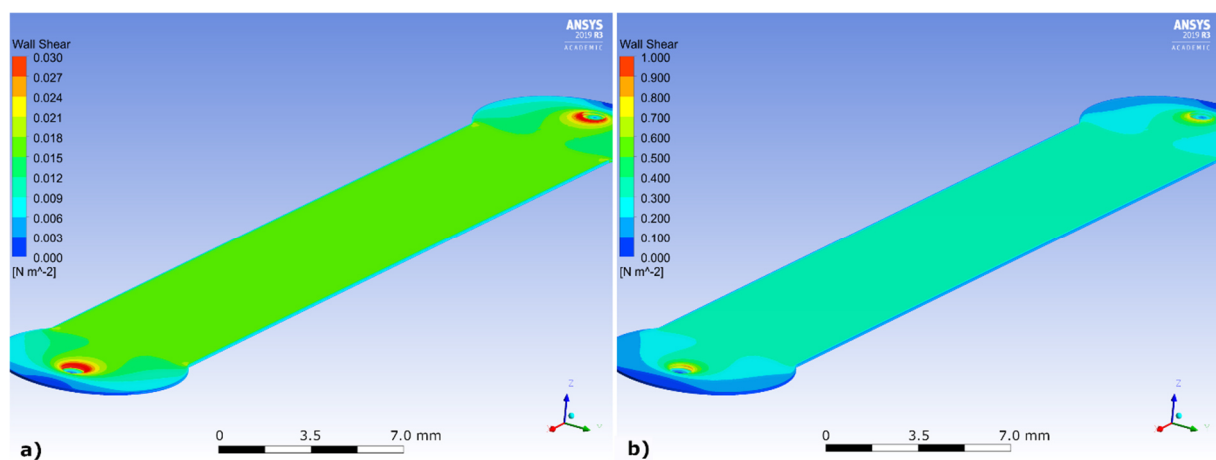
Figure 4-2: Wall shear in a channel for a volume flow of 0.01 ml/min (a) and 0.2 ml/min (b), steady state condition simulated with Ansys.

The Reynolds number can be calculated for the entire channel; however, this value is an average over the entire flowed element. Another option is to use the mesh that was created to calculate the channel. Thus, a Reynolds number can be calculated for each volume element. Figure 4-3 depicts the Reynolds numbers for volume elements that had a dimension of 5 µm in the z-range. The Reynolds number was largest in the center and approached zero at the walls. Since it was proportional to the flow velocity according to equation (6), the Reynolds number resembled the velocity profile. The Reynolds numbers at a flow rate of 0.2 ml/min ranged from 0.028 at the coverslips to 0.23 at the center, which was larger than at a low flow rate. At 0.01 ml/min, they were between 0.001 at the walls and 0.012 in the center. The small values for the Reynolds number, $R_e \ll 2000$, suggest that a smooth laminar flow was present in the center region of the flow channels.

Laminar flow behavior can also be concluded from the streamlines. They indicate the path and velocity of a fluid particle with time. Figure 4-4 presents the streamlines for the different volume flows. It is apparent that the velocity within a flow layer remained constant shortly after the inlet. Simultaneously,

the courses of the streamlines were parallel in the inner rectangular channel segment. Just before the outlet, the streamlines changed, and with it, the velocity vectors.

The physical quantities discussed above describe the flow behavior in the investigated area of the channel as homogeneous and constant. Thus, it can be concluded that the bacteria at both the top and bottom coverslips experienced the same lateral forces at all points throughout the region. Only gravitation, which acted perpendicular to the flow, had a differing influence. However, it was constant for both the top and bottom coverslip. Hence, the probability that a bacterium attached to the coverslip was the same everywhere, and a normal distribution could be assumed.
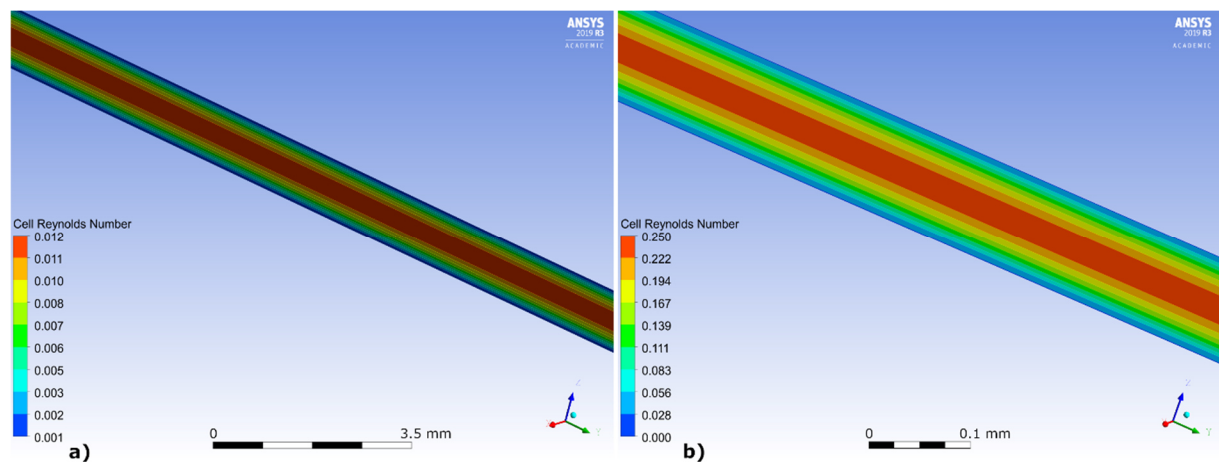
Figure 4-3: Reynolds number of volume elements, steady state condition simulated with Ansys. Clipping of the channel cross section for flow rates 0.01 ml/min (a) and 0.2 ml/min (b).
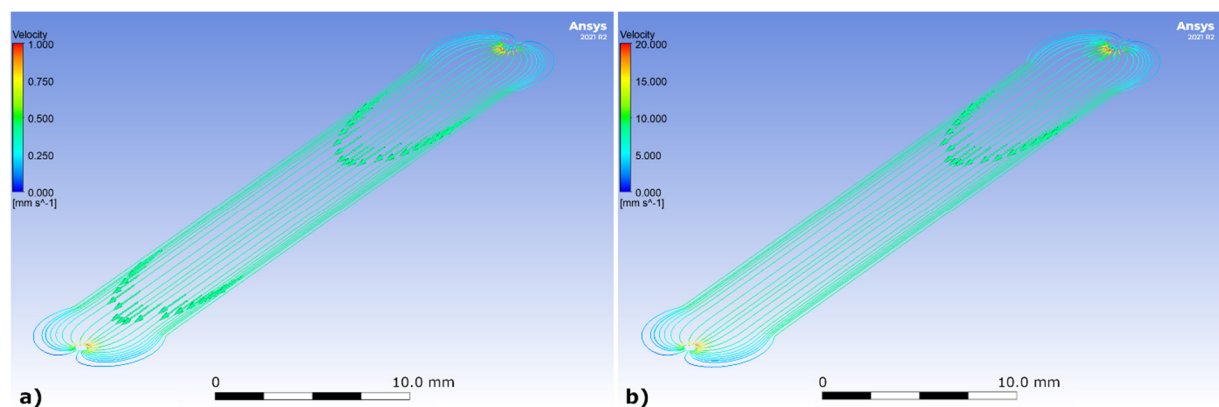
Figure 4-4: Streamlines with flow direction vectors, starting from the inlet, for the flow rates 0.01 ml/min (a) and 0.2 ml/min (b), steady state condition simulated with Ansys. The velocity differences in the mid-channel region result from the z-position of the streamlines. Thus, streamlines closer to the wall of the channel appear slower, which can be deduced from Figure 4-1.

4.1.2 Imaging of the Investigated Substrate Types

The surface structures on the coverslips and the coverslip itself were imaged by AFM and SEM. Figure 4-5 (a) shows the ZnO nanorods of NR-glass from above. They were hexagonal in cross section and about 50 - 100 nm wide. They had a length of 0.7 - 1 µm and stood mostly upright and closely packed to each other, as seen in Figure 4-5 (b). A typical distribution of lengths can be derived from the cross section of ZnO nanorods shown in Figure 4-6. The root mean square roughness could be derived with the JPK DATA Processing software: R_q = 100 – 130 nm.
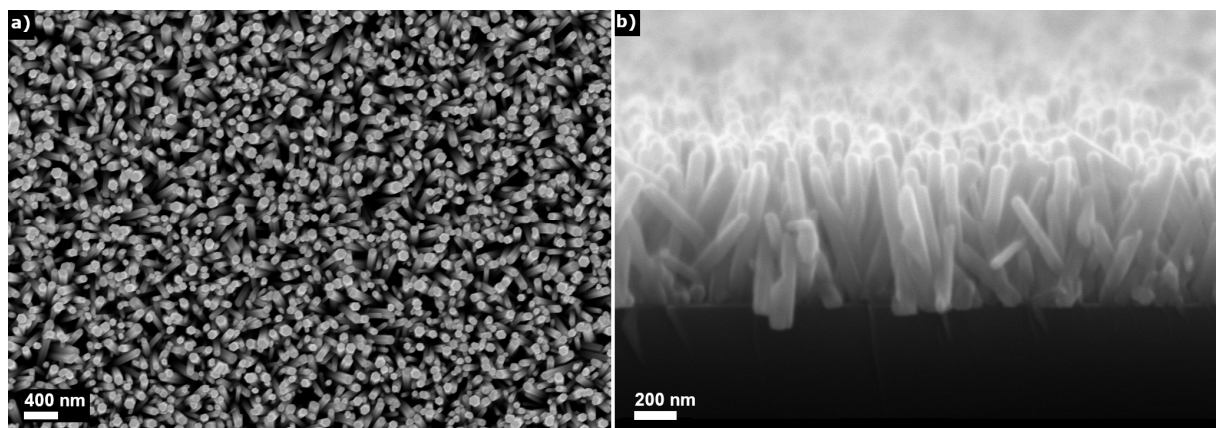
Figure 4-5: Scanning electron microscope images of ZnO nanorods on a coverslip (NR-glass). Scanned from above (a) and cross section (b).
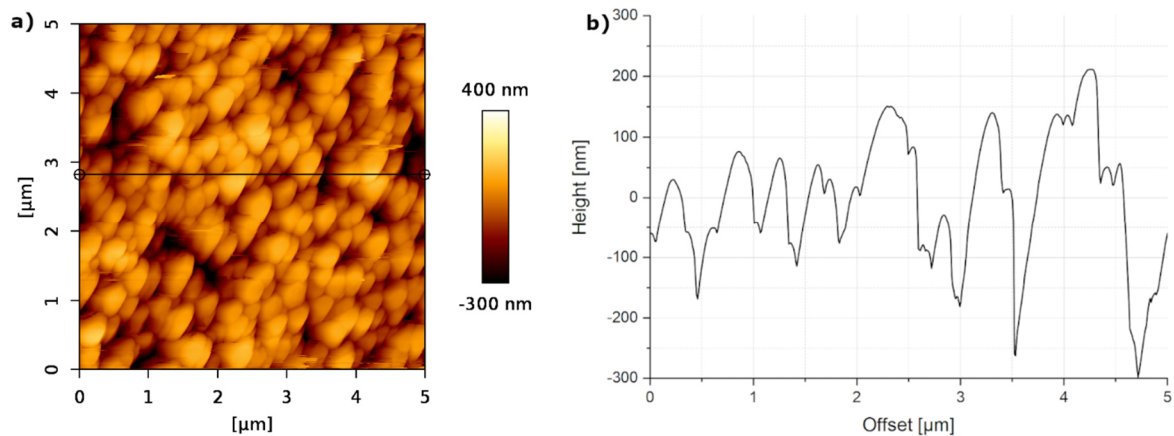
Figure 4-6: AFM image of ZnO nanorods on a coverslip (a) and its cross section (b).
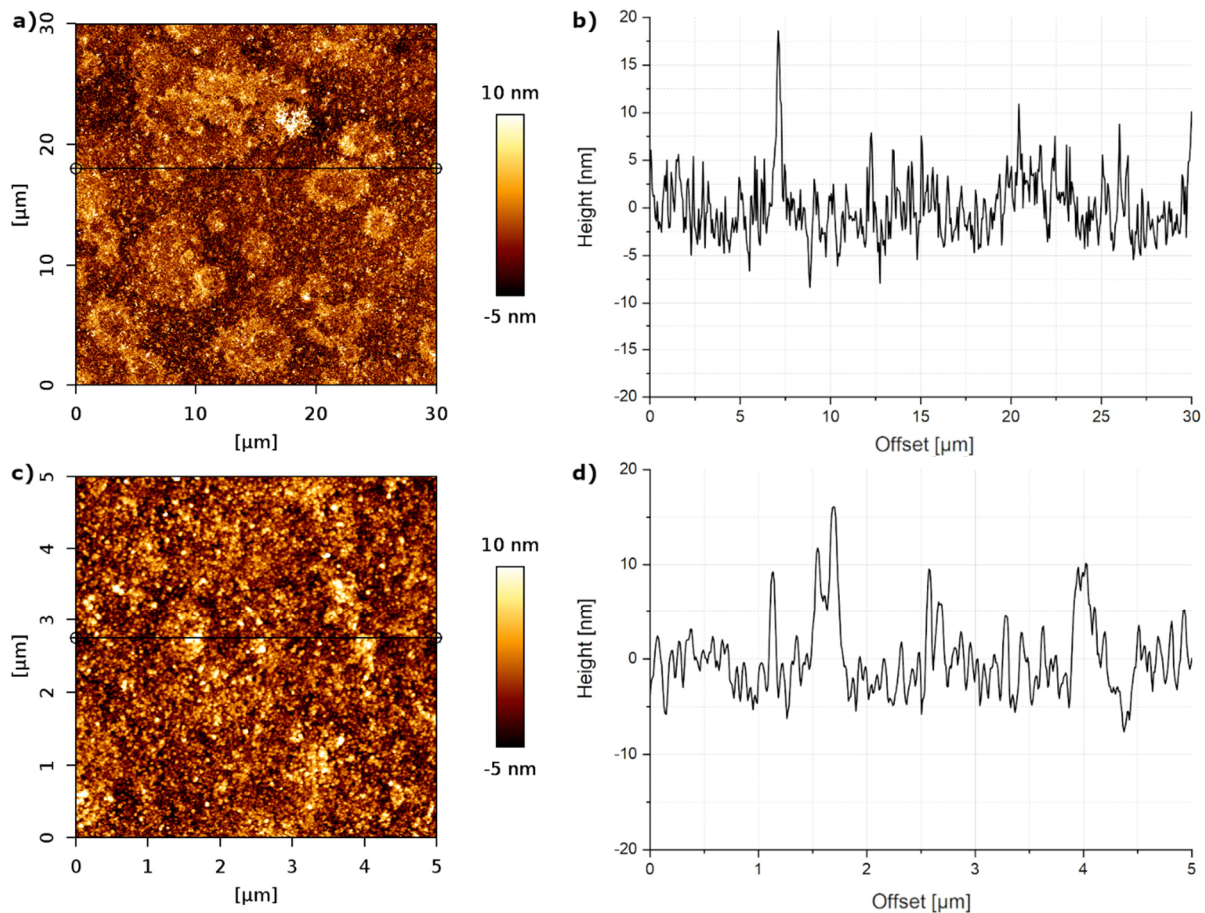
Figure 4-7: AFM image with different resolutions of TF-glass, a layer of ZnO nanoparticles, (a) and (c), and their cross sections (b) and (d).

The surface of a TF-glass scanned with an AFM is shown in Figure 4-7 for different resolutions. In fact, the thin film turned out to be an almost homogeneous coating of ZnO nanoparticles adhering to each other. The particles had a size of about 1 nm to 10 nm judging from the cross section (Figure 4-7 b and d). Individual nanoparticles can be identified in Figure 4-7 (c). It is assumed that the ZnO nanoparticles are the crystallization nuclei that provided uniform size distribution and coating in the nanorod synthesis. SEM imaging was not possible because the ZnO films were below the resolution limit. The root mean square roughness of TF-glass was 1–3 nm.

The pure coverslips were much smoother than TF-glass. The average of an AFM scan cross section in Figure 4-8 b) shows a maximum z-range of ± 1 nm. Furthermore, the root mean square roughness of 0.3–0.4 nm was lower than that of TF-glass.
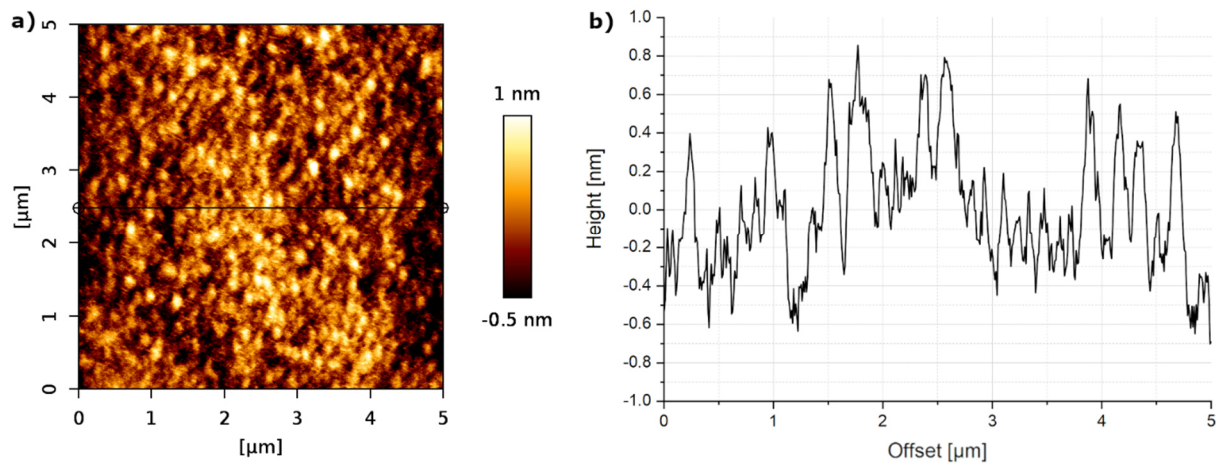
Figure 4-8: AFM image of a pure glass of a coverslip (a) and its cross section (b).
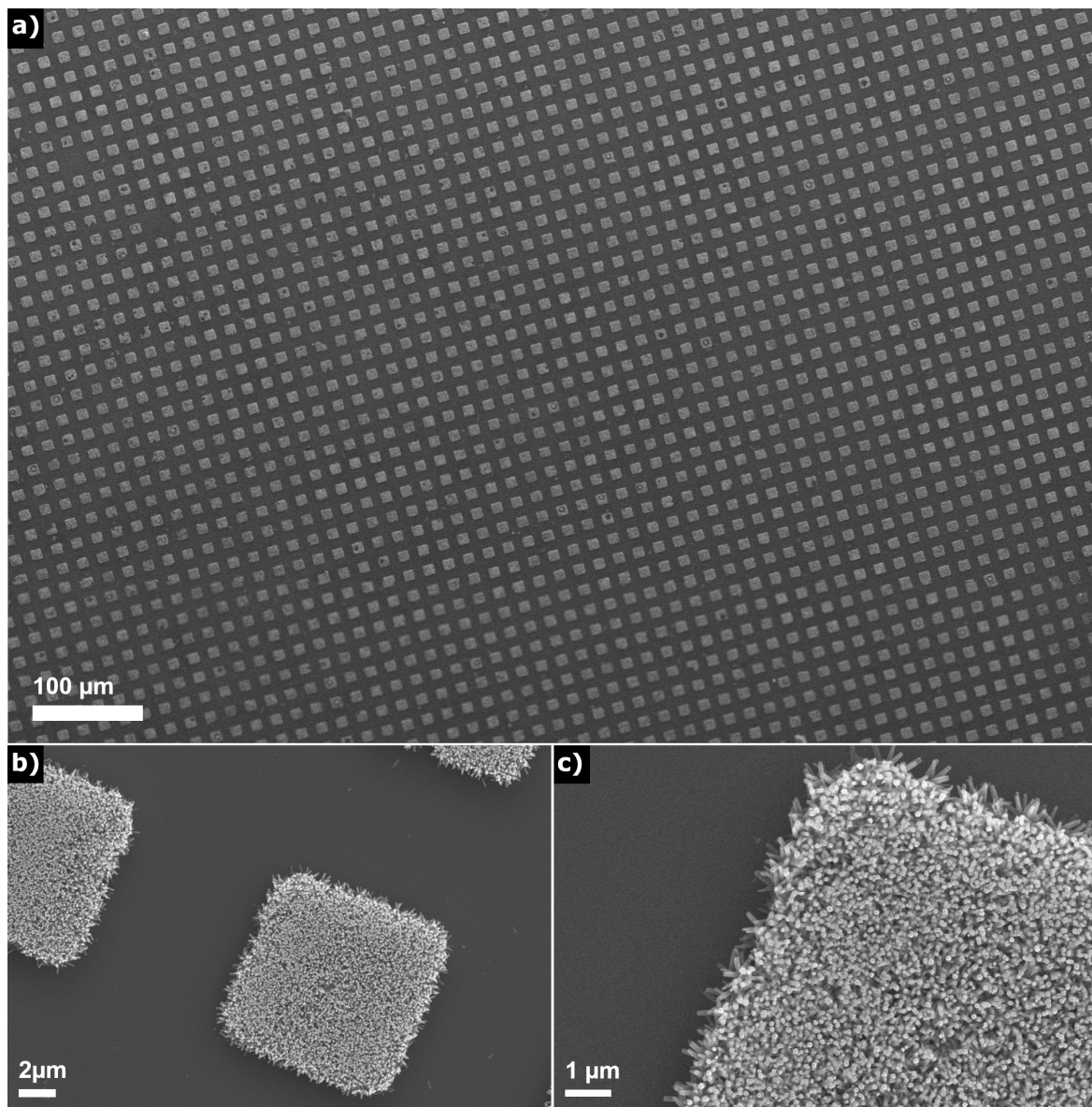
Figure 4-9: SEM images of aNR-glass for different resolutions. The device could not resolve the subsequent coated ZnO thin film.

Arrays of ZnO nanorods could be produced with a few defects in the pattern, as shown in Figure 4-9 (a). The nanorods in the nanorod regions were similar in their distribution and dimensions to those of NR-glass. In some cases, nanorods with a larger diameter appeared due to a lower seed density, resulting in a decrease in the total number of nanorods in an array. The AFM scan of Figure 4-10 shows that the nanorods on aNR-glass were approximately the same length as on the NR-glass: they were about 0.8–1.1 µm long. Furthermore, the bottom of the interspaces was almost smooth. This roughness was identical to that of TF-glass, while the roughness of the nanorod arrays was identical to that of NR-glass.
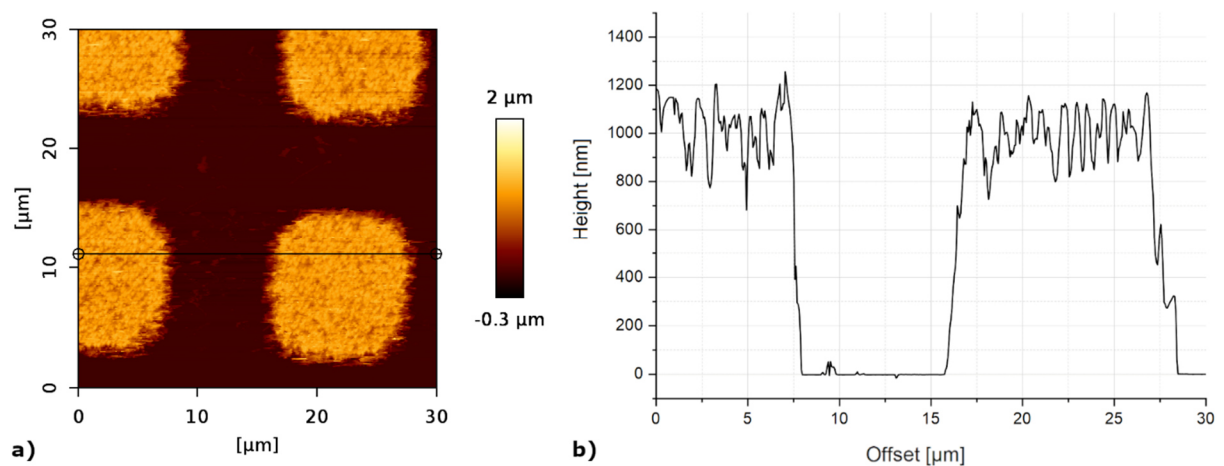
Figure 4-10: AFM image of a ZnO nanorod array (aNR-glass) on coverslip (a) and its cross section (b). The structures have been subsequently covered with a thin film of ZnO, but this cannot be discerned due to the size ratios.

4.1.3 Concentration of Dissolved Zinc During the Flow Chamber Experiment

In order to assess the influence of dissolved zinc on the bacteria, mass spectroscopic analyses were performed. The mass concentration of Zn^{2+} for the effluent from prepared channels for TF-glass and NR-glass was analyzed and are presented in Table 4-1. Both diH2O and PBS were measured, while it was assumed that ZnO had a much lower solubility in isopropanol (Agriculture and Environment Research Unit, 2023), and thus ZnO dissolution in this liquid was irrelevant. The dissolution of ZnO was about 30 to 70 times higher in flowing diH_2O compared to flowing PBS. The concentration of zinc in the aqueous solvents provides an indication of the solubility of the ZnO nanorods. A low solubility implies a higher stability of the nanorods. In addition, possible bactericidal effects of the dissolved zinc can be inferred from the concentrations. Both influences will be addressed later in the discussion.

Table 4-1: Mass concentration of dissolved zinc in the effluent of channels with ZnO surface structures on top and bottom coverslips, measured by mass spectroscopy.

	Dissolved Zn^{2+} (µg/l)	
	TF-glass	NR-glass
diH_2O	1872.58 ± 21.49	3367.30 ± 35.59
PBS	63.63 ± 1.23	47.00 ± 0.84

4.1.4 The Cell Number Distribution on Four Different Substrate Types

The attachment behavior of *P. fluorescens* SBW25 on different substrates was analyzed in situ in a flow chamber. For this purpose, images were taken with a microscope of areas on coverslips exposed to a flowing bacterial suspension. Two fluorescence image channels were used: a green channel and a violet channel. The coverslips had the homogeneous substrate types TF-glass, NR-glass, and the heterogeneous aNR-glass. In addition, the untreated coverslips were considered as pure glass. After the bacterial suspension had flowed over the substrates for 30 min, the flow channel was flushed for 7 min at an increased flow rate which induced a higher shear rate. Loosely adhering bacteria and planktonic bacteria in the liquid column were removed. Consequently, the remaining bacteria were the ones that were firmly attached to the substrate type. Subsequently, the remaining single bacteria were imaged, counted, assigned to their substrate type, and normalized to the substrate type area.

During the 30-minute attachment period, it was observed that almost all bacteria once were in contact with the substrate attached to it. Those that became detached reattached to the substrate after a few micrometers and remained there. After the cells attached, they tumbled for a while in place with the flagellum anchoring them to the surface. Finally, the cells attached firmly to the substrate with no movement anymore.
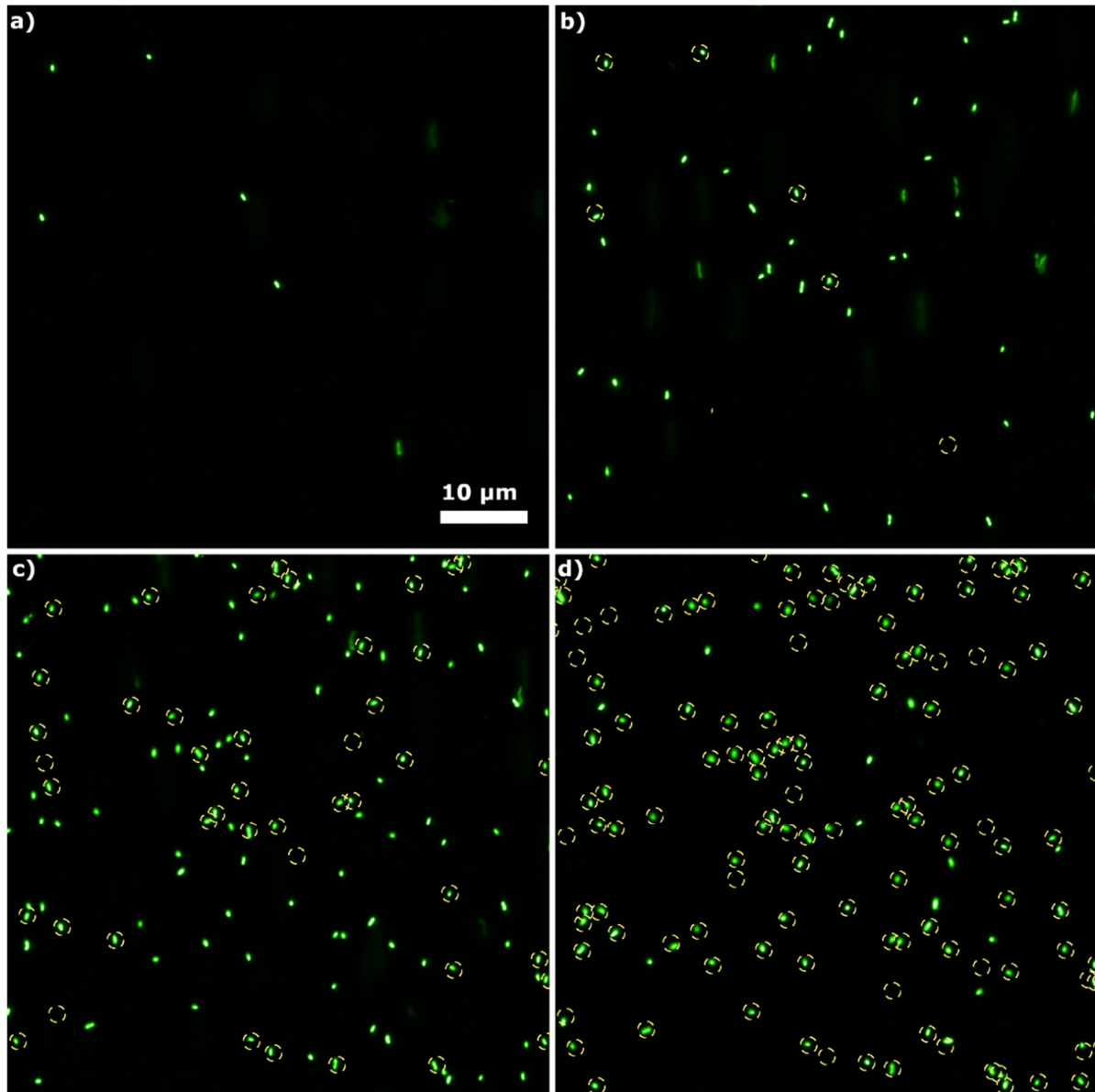
Figure 4-11: *P. fluorescens* on TF-glass captured with a fluorescence microscope (green channel), time series at the same position during the experiment. For a better visualization only an image section was chosen. The yellow round markers indicate the locations where the bacteria had attached at the previous time step. The images were captured after 5 min (with new bacteria: 7) a), after 15 min (new: 44, detached: 2, total: 49) b), after 30 min during the attachment period (new: 82, detached: 4, total: 127) c), and after purging the flow channel (new: 11, detached: 14, total: 125) d). Blurred green stripes indicate bacteria moving in the flow close to the surface.

Exemplary, a time series during the experiment at one position on TF-glass is depicted in Figure 4-11. After passing a bacterial suspension at 0.01 ml/min for 5 min through the flow channel, 7 bacteria attached. In the mid of the attachment phase (15 min), 2 bacteria had detached while 44 new bacteria had been attached. At the end of the attachment phase, 4 cells had detached compared to the previous time step, while 82 new cells had been attached. Flushing the flow channel with 0.2 ml/min removed only 14 bacteria. However, 11 cells attached since all the bacteria in the suspension from the upstream flow chamber system had to pass the selected position. Thus, the detached bacteria roughly balanced with the newly arriving bacteria.

For pure glass, the number of bacteria was determined after the attachment and flushing phase of the experiments. Figure 4-12 displays the normalized number of bacteria on pure glass for three experiments for the bottom and top coverslips, respectively. Each rDS shows points, with each indicating the number of counted bacteria in an image normalized to mm^2. The number of identified outliers was negligible. Normal distribution could not be rejected for the iaDSs and for the rDSs. A visual indication that a normal distribution of the rDSs prevailed can also be drawn from the distribution functions in Figure 4-12.

If one compares the rDSs of the technical replicates within the top and bottom coverslips, it is noticeable that the arithmetic mean number of bacteria varied. For example, the mean value for the first experiment was higher for both coverslips than for the following ones. Since these were technical replicates, which means replicates with the same substrate type, similar mean values and standard deviations would have been expected. Application of the F-test yielded F=699.5 and F=326.19 for the bottom and top glass coverslips, respectively. A post-hoc Tukey's test revealed no significant similarity between the mean cell numbers of all paired groups. Hence, the variations between the technical replicates were too strong to give one definite mean for the cell number on pure glass and one stDS was not possible to deviate.
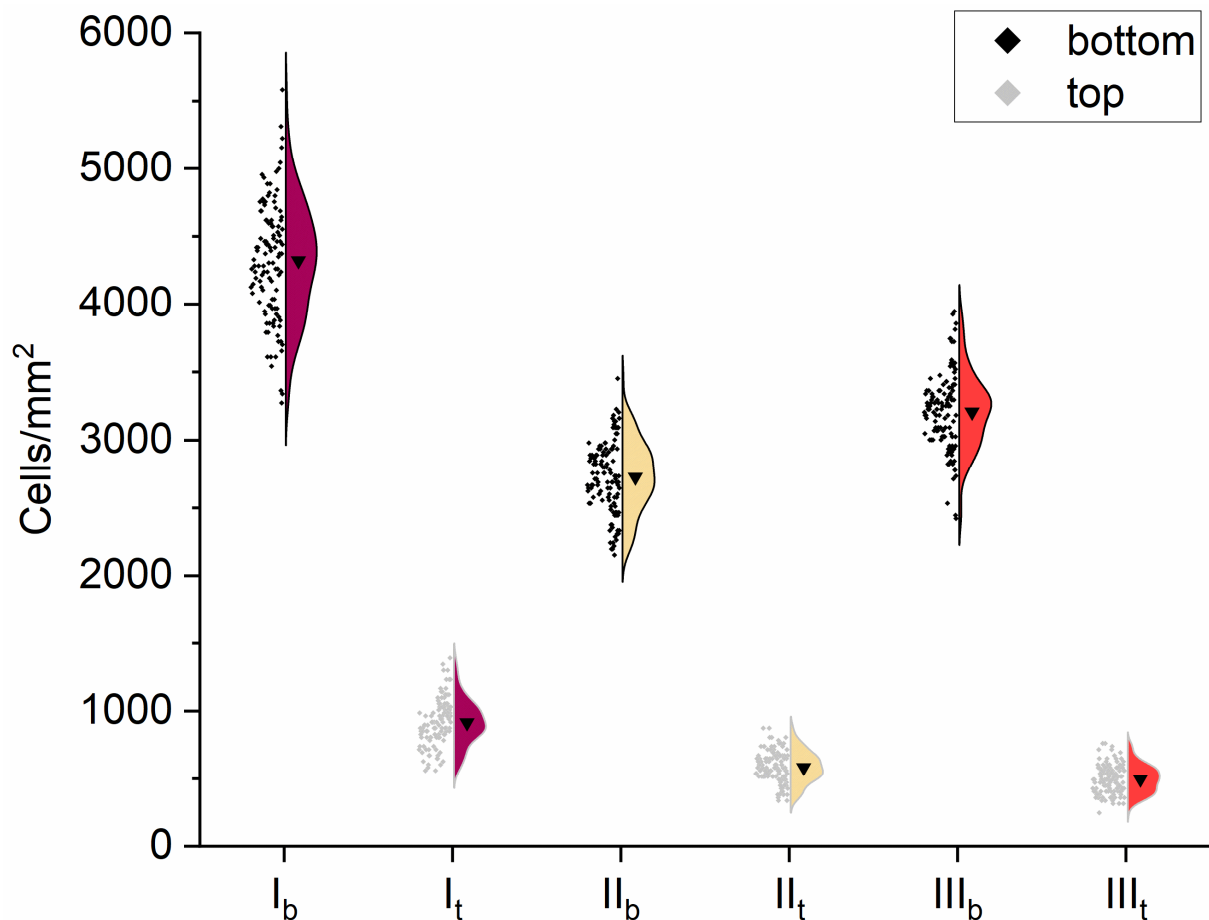
Figure 4-12: Counted bacteria cells normalized to mm^2 on pure glass for three experiments (I – III) and for bottom (subscript b) and top coverslip (subscript t). On the left side of each rDS, the normalized cell count for each image is shown as a point, and on the right side is the distribution function. ▼ = arithmetic mean.

The cell numbers on the bottom and top coverslip after attachment and flushing for three technical replicates of TF-glass are plotted in Figure 4-13. The normal distribution for the bottom coverslips was not rejected for any iaDS. For the rDSs, the normal distribution was rejected for I_t, III_t, and III_b. This outcome was reflected in the probability distributions of the rDSs, which had no Gaussian curves but were bimodal. The bacteria appeared to attach non-uniformly to different areas within the same replicate. For the comparison between the rDSs, ANOVA (DF=2) revealed for the bottom and top TF-glass F=544.37 and F=15.38, respectively. Tukey's test indicated that the null hypothesis must be rejected for all pairwise group comparisons except I_t and III_t as well as I_b and II_b. Thus, also for TF-glass, no stDS could be derived.
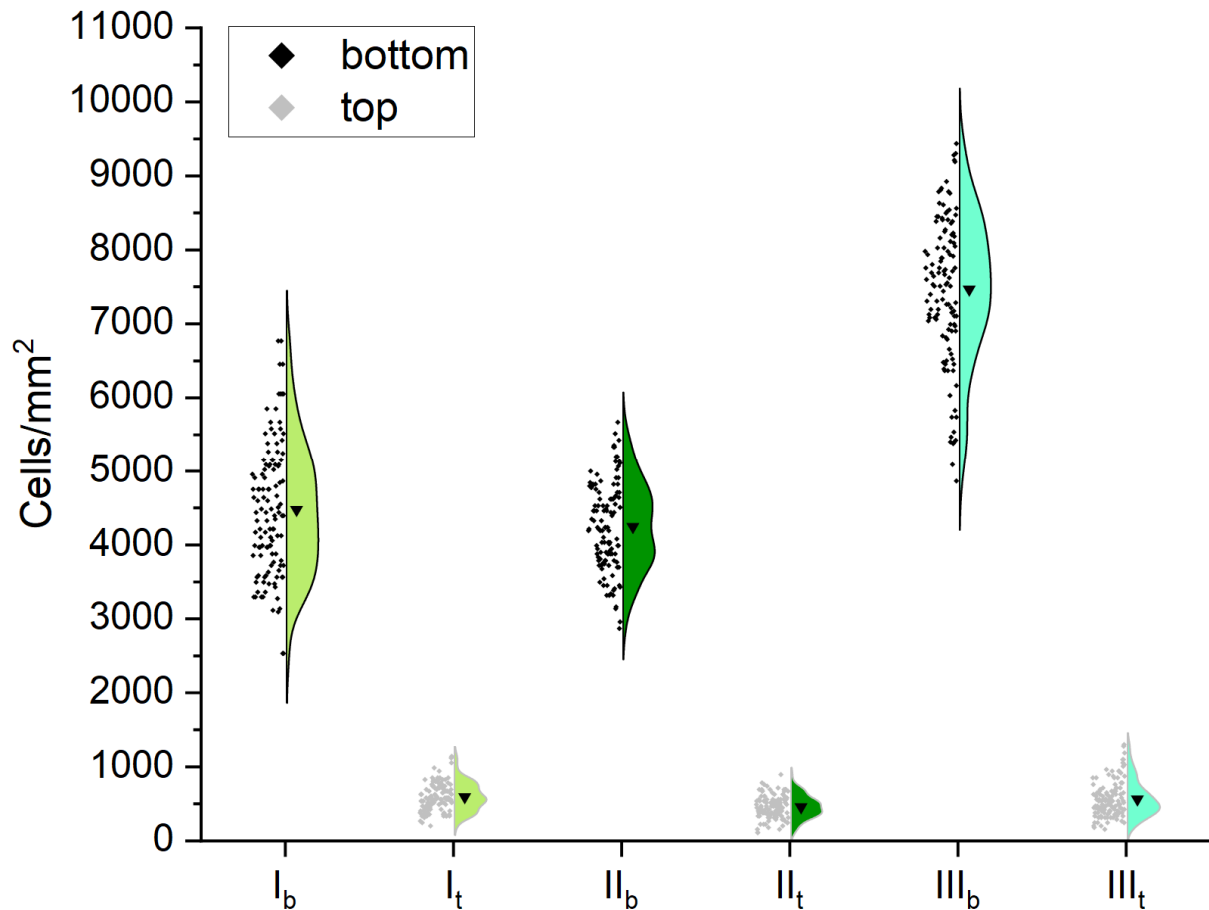
Figure 4-13: Counted bacteria cells normalized to mm^2 on TF-glass for three experiments (I – III) and for the bottom (subscript b) and top coverslip (subscript t). On the left side of each rDSt, the normalized cell count for each image is shown as a point, and on the right side is the distribution function. ▼ = arithmetic mean.

Figure 4-14 shows the normalized cell number for NR-glass. One iaDS of the replicate III$_t$ had no normal distribution. For the entire rDSs II$_t$ and III$_t$, as well as for III$_b$, no normal distribution was found. As was observed for TF-glass, bimodal distributions were noticeable from the plots. ANOVA F-test (DF=2) resulted, with the data set of experiments I – III, in F=257.01 and F=310.45 for the bottom and top NR-glass, respectively. The null hypothesis had to be generally rejected for all data set pairwise combinations as identified by Tukey's test. Again, no stDS could be derived for NR-glass.
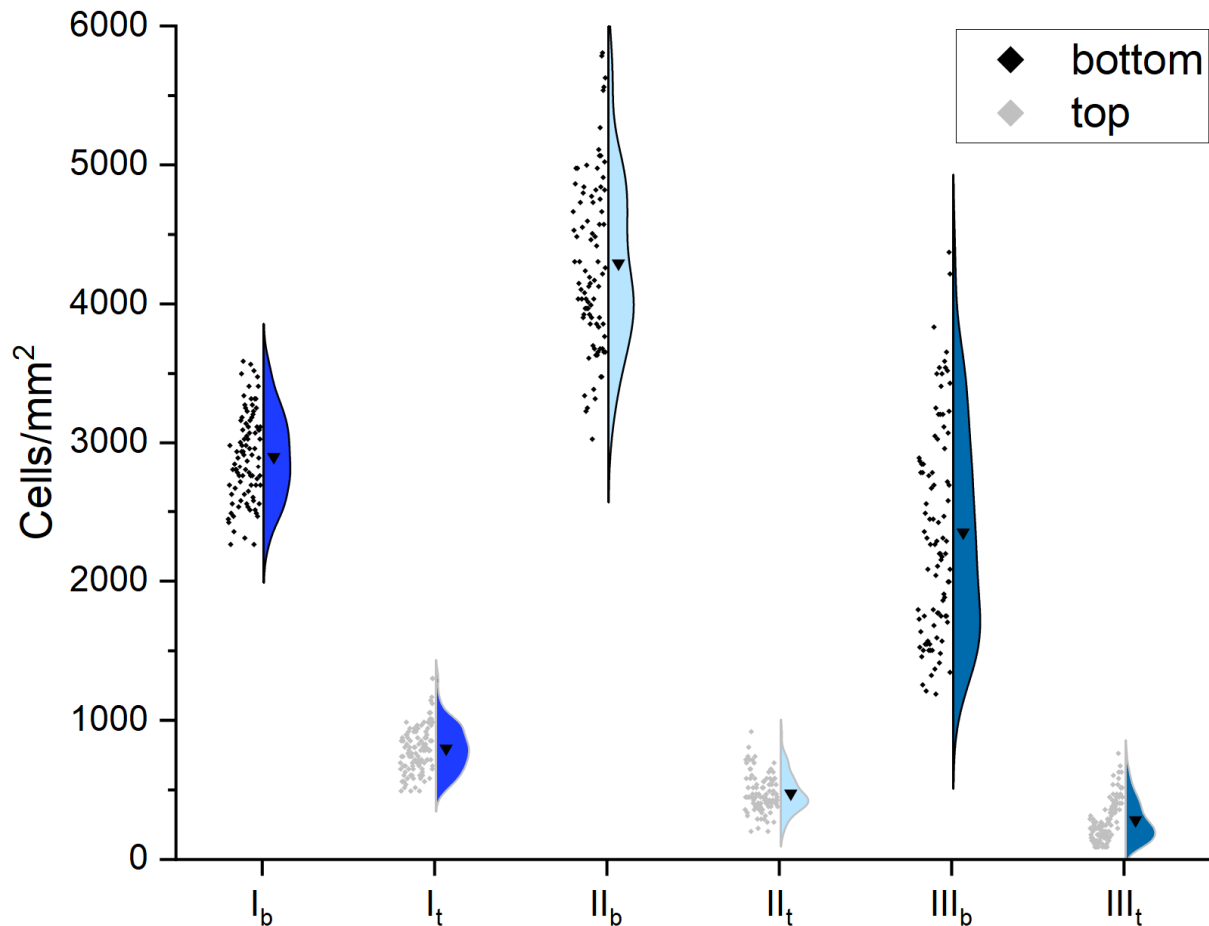
Figure 4-14: Counted bacteria cells normalized to mm^2 on NR-glass for three experiments (I – III) and for the bottom (subscript b) and top coverslip (subscript t). The normalized cell count for each image is shown as a point on the left side of each data set, and on the right side is the distribution function. The triangle shows the arithmetic mean. ▼ = arithmetic mean.

The arithmetic mean normalized cell number of each homogeneous substrate type is presented in Table 4-2. The values for pure glass varied around 500 to 900 cells/mm² and around 2700 to 4300 cells/mm² for the top and bottom coverslip, respectively. The cell numbers for TF-glass varied around 450 to 600 cells/mm² and around 4200 to 7500 cells/mm² for the top and bottom coverslip, respectively. The values for NR-glass varied around 300 to 800 cells/mm² and around 2400 to 4300 cells/mm² for the top and bottom coverslip, respectively.

From the arithmetic means and standard deviations, it can be concluded that there was a high degree of variation within the data sets, as is the case for III$_t$, for example (relative error of about 50%). Furthermore, the mean values of the replicates of a substrate type fluctuate. For the bottom coverslips of TF-glass, for example, the values differ by about 40%. This observation confirmed what had already been found by the statistical tests of the entire data sets: the replicates did not resemble each other. Furthermore, comparing the mean values of one substrate type with the mean values of another

substrate type, no one stood out. Comparing within the top and the bottom coverslips, no substrate type was found to have an increased or reduced bacterial number.

The adsorption rate coefficient j, which was calculated from the arithmetic mean values, is given in Table 4-2 to compare the attachment of the bacteria in the present study with literature data. For pure glass, which is often investigated, values in the range of $0.22 \cdot 10^{-8}$ to $0.4 \cdot 10^{-8}$ m/s and $1.18 \cdot 10^{-8}$ to $1.88 \cdot 10^{-8}$ m/s were calculated for the top and bottom coverslip, respectively.

Table 4-2: Mean normalized attached cell number with standard error on different substrate types (given are values for the rDSs) and the derived adsorption rate coefficient according to equation (2).

		Mean cell number per mm^2			Adsorption rate coefficient 10^{-8} m/s		
		I	II	III	I	II	III
Pure glass	Top	916 ± 170	583 ± 118	496 ± 106	0.4	0.25	0.22
	Bottom	4320 ± 434	2727 ± 265	3207 ± 283	1.88	1.18	1.39
TF-glass	Top	593 ± 188	458 ± 154	564 ± 238	0.26	0.2	0.25
	Bottom	4475 ± 887	4247 ± 597	7466 ± 990	1.94	1.84	3.24
NR-glass	Top	799 ± 171	475 ± 136	284 ± 151	0.35	0.2	0.12
	Bottom	2899 ± 318	4292 ± 616	2350 ± 756	1.26	1.86	1.02

The apparent inhomogeneities of the bacteria distribution on the same substrate, as reflected by non-Gaussian distribution curves, were investigated in more detail for TF-glass. For this purpose, the almost entire flow channel cross section, approximately 4 mm, of the bottom and top coverslip surface was examined over a length of 8 mm. Figure 4-15 shows the attached bacterial cells/mm^2 over this examination zone. For both the top and bottom coverslips, regions of different bacterial densities can be distinguished. The differences in cell number distribution were more significant in the y-direction than in the x-direction. This distribution led to elongated shapes of similar bacterial densities parallel to the flow direction. Since the x-direction was the flow direction, it is reasonable to assume that distinct flow characteristics occurred parallel to the flow.

The attachment behavior of bacteria on a combination of smooth areas and nanorough areas on the same substrate was investigated using aNR-glass. The areas with nanorods could be distinguished from those with thin films in the microscope by means of the NBE emission of ZnO nanorods displayed by the violet channel. In the grayscale image, the nanorod areas appeared brighter. A border region was

introduced for the evaluation. It was defined as ± half a bacterial length (0.5 µm) originating from the sharp thin film–nanorod transition. This approach was necessary because bacteria could not be unambiguously assigned to a substrate type due to their two-dimensional attachment on the thin film–nanorod transition. Besides this reason, the roughness change caused by the transition from thin film to nanorods should have also been taken into account. Depending on where the maxima were located, they were assigned to one of the three substrate types.
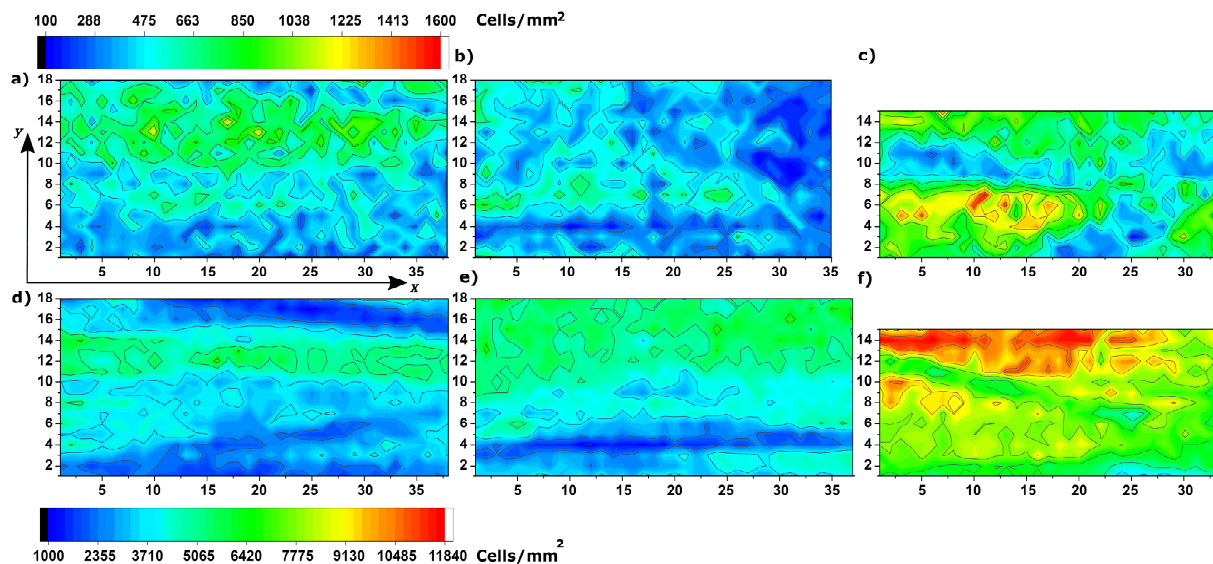
Figure 4-15: Bacterial cells/mm^2 on three replicates of TF-glass, top (a-c) and bottom coverslips (d-f). Ordinate and abscissa indicate the image number in row and column, respectively. The sections have dimensions of approximately 4x8 mm^2. The technical replicates I – III are (a, c), (b, e), and (c, f), respectively. The flow direction is parallel to the x-axis.

Each image comprised three different substrate types: about 70% interspace region, 20% nanorods region and, 10% border region. Therefore, the different substrate types' sizes influenced the probability of bacterial attachment. This influence could be excluded by normalizing the counted bacteria to their individual substrate. For this purpose, the number of counted bacteria was divided by the area of the substrate type they were located on. This procedure was performed for each image individually. The normalized cell count was determined for four experiments (I – IV) for the bottom and top coverslips.

The normalized cell count varied on the bottom coverslips varied for each aNR-glass substrate type as can be seen in Figure 4-16. It should be noted that per replicate, three rDSs resulted due to the three substrate types. For all replicates, arithmetic means were lowest for the interspaces. In contrast, the means for the border regions were the highest. The means for the nanorod substrate type were in between. An exception was the rDS of IV. Here the mean cell count on nanorods was at the level of

the mean cell count on interspace. Whether the means of the rDSs "bacteria in interspaces", "on borders", and "on NRs" were similar was tested with ANOVA (DF=3). The F-test for the bottom aNR-glass resulted in F=384.03, F=51.07, and F=96.75 for the bacteria in the interspaces, on borders and on nanorods, respectively. Significantly equal according to a post-hoc Turkey's test were only pairwise combinations of I_{border}, II_{border}, and III_{border} as well as the combination III_{NR} IV_{NR}. The large deviations between replicates occurred for bottom aNR-glass as they did for the homogeneous substrates. Possibly, these variations were due to the same influences. Nevertheless, the following statement holds: bacteria, under the influence of gravity, most likely gather on aNR-glass at the border regions, followed by the regions on the nanorods, and finally the interspaces.
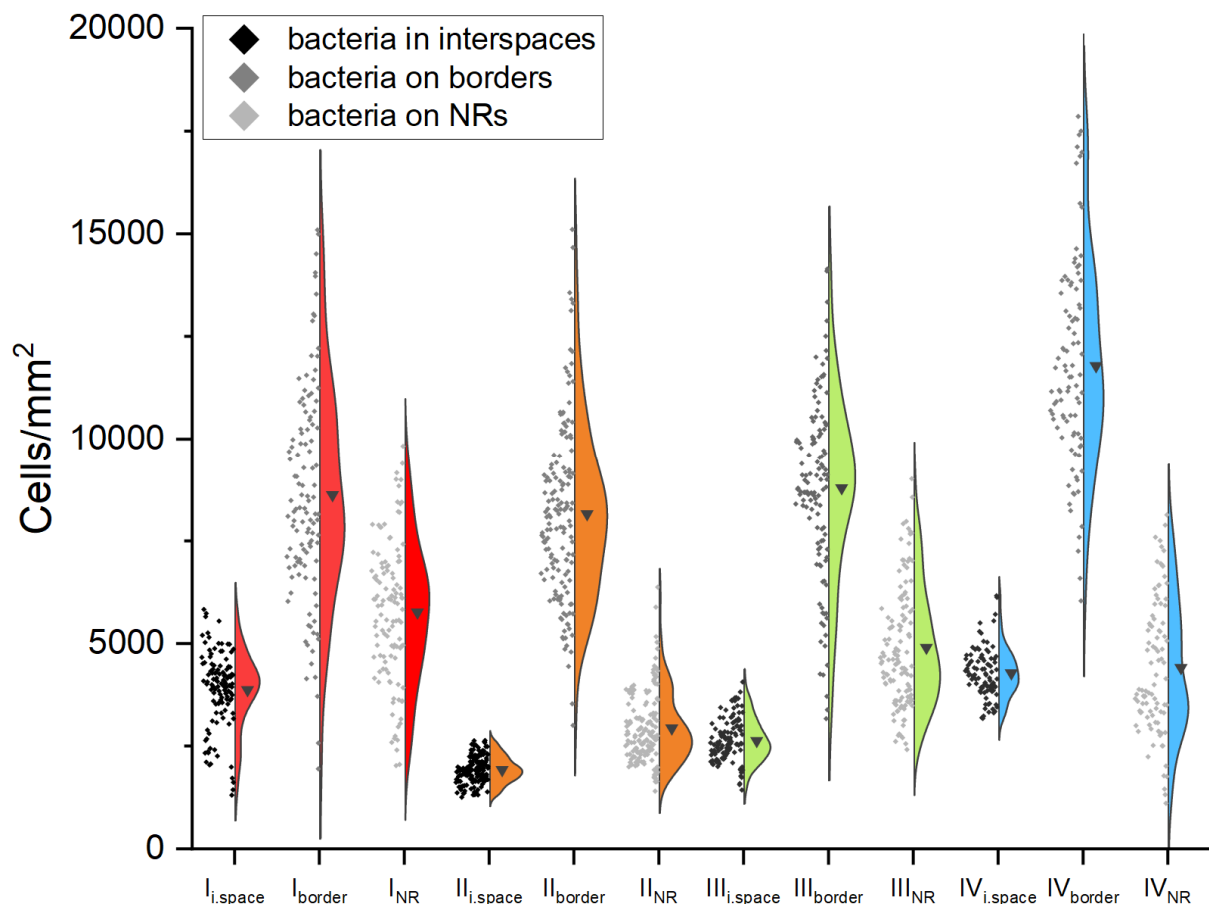
Figure 4-16: Normalized number of bacterial cells per mm^2 for the four experiments (I – IV) for the bottom coverslips. The data points are shown on the left, and the distribution function is on the right. One data point corresponds to the normalized number of cells on a substrate type in one evaluated image. The arithmetic mean is symbolized by a black triangle. All rDSs of a technical replicate are colored in the same way. ▼ = arithmetic mean.

The rDS for the top coverslips resembles the rDS for the previously discussed bottom coverslips as can be seen in Figure 4-17. The lowest arithmetic means were determined for bacteria that attached in the interspaces. The means for the border regions were highest, while that for the nanorod substrates was

slightly lower. However, both means were distinctly higher than that for the interspaces. An exception was replicate II. The ANOVA(DF=3) F-test yielded F=62.67, F=17.5, and F=71.53 for the bacteria in the interspaces, on borders, and on nanorods, respectively. Only the pairwise combinations of the groups $II_{i.space}$ and $IV_{i.space}$, I_{border} and III_{border}, as well as I_{NR} and III_{NR}, I_{NR} and IV_{NR} were significantly equal as calculated with post-hoc Turkey's test. The low similarity in cell number distribution on each substrate type between the replicates was noticeable for the top coverslips as it was for the bottom coverslip of aNR-glass. As with the bottom coverslips of aNR, bacteria most likely attached at the border regions, followed by the nanorods and the interspaces. However, the difference between the border regions and the nanorods was much less pronounced without the influence of gravity.
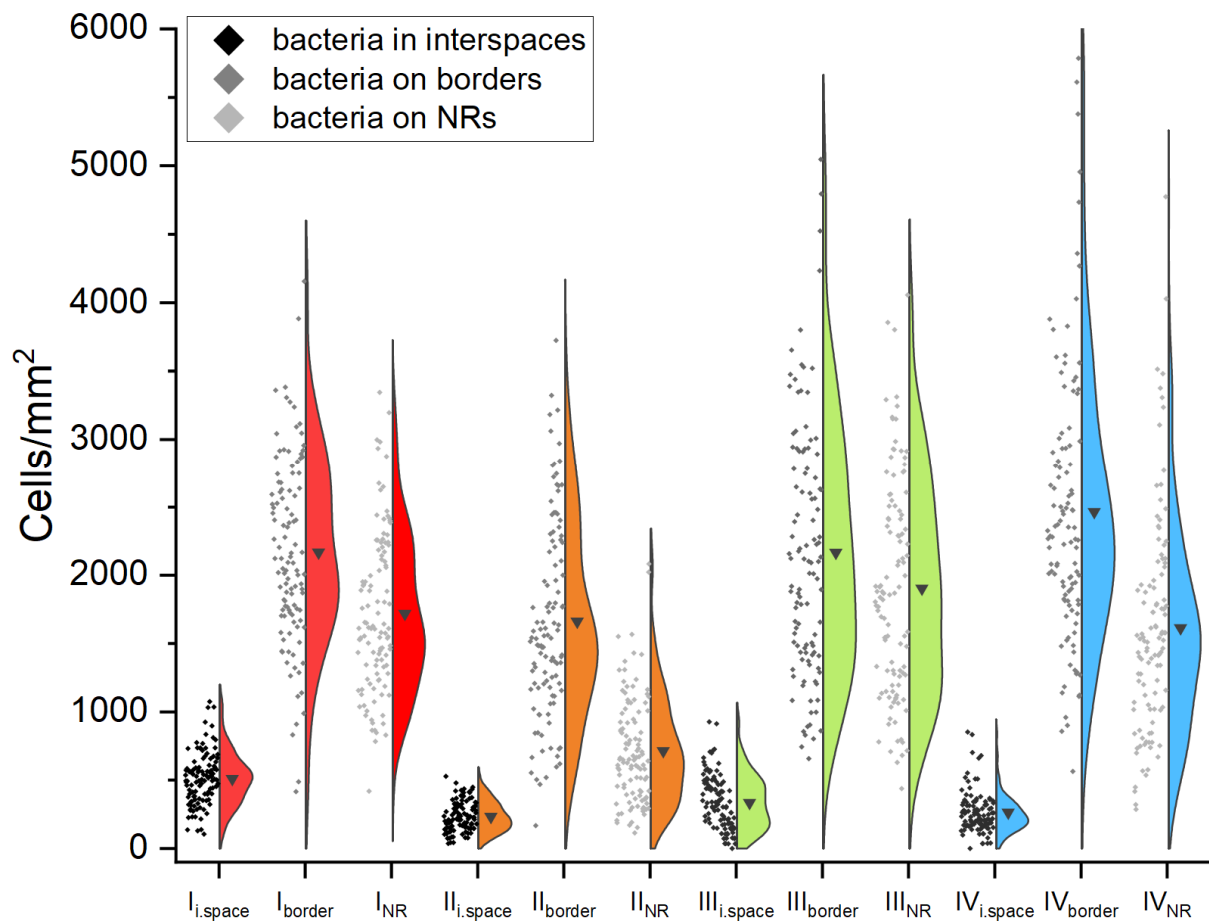
Figure 4-17: Normalized number of bacterial cells per mm^2 for four experiments (I – IV) for the top coverslips. The data points are shown on the left, and the distribution function is on the right. One data point corresponds to the normalized number of cells on a substrate type in one evaluated image. The arithmetic mean is symbolized by a black triangle. All rDS of a technical replicate are colored in the same way. ▼ = arithmetic mean

In the following, the total normalized bacterial number on aNR-glass was considered. This number was the sum of all bacteria in an image related to the image dimension (211x211 µm^2). The arithmetic mean

with standard error, as well as the adsorption rate coefficient of the rDSs of aNR-glass, are given in Table 4-3. The values for the top coverslips varied between approximately 550 and 1000 cells/mm^2 and for the bottom coverslips between approximately 2800 and 5000 cells/mm^2. The large variation in the mean values and the large standard errors were probably due to inhomogeneous flow fields in the channel, as was the case for the homogeneous substrates. Compared with the bacterial numbers of the homogeneous substrates, the values do not indicate an effect on bacterial attachment: for both the top and bottom coverslips, the mean values for aNR-glass were in the same range as for pure glass, TF-glass, and NR-glass. Thus, an overall effect of microtopography on the attachment and retention behavior of *P. fluorescens* was not observed.

Table 4-3: Mean normalized attached cell number with standard error on aNR-glass (given are values for the rDSs) and the derived adsorption rate coefficient according to equation (2).

		Mean total cell number per mm^2				Adsorption rate coefficient 10^{-8} m/s			
		I	II	III	IV	I	II	III	IV
aNR-	Top	986 ± 224	560 ± 179	919 ± 314	852 ± 314	0.43	0.24	0.4	0.37
glass	Bottom	4663 ± 1099	2825 ± 404	3632 ± 628	4999 ± 695	2.02	1.23	1.58	2.17

4.1.5 Discussion

Bacterial attachment experiments in a flow chamber were performed with ZnO surface nanostructures. Since ZnO can release Zn^{2+} in an aqueous solution which can be toxic for bacteria, the stability of the ZnO structures during the experiments had to be evaluated.

ZnO dissolved much more strongly in diH$_2$O than in PBS. This observation is in agreement with the results of Kääriäinen et al. (2013). They studied the solubility of atomic layer deposited ZnO thin films, but under static conditions. They also found a lower solubility for ZnO in PBS than H$_2$O. After 24 h, they measured a zinc ion concentration of about 1 mg/l in PBS and about 7 to 12 mg/l in H$_2$O, respectively. After 5 days, the ZnO film had reduced by 4 nm in H$_2$O and 0.25 nm in PBS, respectively. The reason for the lower solubility of PBS was the formation of Zn$_3$(PO$_4$)$_3$, which is poorly soluble and could not be measured in the supernatant. Similar results were observed by Meißner, Oelschlägel and Potthoff (2014). They also attributed the lower measured Zn^{2+} concentration to the formation of zinc phosphate.

From the low value of Zn^{2+} in PBS (≈ 55 µg/l) in the experiment, a high stability of the ZnO nano- and microstructured surfaces cannot be inferred because Zn^{2+} can precipitate as zinc phosphate. This

reaction probably occurred in the experiments in this study. However, SEM analysis of ZnO substrates before and after the experiments showed no difference. Thus, for the duration of the experiments, the conversion of the ZnO nano and microstructures to zinc phosphate precipitates can be excluded as an experimental influence. However, the ZnO substrates are not suitable for long-term experiments and a protection of the structures must be considered for these applications.

The bactericidal effect of zinc on *P. fluorescens* has already been studied (van Beelen and Fleuren-Kemilä, 1997; Upadhyay and Srivastava, 2014; Lei et al., 2020). Lei et al. (2020) found the lowest minimum inhibitory concentration of zinc sulfate for different strains studied to be 0.4 mmol which corresponds to 0.0256 g/l Zn^{2+}. Upadhyay and Srivastava (2014) found no Zn^{2+} accumulation in *P. fluorescens* cells up to 1 mmol/l. McEldowney (1994) studied the influence of dissolved zinc on the attachment behavior of a *P. fluorescens* strain, with the lowest concentration studied of 5 mg/l. The author found a slight effect, mainly due to the influence on cell surface physicochemical characteristics, similar to what other divalent cations caused. In this study, the concentration of dissolved zinc in diH_2O was measured to compare with the results of other studies. The highest value measured for the effluent from a channel with NR-glass was 3.37 mg/l. This concentration was lower than the reported literature values. Furthermore, no diH_2O was used in the experiments, but PBS. For this medium, the concentration of dissolved zinc (≈ 55 µg/l) was far below the value of diH_2O. Although no values are known for the influence of zinc in PBS on bacteria, it can be assumed that the low concentration did not have a biocidal effect *P. fluorescens*. An influence of zinc ions on the attachment behavior of the cells was suggested as unlikely. However, as the chemical composition of the nano- and microstructured ZnO surfaces were identical, an influencing effect of Zn^{2+} and zinc oxide on the attachment of *P. fluorescens* was considered equivalent.

The initial attachment behavior of *P. fluorescens* SBW25 and the bacterial retention on nanorough surfaces with and without a microstructure was studied using a flow chamber. In the following, comparisons will only be made with other studies using flow chambers as well. The specific design of the flow chamber used in the present study allowed the use of a high numerical apparatus objective of a fluorescence microscope. Thereby, individual bacteria could be identified and imaged. Microstructured substrates with arrays of nanorods could be identified using NBE emission from ZnO. Multiple images in randomly selected regions on the substrate ensured statistical evidence. Evaluation of bacterial cell number, as well as correlation within the microstructured substrate, was done using an ImageJ macro script.

The data sets must first be evaluated before answering the question of whether the nano- or microtopography being studied will result in reduced bacterial attachment and retention. Afterwards, the cell numbers on the substrates can be checked for significant differences. These differences may

indicate an influence of the substrate. In the following, the data basis, as reflected by the data sets will be discussed.

Significant differences can be determined with a hypothesis test, such as the ANOVA. However, an ANOVA at the level of substrate types was not applicable since the needed stDSs of all attaching bacteria for each substrate type could not be derived. In such overall distribution, all rDSs must be reflected. If it is assumed that the conditions between the repetitions were the same, the resulting rDSs must have also had a significant similarity among each other. However, among the rDSs of one substrate type, no significant similarity was found with the ANOVAs. This finding applied to glass, TF-glass, and NR-glass, as well as top and bottom surfaces. The situation for aNR-glass will be discussed later. Furthermore, neither a consistent picture emerged when the mean values and standard errors of the rDSs were compared, nor differences between rDSs could be identified for the substrate types (see Table 4-2). Therefore, an influence of the topography in the range of a few to a hundred nanometers on the bacterial attachment was not observable.

For some rDSs, normal distribution of the bacterial cell numbers was not applicable since subclusters of values occurred and resulted in bimodality, for example. Such subclusters appeared in the rDSs if areas were imaged in regions of different cell densities. A closer look at TF-glass experiments revealed that the bacteria were not uniformly distributed over the homogeneous surface. Elongated shaped areas with high or low cell numbers were observed parallel to the flow direction. The reasons for such variations can be surface properties, flow conditions (Margalit, Leshansky and Freger, 2013), and bacterial density in the bulk flow over the structures (McClaine and Ford, 2002). The first could be excluded since the homogeneity of the substrates was confirmed by SEM and AFM. Moreover, the areas' shape of different attachment densities suggested flow-related phenomena. In the near field, these flow phenomena were not noticeable. Therefore, the iaDS, which only covered a small area, generally had a normal distribution. Whether a normal distribution was also reflected in the rDS, as was the case for pure glass, depended on the randomly selected image areas. Suppose these flow phenomena are considered in light of the large fluctuations within the rDS. In that case, it can be concluded that the effect of the nanotopography on bacterial attachment and retention was probably masked. As was observed, the flow conditions varied greatly and thus likely had a greater influence on bacterial attachment than the ZnO nano- and microstructures.

CFD simulation of the flow chamber revealed that the same flows with the same characteristics, such as shear stress, velocity, and orientation prevailed on the entire bottom and top channel walls. Accordingly, the flow characteristics for bacterial attachment were the same everywhere. This contradiction between CFD simulations and observations has not been reported in the literature so far. However, studies exist that report high variations and standard errors of bacterial attachment

(Scheuerman, Camper and Hamilton, 1998; Ling, Graham and Cady, 2012). Furthermore, Valiei et al. (2012) designed a channel with flow-splitting elements which led to an equalization of the pressure in the observed channel section. This experimental design could indicate that flow phenomena have already been noticed and some solutions were considered. It is possible that interactions exist between the fluid and the material of the surface, which lead to the formation of zones with increased flow velocities. These were not considered in models for CFD, so further studies are necessary.

Nevertheless, for all substrate types, a general pronouncing trend in the data was observed, which was the number of bacteria was higher on the bottom surface than on the top surface. The cause is discussed in the following with references to observations in the literature. A first suggestion might be that such a characteristic would be gravitationally determined. However, contrary results to this assumption have been reported. Rutter and Leech (1980) found no sedimentation due to gravitational forces. *Streptococcus sanguis* attached equally to both the top and bottom of a microslide. Thereupon, Sjollema, Busscher and Weerkamp (1988) pointed out that sedimentation effects not only correlate with the mass of the particles relative to the suspending medium but also depend significantly on hydrodynamic conditions. Especially in systems with a low ratio of convective to diffusive mass transport, sedimentation effects are important. In their experiments, they found a decreased deposition rate at the top compared to the bottom plate of a flow chamber for different Streptococci strains. In fact, the hydrodynamic factors are far more complex. Margalit, Leshansky and Freger (2013) modeled the deposition by including adhesion, buoyancy, and lift forces as well as flow velocity and diffusion. According to their model *P. fluorescens*, with an averaged radius of 0.75 µm (Ping, Birkenbeil and Monajembashi, 2013) would unambiguously attach more to the bottom wall than to the top wall, which is consistent with the observations of the present study.

In the following, the result will be discussed that the investigated nano- and microtopographies had no observable effect on the attachment and capability of the bacteria to withstand high shear stresses. Furthermore, possible reasons for this outcome are suggested.

The attachment of *P. fluorescens* to glass was studied by Camper et al. (1993). They estimated the adsorption rate coefficient j to be $6.5 \cdot 10^{-8}$ m/s for the bottom coverslip. A similar value was found by Mueller et al. (1992) with $6.9 \cdot 10^{-8}$ m/s. The higher attachment compared to the present study ($1.18 \cdot 10^{-8}$ to $1.88 \cdot 10^{-8}$ m/s) can be explained by a higher shear rate. In both referred studies, it was 784 s^{-1}, while in the present study, it was 18 s^{-1}. An increased shear rate correlates with a higher flow, which provides more bacteria per time in the flow channel cross section, thus causing more bacteria to attach (Margalit, Leshansky and Freger, 2013). This relation holds for a shear rate threshold at which an increase in shear rate reduces the attachment of bacteria. At this threshold, the detaching forces of shear stress prevail. For comparison, Busscher and van der Mei (2006) indicated that shear rates of

6000 to 8000 s^{-1} on the wall were necessary to prevent attachment of *P. fluorescens* to stainless steel. Only at 12000 s^{-1} did the cells detach (the maximal detachment shear rate in the present study was 356 s^{-1} at 0.2 ml/min flow rate). Such high wall shear stresses were not present in either the attachment phase or the flushing phase in the experiment of this study.

A comparison of this study's result on the attachment and retention of bacteria on nanostructured surfaces (NR-glass) is provided by the studies of Hizal et al. (2016) and Hizal et al. (2015). In the first reference, the authors investigated a surface with single nanopillars of 500 nm height with different spacings and tip diameters (Hizal et al., 2016). No differences in adsorption rates between the nanostructured surfaces and a smooth control were observed. For all surfaces, *j* was ca. 7.5 $\cdot 10^{-8}$ m/s for *S. aureus* and 5.5 $\cdot 10^{-8}$ m/s for *S. epidermidis.* However, the detachment was higher for bacteria on the nanopillars than on the smooth control. This behavior was measured with higher shear rates as it was done in this study. The nanotopography of the second study (Hizal et al., 2015) is more comparable to that of this study, as both involved a nanostructure-"lawn", meaning no spacing between structures. Likewise, the authors found no difference in the attachment of *S. aureus* to a smooth and nanostructured surface. In summary, this studies confirms the observations of this work that there is no difference in bacterial attachment to smooth and nanostructured surfaces.

The higher adsorption rate coefficient of staphylococci of the above-cited study compared *to P. fluorescens* in this study (1.18 $\cdot 10^{-8}$ to 1.88 $\cdot 10^{-8}$ m/s) might be attributed to the drag of bacteria. Cells from the upper channel areas detach and reattach further down in the observation window. That is the case when bacteria do not attach in sufficient strength to the substrate, detaches and reattaches later (Li et al., 2011; Margalit, Leshansky and Freger, 2013). Negligible detachment was observed for *P. fluorescens* in the present study in time series images. In contrast to *S. epidermidis* and *S. aureus, P. fluorescens* has flagella presumably providing the bacteria's strong linkage to the substrate with initial adhesion and protecting quite efficiently from detachment. The flagella acted here like a kind of anchor. That was evident from the temporary tumbling movements of bacteria newly attached and has already been observed by Conrad et al. (2011) and Sharma and Conrad (2014).

A comparison of this study's result on the attachment and retention of bacteria to ZnO nanopillars is provided by the study of (Lin et al., 2022). Two types of ZnO nanopillars were prepared, one with high surface density and low void area and the other with low surface density and high void area. In addition, a ZnO thin film was considered as smooth reference. Both the ZnO nanopillars with high density and the ZnO thin film resembled the NR-glass and TF-glass of the present study, respectively. At a wall shear stress of 8.6 mN/m^2 (17 mN/m^2 in the present study), all bacterial species (*P. aeruginosa*, *S. aureus* and *B. subtilis*) attached equally regardless of the different topographies. Only increased wall shear stresses of 43, 86, and 430 mN/m^2 increasingly detached the bacteria from low

density and high density ZnO nanopillars and smooth ZnO. However, all bacterial species detached least from the low-density ZnO nanopillars. The authors concluded that bacteria were trapped in the large void areas of the low-density ZnO nanopillars and were protected from detaching shear stress. Thus, the detachment of bacteria by higher wall shear stresses would actually contradict the present study. However, the observed initial attachment time was only 3 min (Lin et al., 2022) while it was 30 min in the present study. The authors performed an additional experiment and noted that *P. aeruginosa* could not be detached from increased shear stress after 90 min attachment time. That would mean that after 30 min attachment time in the present study, *P. fluorescens* cells were in transition to the firmly attached stage.

Assuming that attached bacteria after only a few minutes were already irreversible fixated, it must be assumed that bond-maturing has already happened. This in consequence would mean an adhesion force of the bacteria of 0.5-1 nN (Busscher et al., 2010; Aguayo et al., 2015). In contrast, a lateral force of $6.6 \cdot 10^{-15}$ nN and $1.3 \cdot 10^{-13}$ nN for a flow rate of 0.01 ml/min and 0.2 ml/min acts on the single attached bacterium, respectively. Here, it is assumed that the bacterium is longitudinal-orientated and has a diameter of 0.7 µm. This discrepancy illustrates that a bacterium can no longer be detached by shear stress after a few minutes. At this point, it should be noted that moving air-liquid phase boundaries can cause lift forces up to 200 nN acting on one bacterial (Gomez-Suarez, Busscher and van der Mei, 2001). Thus, ex-situ analysis of bacteria that can not withstand such high forces is prone to biases.

Attachment of *P. fluorescens* to aNR-glass was quantified by absolute cell numbers on the substrate types and by normalized cell numbers. It became obvious that these two presentations showed different pictures of bacterial attachment on a heterogeneous surface. The probability of attachment for the cells was proportional to the available area of the substrate types. Therefore, a normalized bacterial count, where the number is related to the area, more closely reflects reality. However, variations of the rDSs were apparent for aNR-glass, as was the case for the homogeneous substrate types. This anomaly was probably caused by the same above-described flow phenomena: A non-homogeneous flow field caused a non-uniform distribution of bacteria in the channel. However, for aNR-glass, it must be noted that all substrate types can be found in each image. Thus, in addition to the flow field in the bulk stream, the near field at the surface gained more influence. That means all substrate types were offered for attachment to the single, passing bacterium several times on its trajectory. Hence, the relative distribution of the bacteria in the nanorod, interspace, and border regions was a consequence of the near field. From this distribution, some conclusions can be drawn on the bacterial attachment behavior of the substrate types.

P. fluorescens cells attached more to the border regions and the raised nanostructures of aNR-glass than to the deeper smooth surface of the interspaces. When comparing nanorods and border region, the latter was in favor of bacterial attachment. This distribution was more pronounced for the bottom substrates than for the top ones. Moreover, the cell number in the border region was distinctly higher than for all homogeneous substrate types studied.

A reason for this observation can be found in the study of Scheuerman, Camper and Hamilton (1998), who investigated the attachment of a motile and non-motile *P. fluorescens* strain to 10 µm high linear grooves perpendicular to the flow direction and with different widths (10, 20, 30, and 40 µm). The authors found that the bacteria attached preferentially to the edges of the grooves, with more attaching to the downstream edge. This distribution was independent of the groove width and mobility of the bacteria, whereas the non-motile strain attached less to the overall substrate in general. The increased bacterial numbers at the edges of linear grooves could indicate, as for the border regions of the present study, that an increased contact area in edges is preferred for attachment. Furthermore, the authors identified small vortices at the structures' edges with CFD simulations and considered trapping of bacteria to cause higher cell numbers at the edges. As can be seen in the later presented CFD simulations of micro-hydrodynamics over 3D printed microstructures, two separate vortices form when the spacing-to-height ratio is >2.4. The spacing-to-height ratio of the nanorod arrays was 10. Thus small vortices in the border region were present and could contribute to a trapping of bacteria in this confined region.

In this study, an effect of microtopography to influence the attachment and retention upon high shear forces of bacteria could not be concluded. Only the comparison between the top and bottom aNR-glass provides a hint of which substrate type could have affected the attachment of the bacteria to microstructures. The increased cell numbers on the nanorods relative to the cell numbers in the interspaces for the top compared to the bottom aNR-glass suggests an influence of gravity: cells must move actively into the interspaces. The gravitation counteracts bacterial movement. Hence the effort for the bacteria to reach the interspaces, which were only accessible by active locomotion against the gravitation, was higher, as was the case for the top aNR-glass.

In the literature, there are contradictory results on the attachment of bacteria to microstructures. (Wang et al., 2014) investigated the initial attachment of *S. aureus* to 100 nm deep microwells of different diameters (1-5 µm) and spacings (0.5–10 µm). They found about 90% fewer cells attached to the substrates with microtopography than to the smooth control. Well diameter and spacing had no effect, except for a diameter of 5 µm and a spacing of 10 µm, where only 80% fewer cells attached. Two studies on bacterial attachment on several microstructures were published by the same group: one for *E. coli* (Graham et al., 2013) and one for *P. aeruginosa* (Ling, Graham and Cady, 2012). Both

presented two opposite findings. Attachment of *E. coli* compared to a smooth control was reduced by 30%, 65%, and 80% on 500 nm heigh continuous lines, staggered lines, and wells (1.7 µm diameter), respectively (Graham et al., 2013). Different spacing of the wells did not result in any change in bacterial attachment. However, attachment of *P. aeruginosa* to different types of pillars, square holes, lines, sharklet- and other microstructures showed no significant difference compared to a smooth control (Ling, Graham and Cady, 2012). In summary, publications show that the bacterial species has a significant influence on the attachment to microstructures, which is why comparisons between studies can actually only be drawn within a species or strain. However, no other publication was found dealing with the attachment of *P. fluorescens* on microtopographies under flow conditions and in-situ investigation. Hence more research is necessary in this field.

4.2 Part II: Bacterial Attachment and Retention under Micro-hydrodynamic Effects

In the previous section, the direct effects on bacterial attachment and the ability to remain on nano- and microtopographies were investigated. In the following, the indirect effects of 3D printed microstructures on bacterial substrate interaction will be discussed. Specifically, confined flow separation at the surface and narrow fluctuating shear stresses will be addressed as those kinds of effects.

4.2.1 Evaluation of Micro-hydrodynamics for 3D Printed Microstructure Design

CFD simulation of the micro-hydrodynamics in the vicinity of 3D printed structures was done for flow rates of 0.01 ml/min and 0.2 ml/min. The uniform cuboidal-shaped blocks were separated by small gaps in the y-direction and spacings of increasing size in the flow x-direction. Thus, the type and quality of micro-hydrodynamic effects could be systematically assessed.

Velocity vectors indicate the formation of circular vortices in the interspaces of cuboidal-shaped blocks for two flow rates, as seen in Figure 4-18. The velocity vectors are oriented parallel to the direction of flow. Above the structures, the velocity vectors indicate a linear faster flow. This linear flow, which is unaffected by the surface and comprises a large part of the water column in the channel, is called bulk flow.
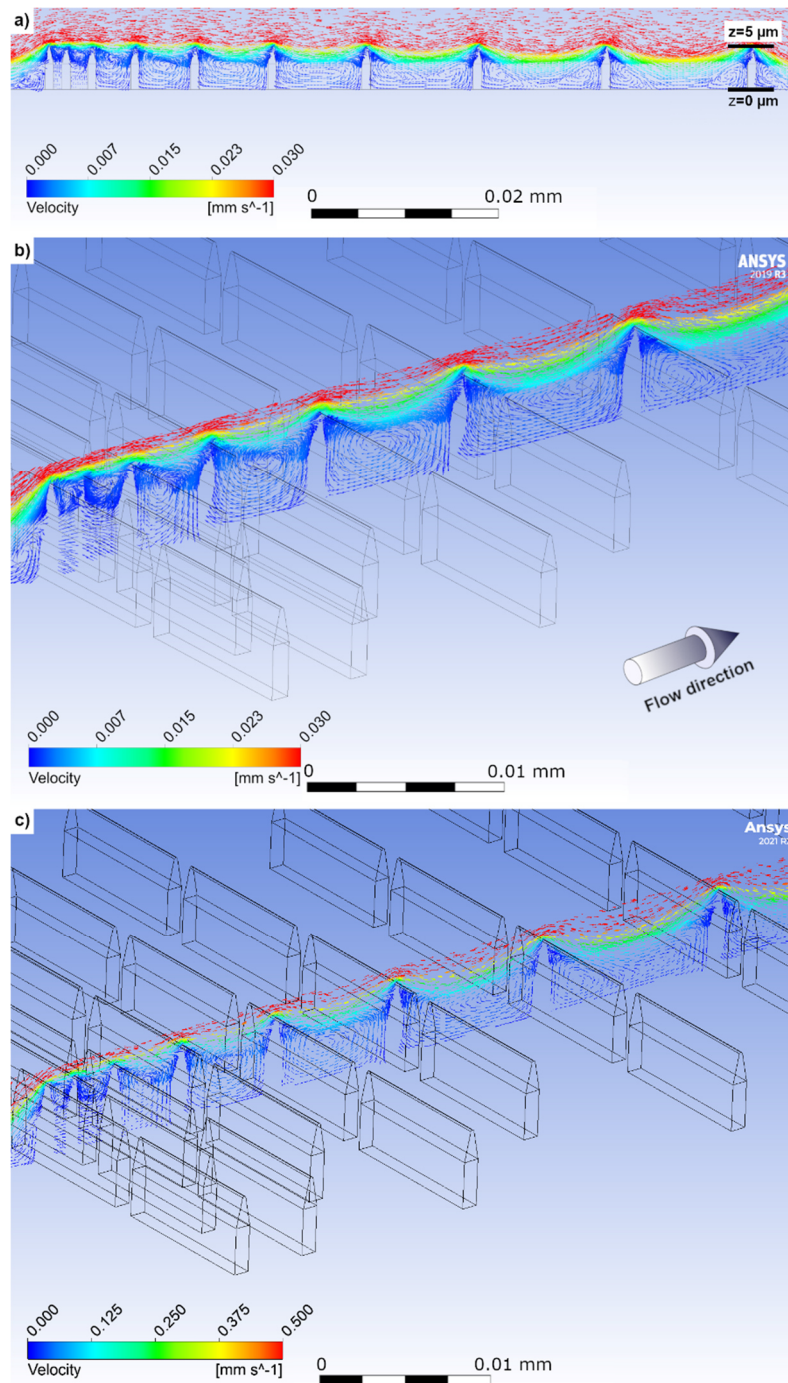
Figure 4-18: Fluid flow in the vicinity of blocks, protruding into the flowing liquid represented by velocity vectors. The different distribution of the velocity vectors is due to the size and shape of the calculated volume elements. In the lower zone, these are uniformly cuboidal-shaped, while above these are tetrahedral. The block spacing is 1 µm, 2 µm, and 2 µm more to each next block from left to right. Presented is a cross section with markings on the right indicating the height (z) from the coverslip substrate on which the fluorescence microscopy images were focused (a) and a perspective close-up of a vertical projection plan (b) for a flow rate of 0.01 ml/min. The shaded arrow shows the bulk flow direction. A perspective close-up of velocity vectors on a vertical projection plane for a flow rate of 0.2 ml/min is shown in c).

Below a spacing of 4 μm, the vortices are located in the upper region between the converging ridges. With increasing spacing, the center of the vortices moves to the surface. Above a spacing of 10 μm, the vortex separates into two. As the spacing increases further, the vortices become smaller and move toward the edges of the substrate and block wall. Simultaneously, the bulk flow enters the spaces between the blocks and, at 16 μm spacing, reaches the surface.
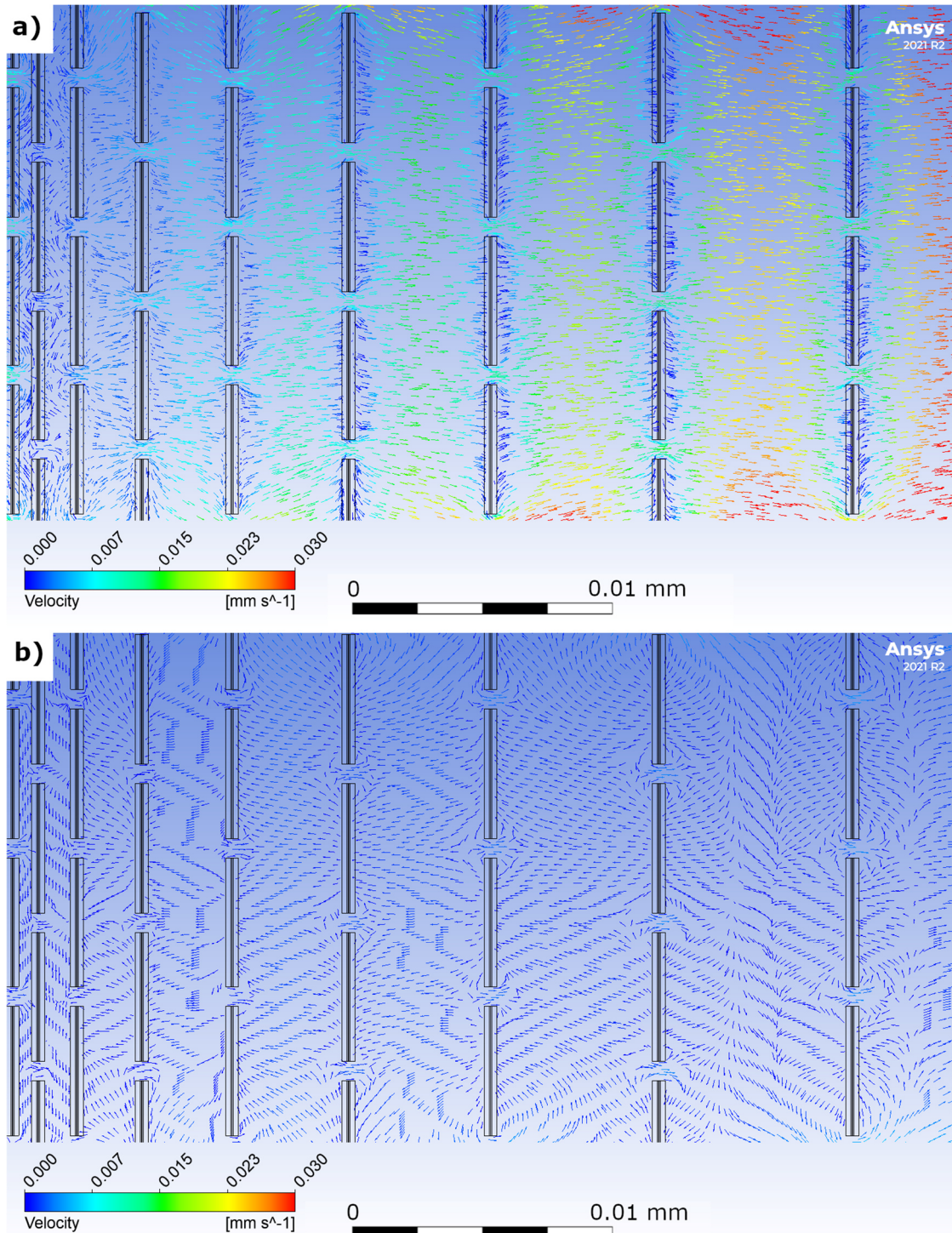
Figure 4-19: Top view on a horizontal projection plane of velocity vectors at z=4 μm (a) and z=0.5 μm (b) for a liquid flow of 0.01 ml/min in the vicinity of blocks. The bulk flow direction is from left to right.

It is noticeable from Figure 4-19 that the azimuth angle of the vectors also differs. In the upper zone near the ridges (Figure 4-19 a), the vectors are aligned in the flow direction with increasing spacing. At 1 μm and 2 μm spacing, the vectors describe a horizontal vortex between the gaps. Near the surface (Figure 4-19 b), the backflow is noticeable at 4 μm to 12 μm spacings. They belong to the vertical vortices, which are depicted in Figure 4-17 (a). In the smaller spacings near the surface, the vectors are aligned toward the next gap in the flow direction. Thus, they indicate an additional sub-flow beneath the vortices. At a spacing larger than 12 μm, the two separated vortices are represented by two zones of backflow with two adjacent convergency lines, where the flow is pushed to the sides. For a flow rate of 0.2 ml/min, the orientation of the velocity vectors was the same and only the velocity values were higher; thus, the flow profiles were similar.

The combination of the vertical and azimuth angle of the vectors is reflected by streamlines, where fluid particles are tracked over time. Figure 4-20 shows that the streamlines describe helices, with the pitch of the helix decreasing with increasing spacing of the blocks. The large helix pitch explains the large azimuth angles at 1 μm and 2 μm block spacing in Figure 4-19 (a). As the flow profiles for the different flow rates were the same, the streamlines were similar and differed only in the velocities.
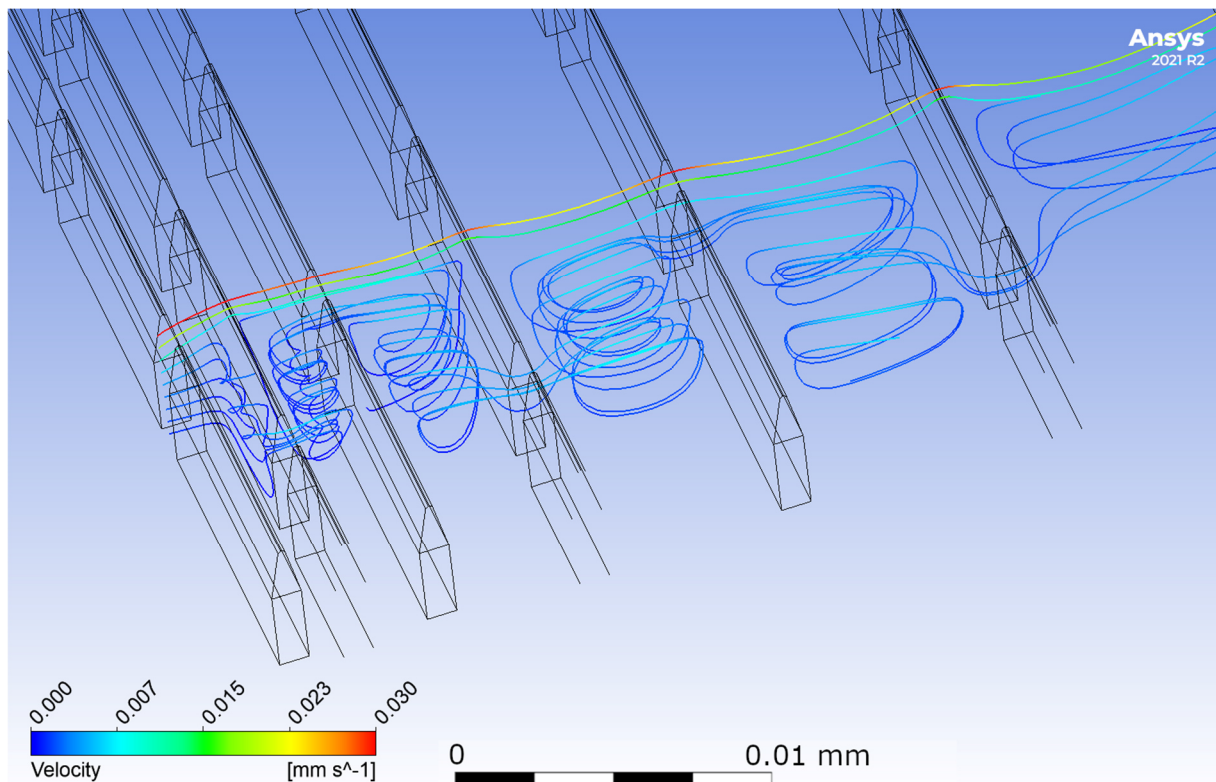
Figure 4-20: Streamlines on blocks of different spacings starting at a line centered in a gap for a flow rate of 0.01 ml/min.

The shear stress on the blocks is presented for 0.01 ml/min and 0.2 ml/min in Figure 4-21 a) and b), respectively. It can be concluded that attached bacteria experience the highest shear stress on the ridges, while the shear stress decreased abruptly toward the block part below. For a flow rate of 0.01 ml/min and 0.2 ml/min, the shear stress was 97 mN/m^2 and 3200 mN/m^2, respectively. Thus, after the attachment time, the purging steps induced a 32 times higher shear rate on the ridges. The high shear stress on the ridges is caused by a faster flow over this block part. The shear stress in the central part of the block is overall equally low.

Based on the visual results of the fluid simulation, four different spacings were chosen for MPL to reflect different hydrodynamic situations: 1 µm to include the flow blocked by small vortices in the upper block part, 4 and 8 µm to include the situation with established vortices overall in the interspace, and 14 µm at which the bulk flow is no longer blocked to the surface. The respective spacings were considered in an .stl file which was comprised of rows of blocks with large extension. Such a file was used as printing instruction for MPL. No specific design needed to be considered for the converging upper third of the blocks. Instead, simple cuboidal-shaped ones were designed. Fortunately, the ridges formed by themselves due to the characteristics of the MPL process.
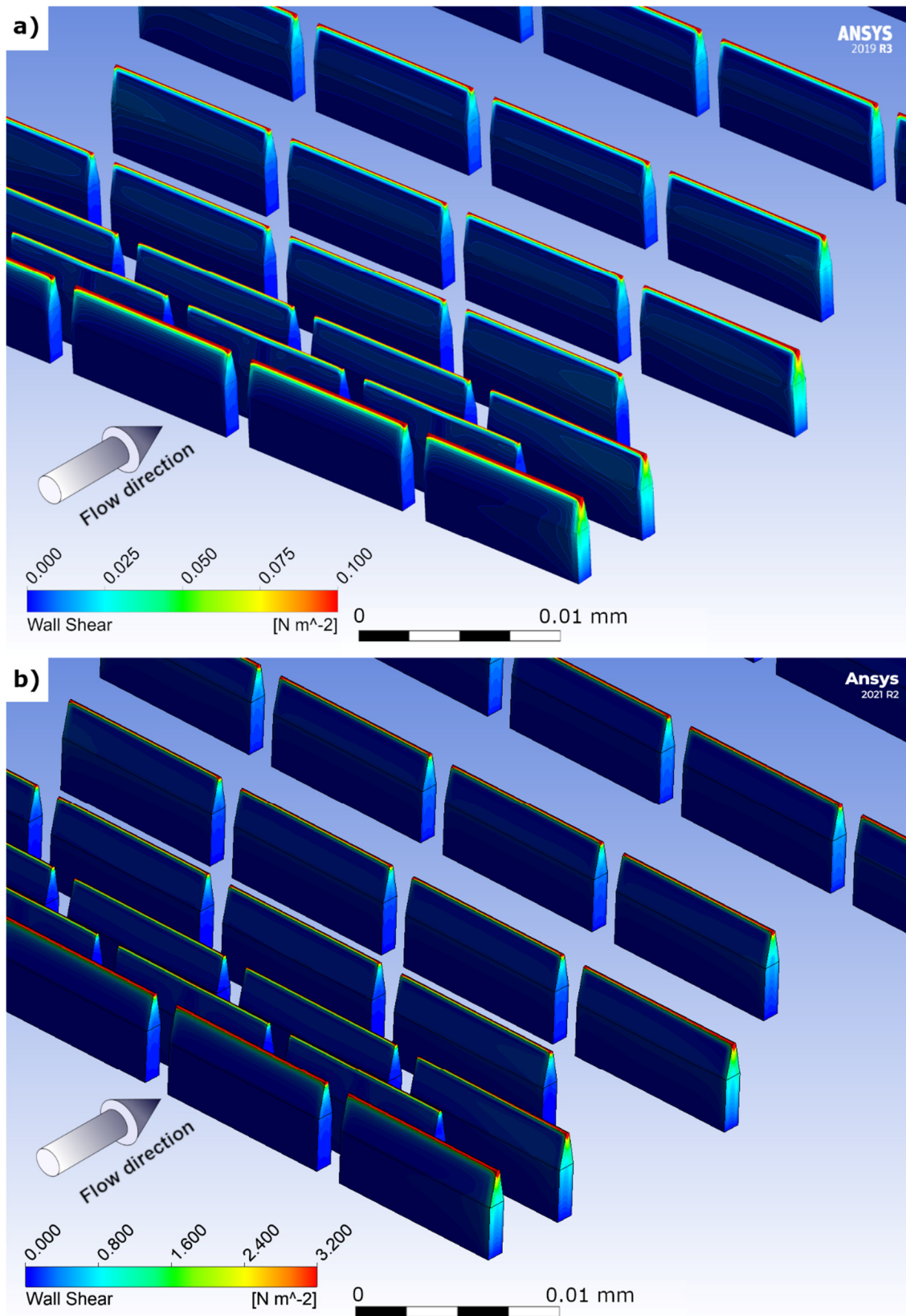
Figure 4-21: Shear stress on the walls of blocks protruding into the fluid flow for a flow rate of 0.01 ml/min.(a) and 0.2 ml/min (b).

4.2.2 Imaging of 3D Printed Microstructures

3D printed polymer surface microstructures on coverslips prepared by MPL were imaged with SEM. Figure 4-22 shows an overview of a sample for an attachment experiment with areas of different block spacing. The areas were of the dimension that one microscopy image could be taken vertically and several images horizontally of the same block spacing. The horizontally repeatable imaging ensured the reproducibility of the respective block geometry parameters and the predominant bacterial attachment situation. The horizontal extension of the areas was possible by stitching a smaller subarea. This stitching was accomplished by repeatedly executing the .stl instruction files, while in between the MPL process, the coverslips were each time shifted by the dimension of the .stl file.

The printing process resulted in a narrowing in the upper quarter of the blocks, which ended in a rounded ridge (see Figure 4-23 a). Viewed from the front, as in Figure 4-24 a), two small bumps on the short sides are noticeable, which also arose from the printing process.
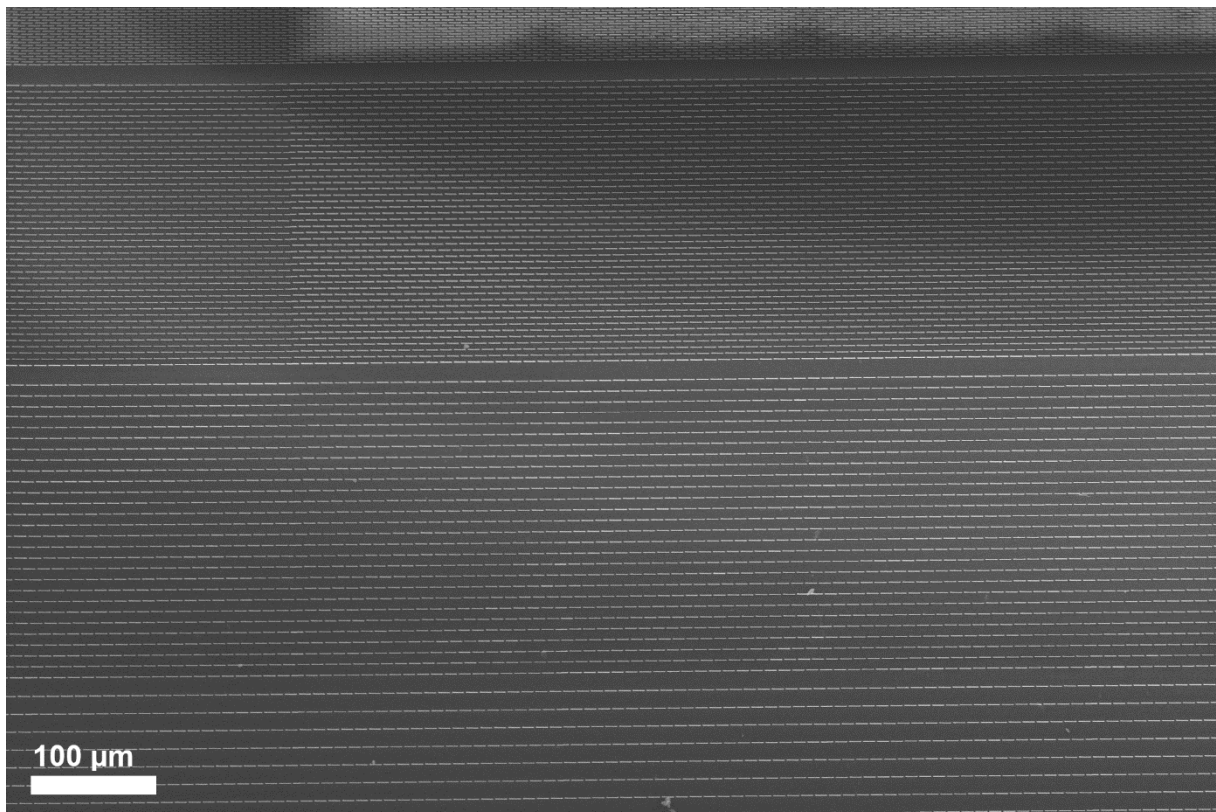
Figure 4-22: Stitched areas of 3D printed microstructures with different block spacing on a coverslip glass. The spacing in the image increases from 1 µm (top) to 14 µm (bottom).
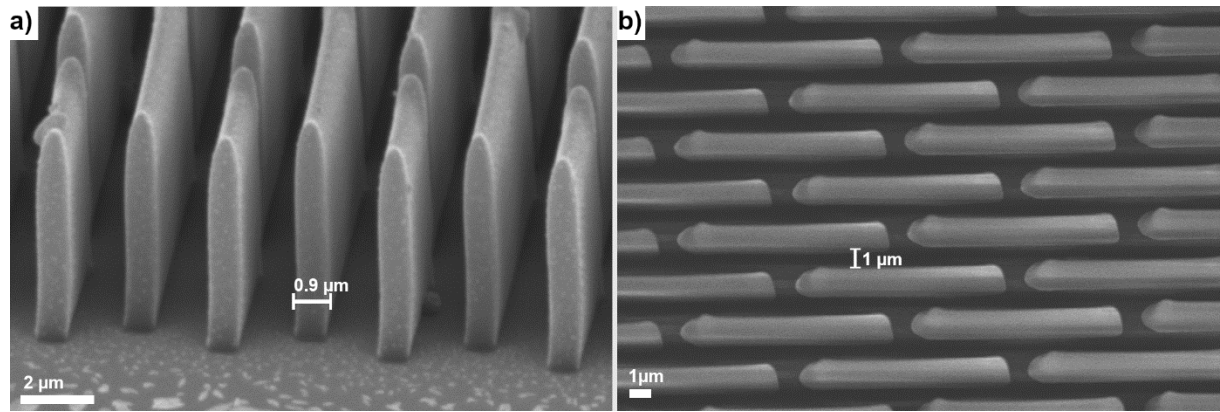
Figure 4-23: 3D printed block structures with 1 µm spacing side view (a) and top view (b). The dead bacteria and debris, which can be seen in a), are due to the imaging after the attachment experiment.
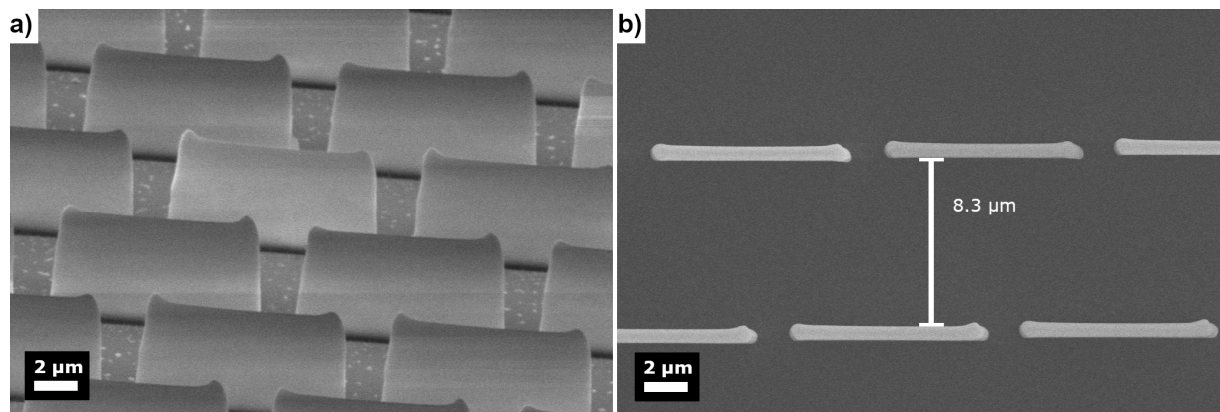
Figure 4-24: 3D printed block structures with 8 µm spacing front view 60° tilted (a) and top view (b).

4.2.3 Influence of 3D Printed Microstructures on the Bacterial Attachment and Retention

Attachment experiments with *P. fluorescens* SBW25 pMRE-Tn7-155 on 3D printed microstructures were performed and evaluated. Multiple image z-stacks per each area with a specific spacing of the microstructures were acquired. Each z-stack reflected the attached bacteria at the ridges of the blocks at z=5 µm and between the blocks at z=0 µm. At least five experiments (labeled I to V) were performed with all four block spacings (1 µm, 4 µm, 8 µm, 14 µm). In contrast to part I, only one image channel (yellow channel) was recorded and evaluated in this part.

Figure 4-25 exemplifies the situation of attached bacteria: the microorganisms were found preferentially on the surface or ridges of the blocks. Therefore, focusing the z-stacks on the surface (z=0 µm) and ridges (z=5 µm) was sufficient to image the attached bacteria with fluorescence microscopy. It should be noted that only a small fraction of the bacteria which could be observed in the light microscopy images remained for the SEM observation. This decrease in attached bacteria was

due to the sample preparation process for the SEM. Hence, enumeration of bacteria in SEM images would have not been an appropriate method to study bacterial attachment.
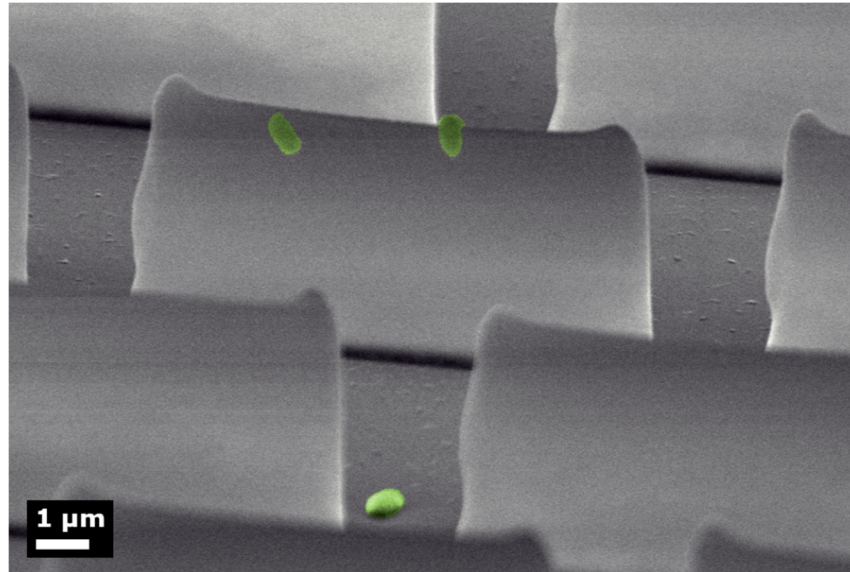
Figure 4-25: 60° rotated front view of 3D printed blocks with 8 µm spacing. Colorized image.

Examples of two-image z-stacks at a certain position for the different block spacings captured with fluorescence microscopy are shown in Figure 4-26. Bacteria sitting on the ridges of the blocks like a string of pearls can be clearly identified for spacings > 1 µm (c,e,g), whereas they are randomly scattered between the structures in d), f), and h) for spacings > 1 µm. For 1 µm spacing only three bacteria were visible between the structures (Figure 4-26 b). It can be seen that the number of bacteria in the interspaces increases with larger spacing.
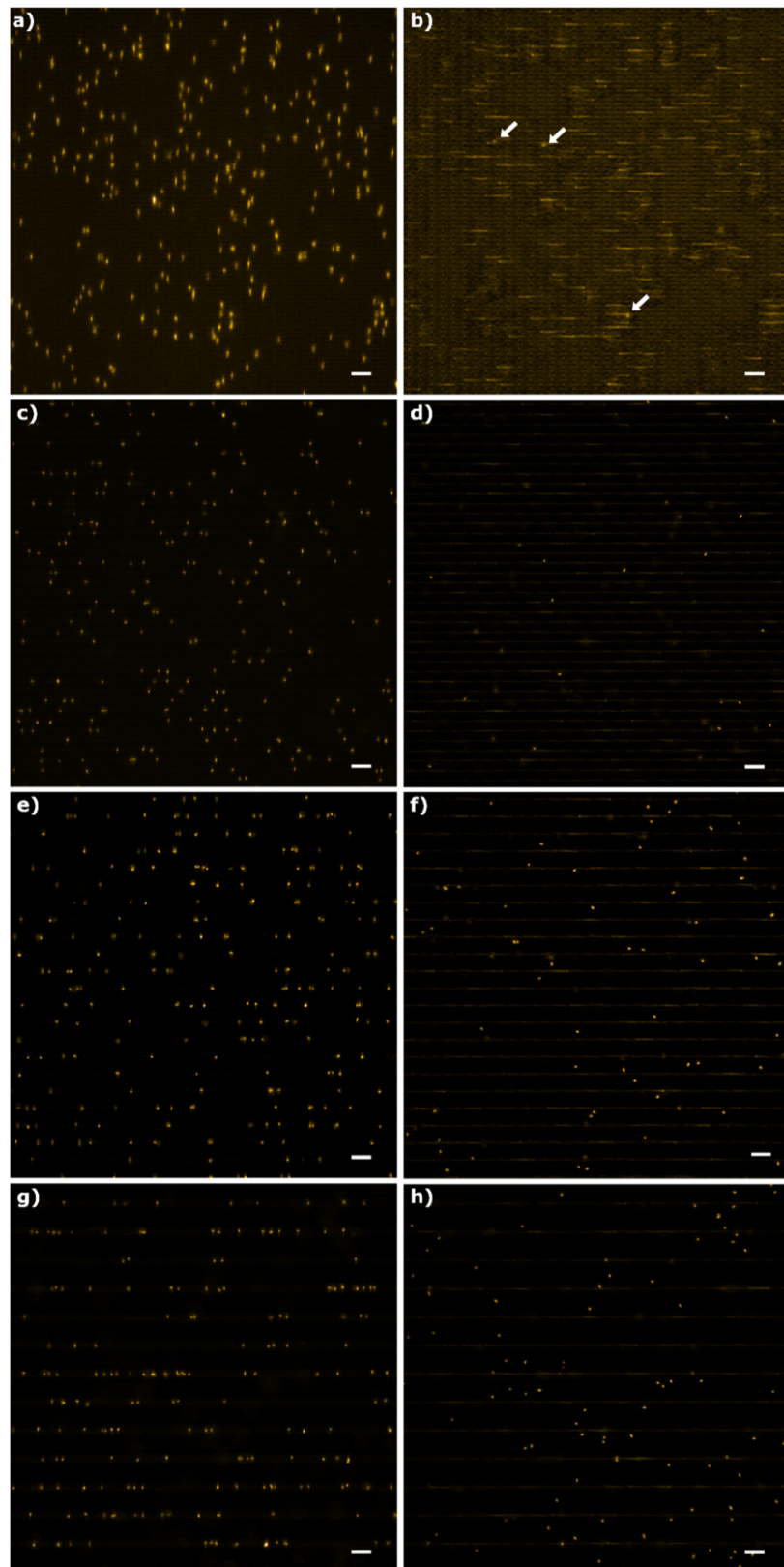
Figure 4-26: Fluorescence microscopy images (yellow channel) of *P. fluorescens* cells attached on the ridge of 3D printed structures with 1, 4, 8, 14 µm spacing on the ridges at z=5 µm (a, c, e, g, respectively) and on the coverslip surface between structures at z=0 µm (b, d, f, h, respectively). Arrows in b) mark the position of bacteria in the interspaces. The images were acquired at 578–610 nm band and 630x magnification. The images are adjusted in contrast and brightness for clarity. The scalebars are 10 µm.

Visual differentiation of the cell numbers on the ridges was difficult, which illustrates the advantage of a software-based enumeration. The beneficial use of the plugin "Find Maxima" in ImageJ can be explained by Figure 4-26 a) and b). The smallest block spacing led to a scattering of the illumination light at the structures, causing a blurring of the cells. However, the plugin was able to identify the local brightness maxima of the spots, which were caused by each cell, better than the human eye.
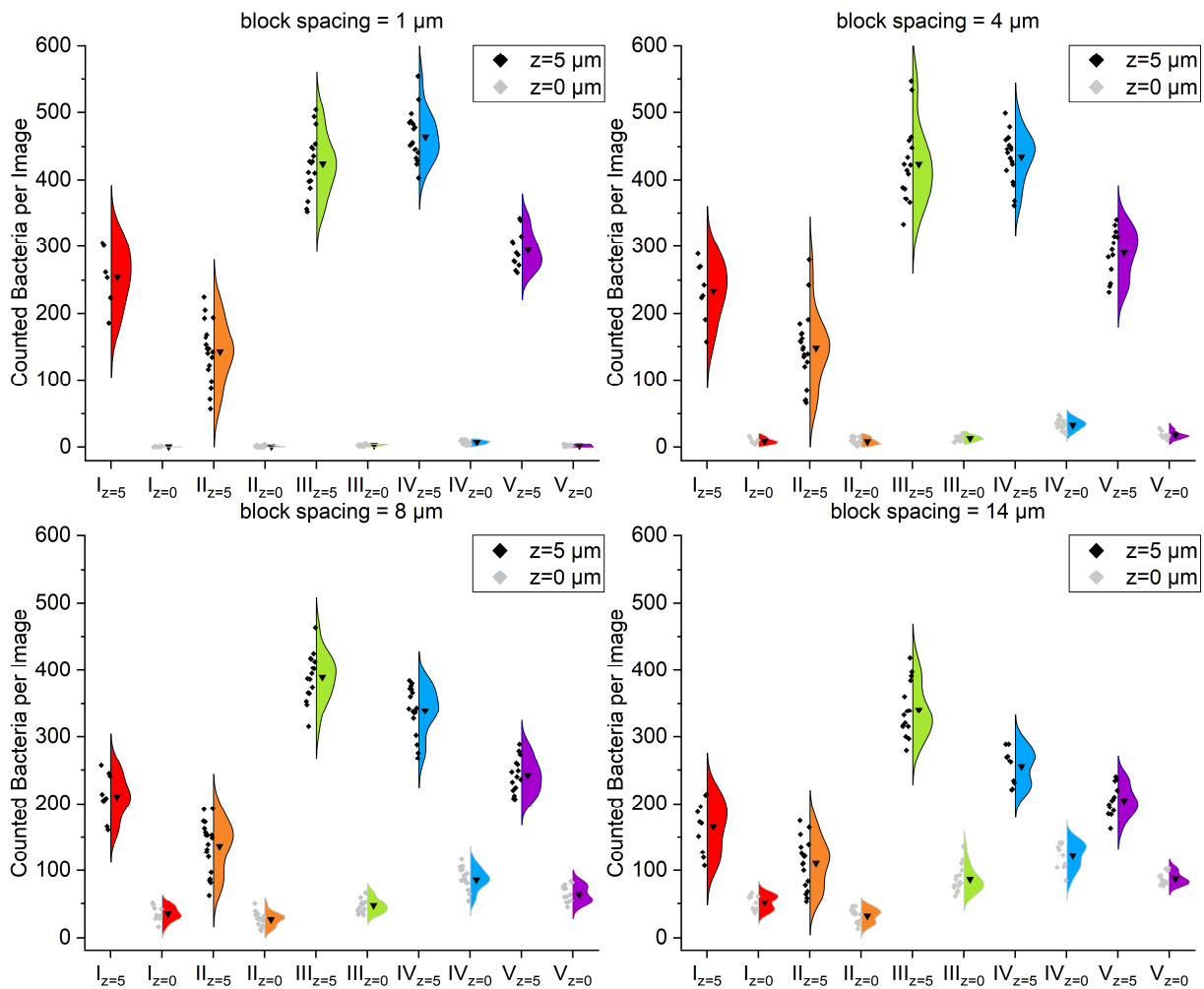
Figure 4-27: Counted bacteria per image (211x211 µm²) for five repetitions (I-IV) at the ridge of 3D printed microstructures (z=5 µm) and between the structures on the coverslip surface (z=0 µm). The spacings of the structures in flow direction were 1 µm, 4 µm, 8 µm and 14 µm, the height was 5 µm. Each black or grey point resembles the bacteria number in one captured image.▼ = arithmetic mean.

The ratios of attached bacteria at z=0 µm and z=5 µm varied for the different block spacings (Figure 4-27). For a block spacing of 1 µm, no bacteria to only four bacteria per image entered the spaces between the 3D structures. In contrast, a higher number of bacteria attached to the ridges. The arithmetic mean number of bacteria on the ridges was the highest for 1 µm block spacing compared to the other block spacings. With an increase in the spacing, the ratio of the number of bacteria on the ridges to the number of bacteria in the interspaces decreased. However, the number of bacteria at

z=0 µm never exceeded the number of bacteria at z=5 µm and was significantly lower. As for the ZnO and glass substrates observed, bacteria once in contact with the surface stayed at the position. The cells tumbled for a while, with the flagellum anchoring them to the substrate until firm fixation with no movement.

Large variations between replicates were identified. The arithmetic means differed in some cases by a factor of three, both within the group of z=5 µm and within the group of z=0 µm. The variations between replicates were a consequence of flow inhomogeneities in the bulk flow, as for the ZnO surfaces. The flow inhomogeneities were reflected in varying total cell numbers in the microscopy images when imaging was done in the y-direction for the respective block spacing.
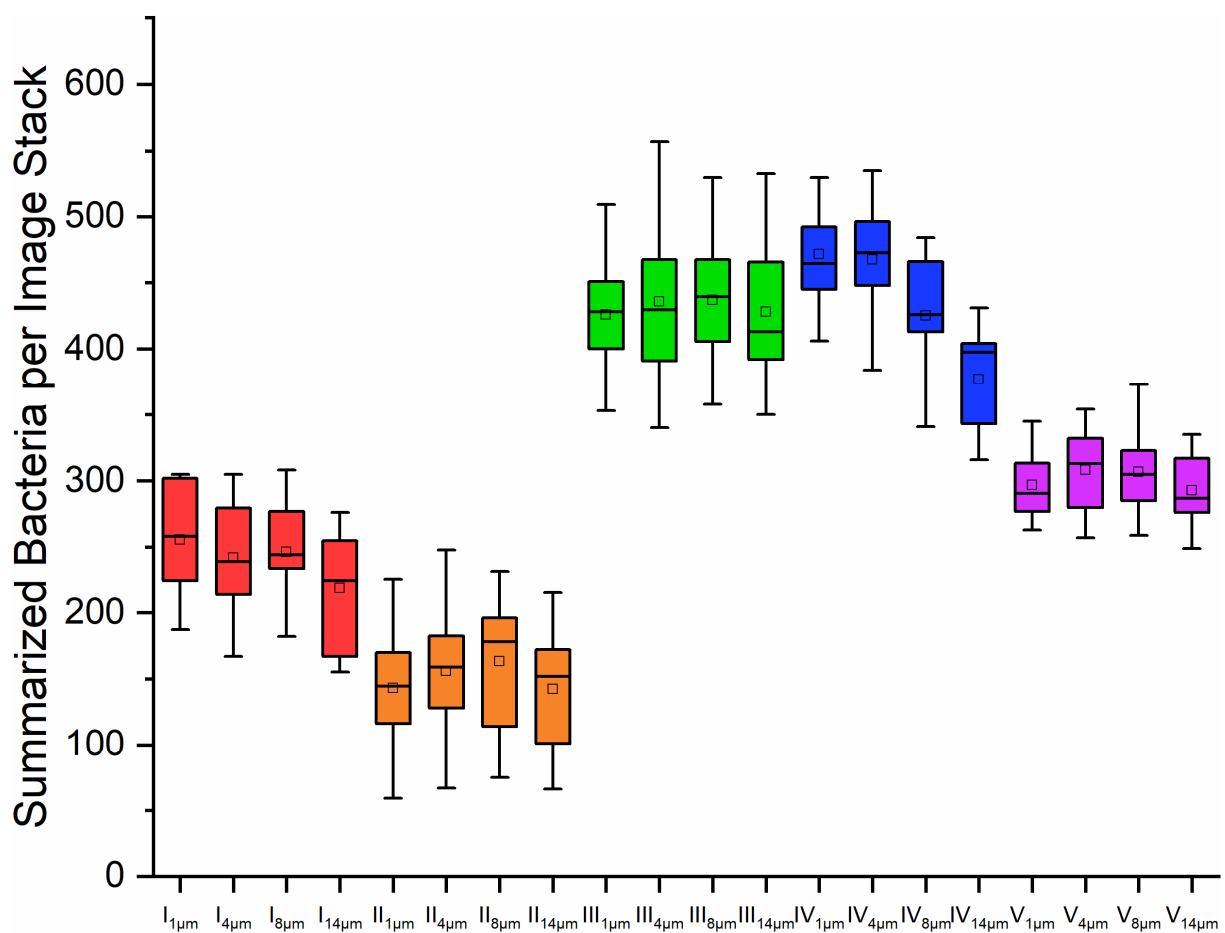
Figure 4-28: Box plots for the total number of bacteria per image stack, which included two images (z=0 µm and z= 5 µm) at each position in an area scan. The total number is the sum of all bacteria between 3D printed structures and at the ridge at a certain image position. Five repetitions (I-V) were done, each with four different block spacings (1 µm, 4 µm, 8 µm, and 14 µm). The colored marked repetition shows which groups (spacings) were tested for significance with an ANOVA.

The total number of bacteria per image section, consisting of the counted cells at z=0 µm and z=5 µm, is plotted in Figure 4-28 for each block spacing. The factor of the available area of polymer per image

section was not considered, as it was done by normalizing the cell number for aNR-glass with its different substrate types in part I (see section 4.1.4). The reason was that the studies on the 3D-printed block structures should reveal whether there was a general effect of different microhydrodynamics on the attachment and the ability of bacteria to remain.

Visual inspection of Figure 4-28 suggests that in each replicate, the number of attached bacteria is similarly distributed between the groups but varies between the replicates. ANOVAs were used to test for significant similarity within each replicate to verify the suggestion that similarity exists within the groups. The different block spacings were examined as groups (DF=3). The ANOVA F-test yielded F≈1 except for replicate IV, where F=13.81. The null hypothesis that all spacings had significantly similar means of attached bacteria per image stack cannot be rejected for all replicates except for replicate IV. For replicate IV, a post-hoc Tukey's test showed significant similarity in means for all pairwise group comparisons except IV_{1um} to IV_{4um}. In summary, the statistical hypothesis testing supports the assumption that no significant differences in the attachment behavior of the bacteria exist for the majority of the samples examined. The different block spacings seems not to influence *P. fluorescens* attachment.

4.2.4 Discussion

It could be demonstrated for the first time that 3D printed microstructures created by MPL can be well used for attachment experiments of bacteria. The hydrodynamic situations that form in a flow chamber in the vicinity of structures on the surface could be evaluated in advance by fluid simulations. This approach allowed the optimal dimensions of the structures to be selected in a targeted manner. The simulation with distinct structures could be transferred to reality with high reproducibility by the MPL procedure.

For classical microfluidic PDMS devices, definite surface microstructures must be implemented in the mold using lithographic method (Pousti et al., 2018). The mold and the casting step are omitted in the fabrication of microstructures with MPL. Instead, the structures are printed directly on a coverslip which can be used as a channel wall in the flow chamber. This procedure facilitates and reduces the time of sample preparation, which means an advantage of MPL. Other advantages are the possibility to create more elaborated structures and the variety of available materials. The disadvantage of MPL is that only one sample can be made at a time, while more PDMS devices can be produced with more molds in parallel. Thus, MPL is particularly well suited for testing prototype samples for flow chamber experiments

Simple cuboidal-shaped structures were chosen for the experiments. Only the spacing between rows of these blocks was varied. It was found in all attachment tests that bacteria attached to both the ridges and to the surface between the blocks. Compared to the attachment of bacteria on ZnO nanostructures and glass, no reduced attachment of the total bacteria due to micro-hydrodynamic effects was observed. However, the ratio between bacteria attaching to the ridges and on the surface between the blocks varied for different spacings. The larger the spacing, the more bacteria were counted on the surface, and the fewer were on the ridges. This distribution could be caused by the micro-hydrodynamic situation near the 3D printed structures. Using CFD simulations, flow separation was confirmed: vortices formed, which blocked the bulk flow from the interspaces and should prevent the bacteria from getting in contact with the surface. However, once a bacterium entered the vortex, it was likely to be transported to the surface, as it has been suggested by Yang et al. (2021).

The high bacterial counts in the interspaces between the blocks with 14 µm spacing compared to the bacterial counts in the interspaces of blocks with lower spacing might be due to the bulk flow reaching the coverslip surface and the vortices being only at the ridges. On the other hand, it must be noted that at the small spacing, more ridges on an area were available for bacteria to attach, whereas at the 14 µm spacing, there were fewer.

Nevertheless, it is surprising that the bacteria were seemingly unaffected by the 3D printed microstructures, despite other studies claiming differently. Although the ridges of the blocks caused increased shear stresses and were very thin in the direction of flow, the bacteria attached to them. As in the experiments with glass and ZnO substrates, the flagella of *P. fluorescens* presumably played a key role in the fixation. The temporary tumbling motion of the bacteria on the flagella was also observed in experiments with the 3D printed microstructures. Thus, the flagella acted like an anchor that easily offered a first linkage to the substrate. The bacteria are then able to pull themselves with appendages to the surface, were they achieve irreversible attachment through bond maturation. Hence, the induced wall shear stress after purging the flow chamber (32 times higher than during the bacteria attachment phase) did not cause the bacteria to detach.

The flagella might have served yet another purpose: the active escape from the vortices to the bulk flow. Evidence for this can be found in the study of Scheuerman, Camper and Hamilton (1998). Motile *P. aeruginosa* and *P. fluorescens*, in contrast to a non-motile *P. fluorescens* mutant, could enter microgrooves where flow separation occurred. This study demonstrates that some bacterial species are capable to attach and remain at surface structures, despite these structures lead to surface blocking microhydrodynamics.

In contrast to the present study, two publications proposing a repelling effect on bacteria by microhydrodynamics are from Halder et al. (2013) and Choi et al. (2018b). Halder et al. (2013) observed a significantly reduced attachment of *E. coli* caused by the micro-hydrodynamics in the vicinity of microwells. The authors attributed the reduced bacterial attachment to sharp wall shear stress fluctuations, which developed at the confined protruding regions between microwells. The spacings for the effective microwell surfaces were 2 and 5 µm. However, Halder et al. (2013) used a different bacterial species. This could be a reason for the contrasting result of the present study.

Choi et al. (2018b) proposed, secondary flows with locally high velocities in the z-direction (up to 0.6 m/s) for micro-hydrodynamic effects. These provided the *P. aeruginosa* repulsing properties of microstructures, especially of structures mimicking the skin of sharks. The secondary flows in the z-direction were the net result of helical vortices between the structures. Such helical flows were also observed in this study, especially in the upper interspaces of the blocks with 1 µm and 2 µm spacing. However, the effective micro-hydrodynamic properties were a consequence of the high flow velocities generated at 15.5 bar pressure. This high inlet pressure provided a maximum wall shear stress of up to 16 N/m^2. The flow parameters differed from those of the above cited publications of (Scheuerman, Camper and Hamilton, 1998) and Halder et al. (2013), and the present study. In these studies the wall shear stress was much lower with 0.83 N/m^2 (Scheuerman, Camper and Hamilton, 1998), 0.5 N/m^2 (Halder et al., 2013), and 0.097 N/m^2, respectively. These lower wall shear stress values were a consequence of lower flow velocities, which led to weaker micro-hydrodynamics and reduced repulsive surface effects. Such a relationship between the flow velocity at the inlet and the effectiveness of resulting hydrodynamics on surface structures was identified by Kumar et al. (2012). At semi-confining structures on the sidewalls of a flow channel, bacterial attachment and biofilm formation decreased with increasing flow velocities. At the highest flow velocity, almost no bacteria penetrated the area of the structures, and attachment as well as biofilm development occurred only in the area of the bulk flow. The authors attributed this to vortices, which had a stronger effect as the flow velocity increased. Furthermore, it should be noted that a wall shear stress of 16 N/m^2, accounting for a shear rate of 16700 s^{-1}, in the study of Choi et al. (2018b) would imply for *P. fluorescens* cell detachment, as the shear rate was above the threshold for detachment (12000 s^{-1}) (Busscher and van der Mei, 2006). Therefore, it is questionable for the study of Choi et al. (2018b) whether cell attachment was prevented by microhydrodynamic effects or if it was due to the high wall shear stress. In conclusion, considering the flow conditions, they must be in a range transferable to real environments (Senevirathne et al., 2021), which was the case in the present study.

In summary, a bacterial repelling effect of microhydrodynamics induced by 3D printed microstructures could not be demonstrated in this study. As microhydrodynamics, both strongly fluctuating wall shear

stresses and surface turbulences providing flow separation were addressed. The causes lie in the many different aspects that influence the attachment of bacteria and their ability to remain on the surface. Some of these are more important than others. In the present study, it was found that especially the bacterial species or strain and whether they have flagella or are round cocci have an important influence on bacterial attachment. Micro-hydrodynamics probably only have an effect at higher flow velocities and consequently higher shear stresses.

4.3 Part III: Lipopolysaccharide Encapsulates Polystyrene Microparticles

In this study an innovative and practical route was developed to design synthetic model microparticles resembling bacterial cells. To achieve this goal, a swell-capture mechanism to incorporate lipopolysaccharides onto the surface of PS microparticles, was used.

4.3.1 Surface Characterization

PS microparticles were treated with a swell-capture procedure and a mixture of LPS in PBS with different concentrations. Furthermore, as a reference, PS microparticles underwent the same procedure but were treated only with PBS.

ζ-potential measurements of the LPS-PS microparticles and the reference are presented in Figure 4-29. Measurements of the suspensions of LPS in PBS used for the PS treatment are included. The lowest ζ-potential value (-31 mV) had PS microparticles without LPS, while the two treated with the highest LPS concentration had the highest values ($\approx$-16 mV). In between, an asymptotic increase was observed, which approaches saturation around the value -16 mV. The ζ-potential of LPS in PBS was higher than that of treated PS microparticles. However, the values fluctuated between the concentrations and a general trend could not be derived.
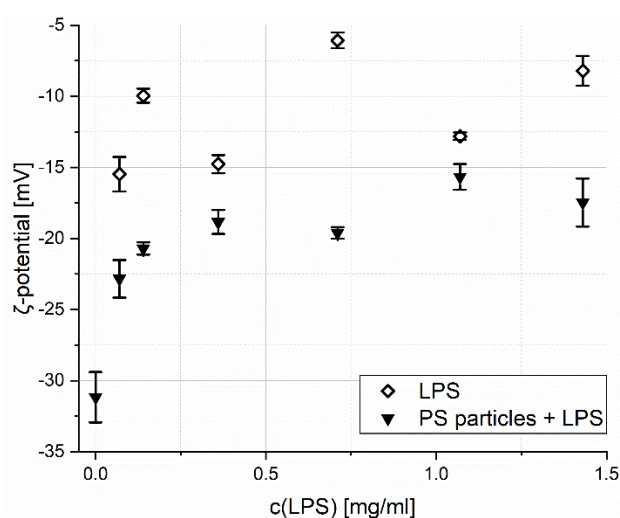
Figure 4-29: ζ-potential of LPS encapsulated PS Particles and of LPS in PBS as a function of the LPS concentration.

XPS was used to verify the encapsulation of PS microparticles with LPS. For this purpose concentration of nitrogen derived from the N 1s peak at $\approx$400.2 eV was evaluated. Since the very narrow outer region (<2 nm) was measured, any occurrence of this element is related to LPS, while in PS, no N exists. Hence, conclusions about the amount of LPS on the microparticles can be drawn from the XPS measurements.

An average measured N percentage is presented in Figure 4-30 a). The PS microparticles without LPS and those with the lowest LPS concentration showed no N occurrence. The highest value of ≈2% was found for S5, while the microparticles with lower LPS concentration had significantly lower values of ≈0.3%. S6 was in between with ≈1.2%.

Around 285 eV in the XPS spectrum is the carbon peak. It is a convolution of peaks resulting from different C species, including N-(C*=O)-C. Thus, the content of LPS in the sample could also be inferred from this species. The other C species could not be assigned to PS or LPS since they can occur in both. Figure 4-30 b) shows a similar picture to Figure 4-30 a): without LPS in the treatment, there was no LPS on the final LPS-PS microparticles. Up to S4, there was a plateau of 0.4% of the N-containing C species in relation to the total C content. S5 also had the highest N-content in the C species, as S6 lies between this value and the plateau.
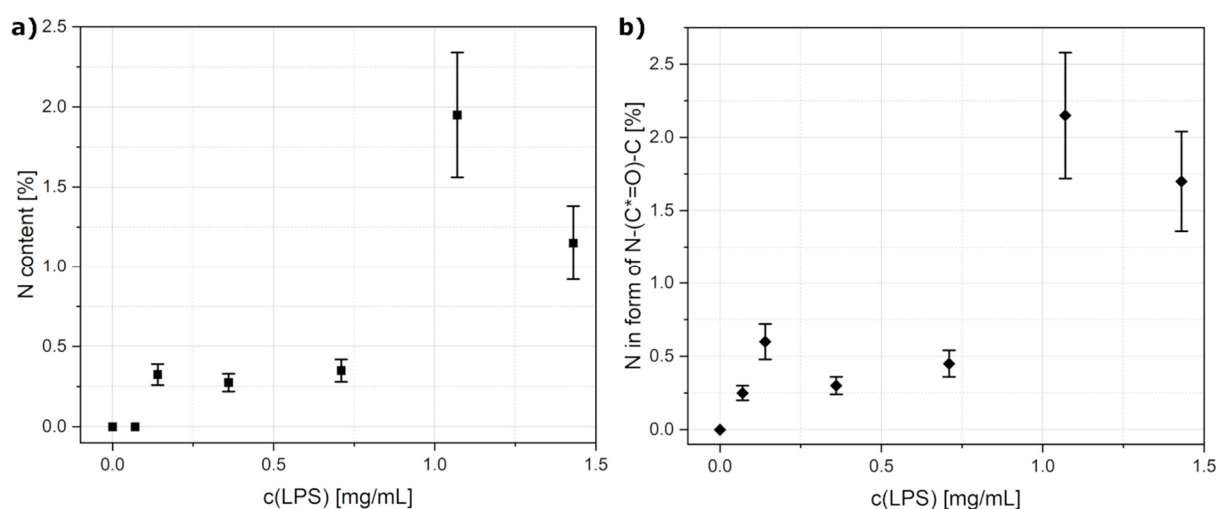
Figure 4-30: N content depending on LPS concentration used during microparticle preparation analyzed with XPS. Presented is the overall N percentage calculated from the N 1s-peak (a) and the percentage of nitrogen origination from N-containing carbon species in relation to all C species measured (b). The error bars indicate measurement uncertainty, which was instrument related.

As an example, the XPS detail spectrum of the carbon C 1s peak is displayed in Figure 4-31. One measurement was selected from each sample S0 and sample S5. The first left peak is the deconvolution of the species N-(C*=O)-C. The value for Figure 4-31 b) can be derived from the relative area and is the mean of all measurements of the respective sample. Remarkably, as LPS increases in treatment, the percentage of C species with oxygen also increases. They may originate to a small extent from PS initiators and additives but more likely from the sugar chains of LPS. However, high inter-sample variations did not allow to summarize the values of O-containing C species in one plot.

Peak name C1s_14	Peak height/ cps	Lorentzian	Position/ eV	FWHM/ eV	abs. Area/ cps·eV	rel. Area/ %
C-C, C-H	657.389	0.2	284.8522	1.2	907.34	92.28
C-OH, C-O-C	41.649	0.2	286.4436	1.2	57.59	5.86
C=O	2.46233	0.2	287.6468	1.2	3.4068	0.35
N-(C*=O)-C	10.806	0.2	288.8404	1.2	14.95	1.52

Peak name C1s	Peak height/ cps	Lorentzian	Position/ eV	FWHM/ eV	abs. Area/ cps·eV	rel. Area/ %
C-C, C-H	456.96	0.2	284.9071	1.275	674.11	56.89
C-OH, C-O-C	177.541	0.2	286.3294	1.275	261.96	22.11
C=O	132.156	0.2	287.3823	1.275	195	16.46
N-(C*=O)-C	36.563	0.2	288.4294	1.275	53.95	4.55

Figure 4-31: High resolution XPS spectra depicting the C 1s peak for S0 (a) and S5 (b), along with the fitting parameters for the corresponding species.

AFM-IR was used to obtain infrared spectra on the surface of the microparticles in area of a few 10th nm. This analysis was achieved by using the cantilever as a detector of thermal expansion. The thermal expansion was the result of a fine IR irradiation in the analysis area. In Figure 4-32, the IR spectra in the measurable range of 1900 – 900 cm^{-1} for S5, S0, and pure LPS are plotted. The measurements were taken on top of a microparticle and representative curves were chosen. Spectra of LPS exhibited a broad and relatively prominent peak in the carbohydrate region, which were attributed to the vibrations of C-O ring, COH, and C-O-C at 1036 cm^{-1} (Naumann et al., 1989; Kiwi and Nadtochenko, 2005). The peak at 1453 cm^{-1} could be assigned to C-H stretching vibration. Peaks at 1560 cm^{-1} and 1633–1655 cm^{-1}, corresponded to the Amide II band [ν(C-H) + δ(C-N-H)] and the Amide I band [ν(C=O)], respectively. The spectrum of S0 exhibited vibrational bands of C-H$_2$ and benzene rings at 1452 and 1492, which are typical of PS (Bhutto, Vesely and Gabrys, 2003). The C=C vibration peak at 1600 cm^{-1} can also be attributed to PS. For the spectrum of LPS-PS microparticles of sample S5, the penetration depth of the IR needs to be considered, which is in the range of a few 100 nm. As LPS has a length of 10–12 nm (Knirel, 1990), not only its presence was detected, but also always the underlying PS. Consequently, the spectrum of S5 was a combination of the other two curves.
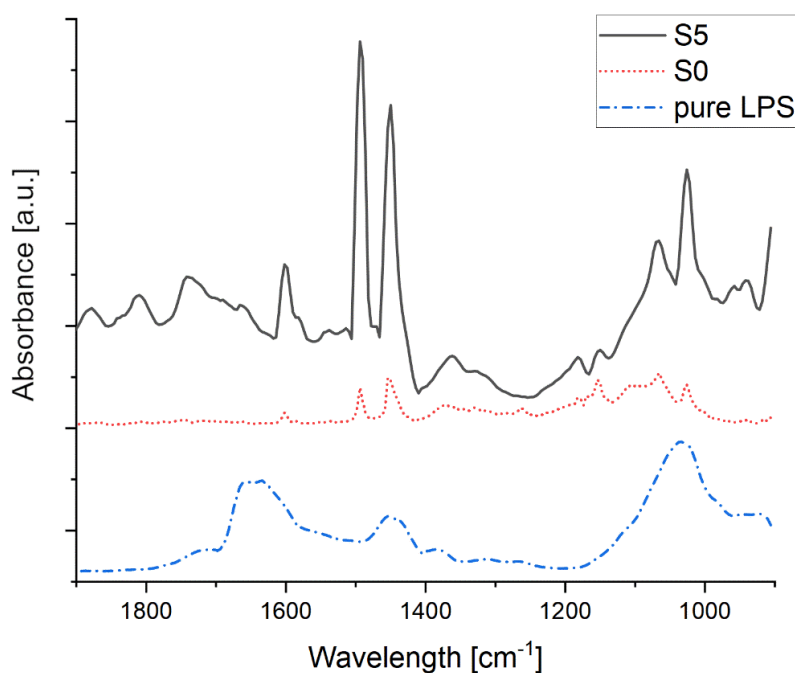
Figure 4-32: AFM-IR spectra on top of the microparticles of sample S5, S0, and pure LPS measured on an Au surface.

The topography measurements on PS microparticles by AFM are exemplary presented in Figure 4-32. On each sample on mica stripped gold, areas of close sphere packing were selected and the scan area was progressively reduced to achieve high resolution from the microparticle surface. For pure PS, S0, and S5, height images of the upper area of a microparticle are presented in Figure 4-34. It should be noted that the upper part of the microparticles had a curvature, which led to problems with flattening to a 2D image. Nevertheless, differences were visible for the microparticle types. The mere treatment with THF led to an alteration of the surface, albeit minor. Small threadlike structures on the surface were obvious, which envelop the microparticles of S5. Since the threads were missing on untreated PS microparticles and S0, it can be assumed that they were protruding LPS domains. As AFM imaging was done in air, the situation reflected the dried state of LPS.
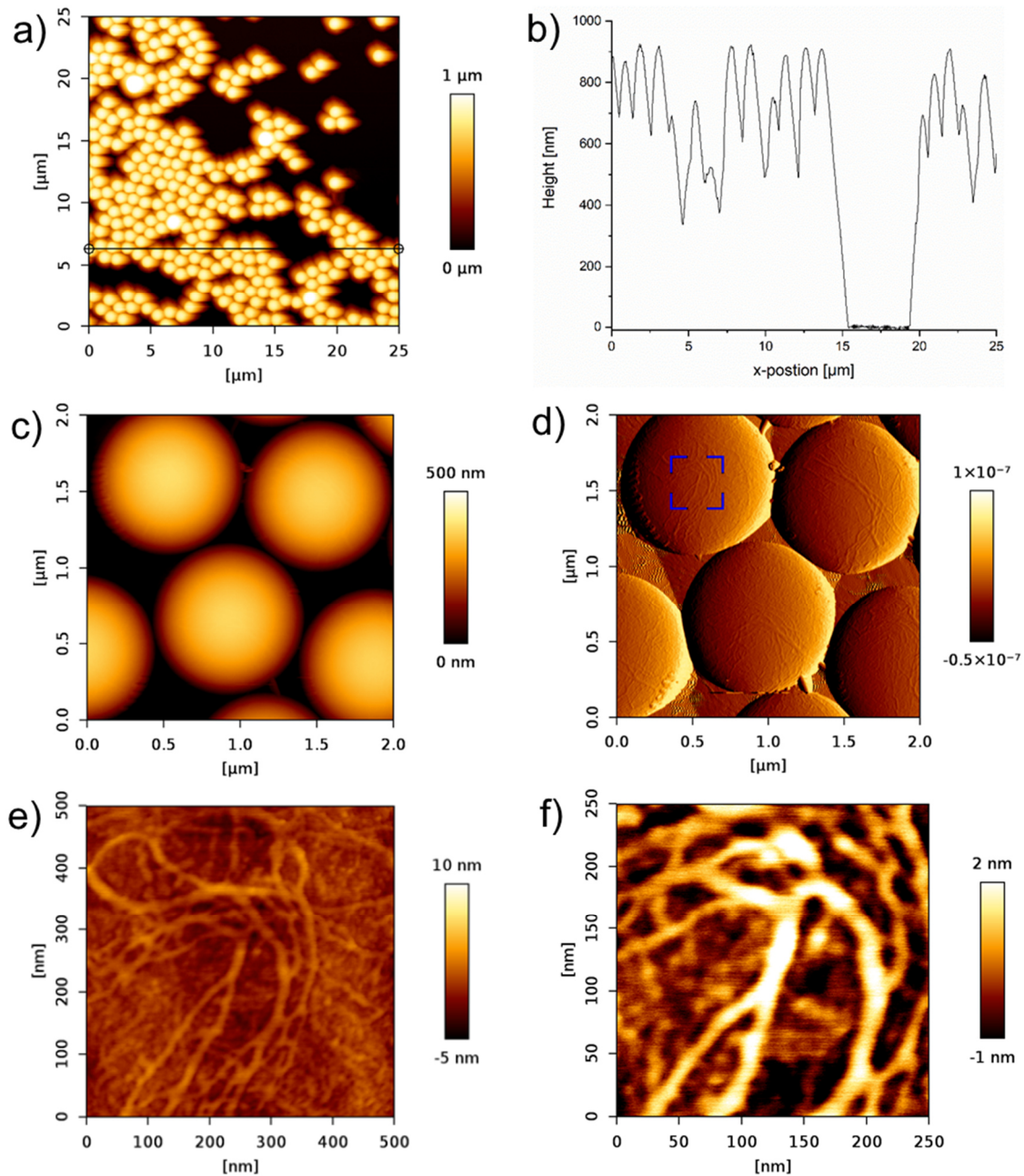
Figure 4-33: AFM height images of S6 on mica stripped gold. Presented is the measurement procedure as a zoom-in series with different magnifications. First, an overview was imaged (a). A cross section of the overview confirmed a microparticle monolayer (b). Next, the upper area of a few microparticles was imaged (c) with the corresponding derivative image confirming a close packing (d). On top of one microparticle, the position is marked blue, higher magnifications of 500 nm (e) and 250 nm (f) followed.
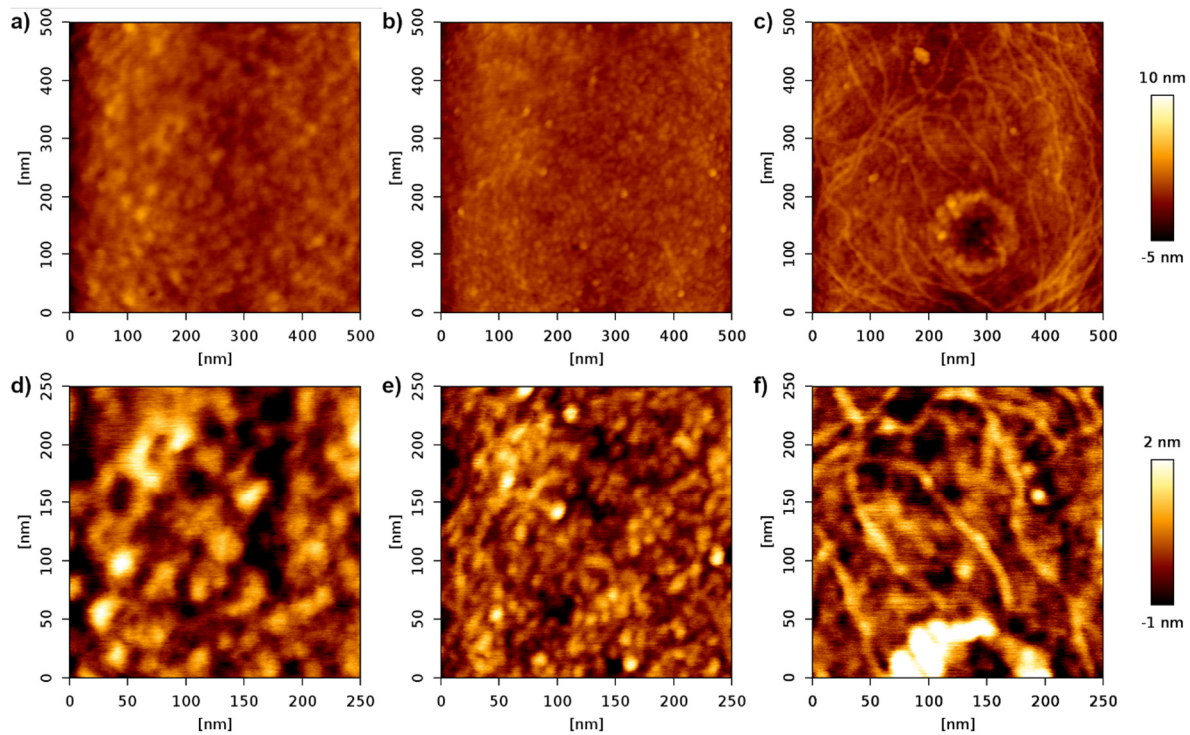
Figure 4-34: Height measurements with AFM show the surface of the upper area of microparticles with different magnifications; untreated PS microparticles (a,d), S0 (b,e), and S5 (c,f).

4.3.2 Evaluation of FITC Labeling

The microparticles of sample S0–S5 were labeled with FITC and investigated with fluorescence microscopy. As evident from Figure 4-35, fluorescence occurred only in microparticles of sample S5. The other samples, S1–S6, not shown here, also exhibited fluorescence; however, the intensity decreased with lower concentrations of treated LPS. FITC binds to primary amines (Skelly, Munkenbeck and Morrison, 1979). These amines can be found as substitutes in the *P. aeruginosa* core oligosaccharide (Lam et al., 2011).
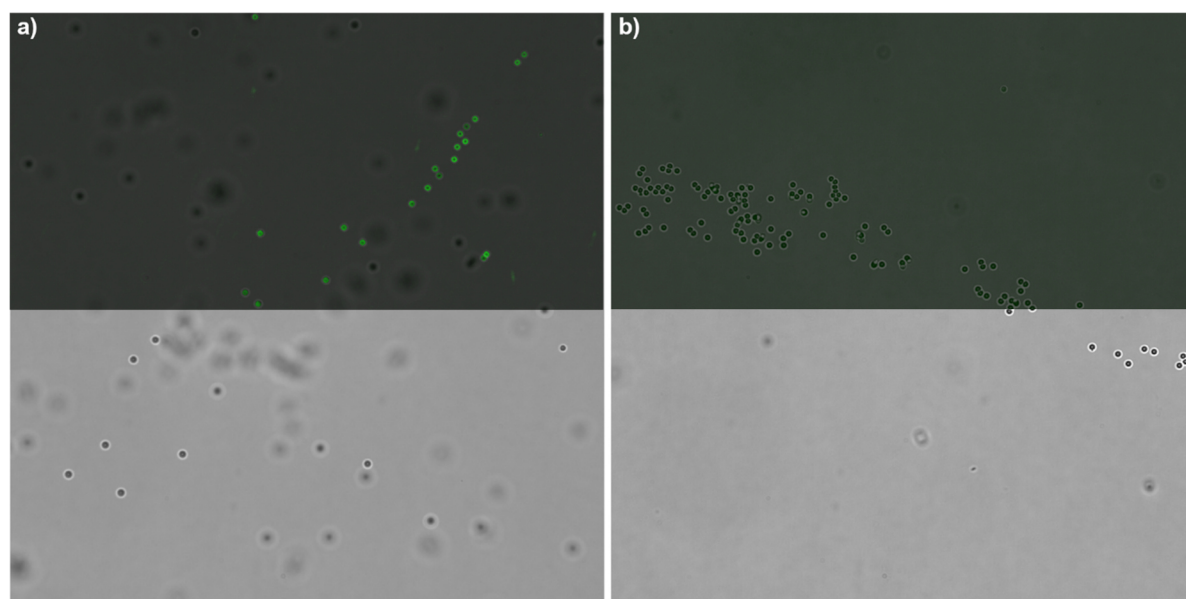
Figure 4-35: Combined microscopy images of LPS-PS microparticles in an aqueous dispersion. The upper half shows the overlay of the bright-field and fluorescence channel (excitation: 470 nm, emission: 519/25 nm bandpass filter) and the lower half only the bright-field. Fluorescence was only visible for S5 (a), whereas microparticles of S0 were only recognizable in bright-field.

4.3.3 Discussion

The proposed mechanism for the LPS-PS microparticles fabricated in this study is schematically presented in Figure 4-36: Proposed swell-capture mechanism to prepare the LPS-PS microparticles in this study. Figure 4-36. First, an aqueous suspension is mixed with an organic solvent such as THF, which can dissolve PS, but in smaller doses causes softening and swelling of the microparticles (Behnke et al., 2010). Next, LPS is added, which was previously extracted from bacteria (in this study, commercially available LPS was used). The hydrophobic lipid A of the LPS is expected to accumulate at the surface of the PS, where the free polymer chains provide permeability to the microparticles. In the final step, the organic solvent is exchanged with water and the microparticles shrink. The lipid A is sucked into the surface, where it "intercalates" with the polymer chains. The rest of the LPS exposes to the surrounding medium.

For the first time, the proposed swell-capture mechanism was applied in this study for the fabrication of LPS-PS microparticles. The success of this method was proven by means of various analyses of the resultant system.

The incorporation of LPS changes the ζ-potential of the microparticle surface. Measurements showed an increase of the ζ-potential with higher LPS concentration. The pure LPS was measured as a reference and yielded higher values than the pure PS microparticles. The results of pure LPS were in agreement

with literature data (Sun et al., 2012). While for the pure PS microparticles, the detailed synthesis route was not known, which defines the ζ-potential (Garcia-Salinas, Romero-Cano and de las Nieves, 2000). The converging zeta potential of increasing LPS content on the microparticles to that of pure LPS is evidence of some kind of LPS accumulation at the microparticle surface.
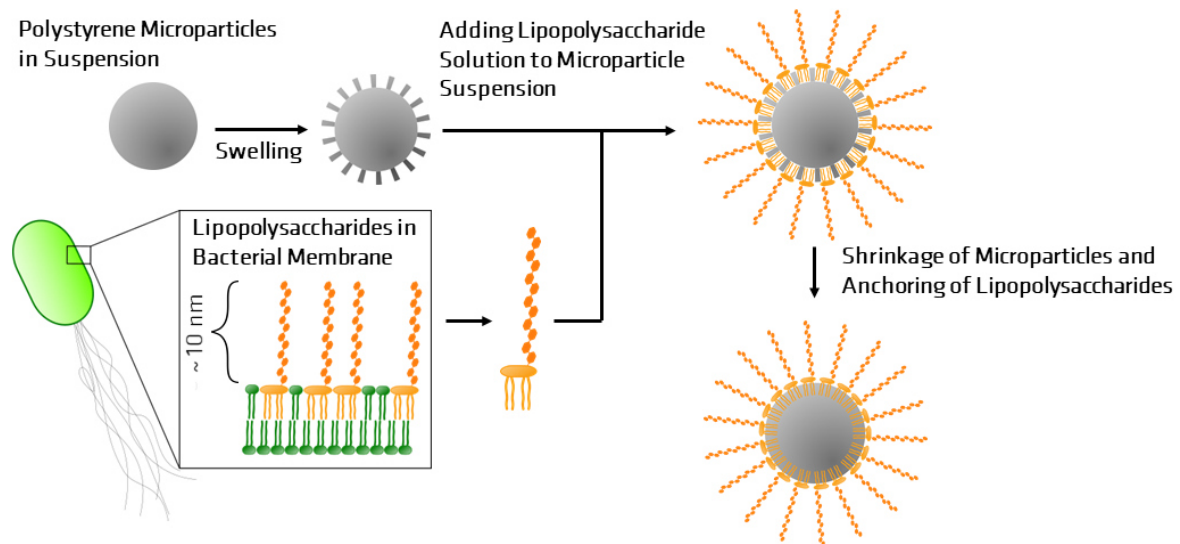
Figure 4-36: Proposed swell-capture mechanism to prepare the LPS-PS microparticles in this study. For illustrative purposes, not to scale.

XPS measurements of the microparticles provide a further indication that LPS has been incorporated. As the amount of LPS in the treatment increased, so did the N content. This characteristic was particularly evident for samples S5 and S6. N is not present in PS but occurs throughout the LPS of *P. aeruginosa*; often as N-acetyl (Knirel et al., 2006). These N-acetyl bonds could also be detected by the fine spectra of the measured elements. Here, N appeared particularly concisely in the form of N-(C*=O)-C. Another marker for LPS would have been phosphate. However, phosphate could not be measured since the P 2p region overlapped with the Si 2p and 2s regions. Silicon originated from the underlying wafer.

In addition to XPS results, a much more detailed insight was possible by AFM-IR analysis. Small areas on the upper part of the microparticle surface could be measured in detail. The spectrum of the LPS-PS microparticles was found to be a combination of that of pure PS microparticles and pure LPS. For both the spectrum of LPS-PS and pure LPS, the amide I and amide II bands were prominent. Furthermore, oxygen-containing groups could be assigned in both spectra. The origin of amide bands might be the N-acetyl bonds, while oxygen originated from carbohydrates (Knirel, 1990; Kiwi and Nadtochenko, 2005).

Trough AFM, the upper curvature surface of individual microparticles could be measured. For this purpose, a method presented by Labuda et al. (2016) was used. The cantilever was excited at higher eigen mode and thus combined with an ultrafine diamond tip, allowed a high resolution of the topography. On the surface of the LPS-PS microparticles, thin threads were visible, which enveloped the underlying microparticle like a yarn ball. They probably originated from the LPS, as they were not found on the pure PS microparticles.

One tool to visualize LPS on the microparticles was staining with FITC. Therefore, after staining the microparticle solution, the particles were intensely washed. Only FITC which tightly bond on the microparticles, stayed. That was the case for the LPS-PS microparticles and the FITC could be visualized with a fluorescence microscope. FITC can form covalent bonds with primary amines (Skelly, Munkenbeck and Morrison, 1979). Such amines are part of substitutes in the core oligosaccharide (Knirel et al., 2006). It has been shown that in addition to detecting LPS, FITC can also be used to visualize the microparticles in the microscope, which may benefit future studies.

In summary, it was shown by various analytical techniques, that LPS can be incorporated on PS microparticles. Incorporation was done by a new, presented swell-capture method.

5   Conclusion and Outlook

In the present project, the direct and indirect influence of nano- and microtopographies on the attachment and retention of *P. fluorescens* SBW25 was investigated. It therefore contributes to the research field of biofilm development of microorganisms. Furthermore, a LPS-PS microparticle system was developed which could mimic bacteria in attachment experiments in the future.

The study of bacterial attachment is presented in Parts I and II.. The first part focuses on the direct effect of a surface with ZnO nanorods and a surface with alternating microareas of ZnO nanorods and ZnO thin film. The second part aims at the influence of micro-hydrodynamics in the vicinity of defined microstructures and represents an indirect effect. For all these substrates, their influence on the initial attachment of bacteria and on the retention of bacteria after high shear stress exposure was investigated. For this purpose, the remaining single cells on the substrates were counted, and the counts were compared statistically with each other. A lower cell count indicates a higher efficiency of a substrate in preventing bacterial attachment and retention.

The attachment of the bacteria in both parts was followed in-situ using a flow chamber. This device and method avoid significant measurement errors, which otherwise occur in ex-situ studies of bacterial attachment. Even though an in-situ method is much more elaborate, it is nevertheless indispensable to gain reliable findings on the attachment of bacteria. Although it has been proven in the past that ex-situ methods are problematic in this field of research, they are still carried out in this way in the majority of studies. The flow chamber for the present project was purposefully developed. It allowed high resolution observation of the bacteria at the upper and lower wall surfaces with fluorescence microscopy.

In the first part, it was found that a lawn of 50—100 diameter closely packed ZnO nanorods did not had a direct effect by reducing the bacterial attachment compared to a smooth ZnO thin film and a glass substrate. The bacterial counts were in the same range for all these substrates. That was also the case for surfaces with arrays of ZnO nanorods. Similarly, the total number of bacteria was not reduced compared to the smooth substrates. Hence, an overall cell-reducing effect of nanotopography and microtopography on *P. fluorescens* attachment must be rejected. However, the bacteria preferentially attached at the 1 μm heigh edges of the nanorod arrays, which was reflected in a higher cell count. Possible reason for the higher bacterial counts at the edges are the increased contact area and protection from the flowing liquid.

In the second part, no reduced attachment due to micro-hydrodynamics at the surface compared to the first part was found either; nor had altered micro-hydrodynamics induced by variation of the microstructures' spacing an attachment reducing effect. Thus, this kind of indirect effect on bacterial adhesion could not be demonstrated. Future studies should aim at modifying microstructures in such a way that surface-repulsing flows exhibit higher forces, resulting in more bacteria being pushed away from the attachment sites.

One reason why no reduction in bacterial numbers was found in either part, even after exposure to higher shear stresses, is very likely the bacterial strain. Bacteria of the species *P. fluorescens* have flagella that act as an anchor and thus fasten the bacterium to the surface upon brief contact with it. Then, other attachment tools of the bacteria, such as pili, can take over and increase the adhesion force. They are followed by bond maturation and EPS production, which leads to irreversibly attached bacteria. These tools are common for bacteria, but what acts like a door opener for the initial contact are presumably the flagella of *P. fluorescens*.

These observations mean serious consequences for further research on surfaces to control bacterial attachment and thus also to counteract biofilm development. In the past, studies did not ascribe significant importance to the influence of the used bacterial species. For example, cocci, which have no flagella and cannot move actively, were often investigated. However, in order to keep a surface free of biofilm and fouling in a natural environment, all microbial species present must be taken into account. Those that can ultimately attach to the surface may also form the basis of a cross-species biofilm. Therefore, this study proposes that future research on surfaces to control bacterial attachment should be directed at those bacteria that can best adhere to the substrate.

For the second part, defined microstructures were created with high reproducibility by MPL. This technique was applied for the first time in the present project to study bacterial attachment. The use of MPL for general microfluidic applications is only scarcely reported in the literature. Therefore, the present project also provides a workflow for using MPL in future work in the aforementioned fields and points out occurring problems and their solutions.

It turned out that the flow in the channels of the flow chamber was not homogeneous, as accompanying CFD simulations predicted. This anomaly resulted in fluctuating bacterial attachment with the consequence of deviating results with high variances. However, a homogenous flow is assumed in other published studies using a flow chamber for bacterial attachment investigations. This phenomenon was noted in the present project because the attached bacteria were mapped with a comparatively large number of images that had not been done before to this extent. The phenomenon that homogeneous flows are predicted by CFD simulations but not reflected in the bacterial

attachment needs further studies. Findings are strongly needed as this topic concerns serious research on bacterial attachment in general.

As a further approach of the present project, an LPS-PS microparticle model system was developed in part III. Therefore, the PS was encapsulated by the LPS with a newly developed swell-capture method. Various analytical techniques were used to detect and confirm the presence of LPS on the microparticles. Thus, many data references for future work are available, which apply analytical techniques for the presented microparticle system. The presented LPS-PS microparticle system was intended as a starting point for studies to mimic bacteria in attachment experiments. Since *P. aeruginosa* serotype O10 LPS was used in this work, appropriate LPS must be extracted for another use.

However, the LPS-PS microparticle application is not limited to bacterial attachment studies. They open up new possibilities in vaccination research. Derivatives of LPS are of great interest as adjuvants for vaccination. Furthermore, the O-antigens presented by LPS play an important role in serological tests. For both fields, the new method now offers a system that is easy to make and very stable due to the anchoring of LPS in the microparticle surface.

6 References

Abdoel, T. H. & Smits, H. L. 2007 'Rapid latex agglutination test for the serodiagnosis of human brucellosis'. *Diagn Microbiol Infect Dis,* 57, 123-8, doi: https://doi.org/10.1016/j.diagmicrobio.2006.08.017

Agriculture and Environment Research Unit 2023 *Zinc oxide* [Online]: University of Hertfordshire, Available: http://sitem.herts.ac.uk/aeru/iupac/Reports/1321.htm [Accessed 02.05. 2023].

Aguayo, S., Donos, N., Spratt, D. & Bozec, L. 2015 'Nanoadhesion of Staphylococcus aureus onto Titanium Implant Surfaces'. *J Dent Res,* 94, 1078-84, doi: https://doi.org/10.1177/0022034515591485

Ahn, C. H., Kim, Y. Y., Kim, D. C., Mohanta, S. K. & Cho, H. K. 2009 'A comparative analysis of deep level emission in ZnO layers deposited by various methods'. *Journal of Applied Physics,* 105, doi: https://doi.org/10.1063/1.3054175

Aksel, N. & Spurk, J. H. 2019, *Fluid Mechanics*, Springer International Publishing.

Aurang, P., Demircioglu, O., Es, F., Turan, R., Unalan, H. E. & Mullins, W. 2013 'ZnO Nanorods as Antireflective Coatings for Industrial-Scale Single-Crystalline Silicon Solar Cells'. *Journal of the American Ceramic Society,* 96, 1253-1257, doi: https://doi.org/10.1111/jace.12200

Ausschuss Für Biologische Arbeitsstoffe 2015 Technische Regeln für Biologische Arbeitsstoffe - Einstufung von Prokaryonten (Bacteria und Archaea) in Risikogruppen, *In:* BUNDESANSTALT FÜR ARBEITSSCHUTZ UND ARBEITSMEDIZIN (ed.) *TRBA 466*.

Bakhchova, L., Jonusauskas, L., Andrijec, D., Kurachkina, M., Baravykas, T., Eremin, A. & Steinmann, U. 2020 'Femtosecond Laser-Based Integration of Nano-Membranes into Organ-on-a-Chip Systems'. *Materials (Basel),* 13, doi: https://doi.org/10.3390/ma13143076

Barata, D., Provaggi, E., Van Blitterswijk, C. & Habibovic, P. 2017 'Development of a microfluidic platform integrating high-resolution microstructured biomaterials to study cell-material interactions'. *Lab Chip,* 17, 4134-4147, doi: https://doi.org/10.1039/c7lc00802c

Baruah, S. & Dutta, J. 2009 'Effect of seeded substrates on hydrothermally grown ZnO nanorods'. *Journal of Sol-Gel Science and Technology,* 50, 456-464, doi: https://doi.org/10.1007/s10971-009-1917-2

Baruah, S., Mahmood, M. A., Myint, M. T., Bora, T. & Dutta, J. 2010 'Enhanced visible light photocatalysis through fast crystallization of zinc oxide nanorods'. *Beilstein J Nanotechnol,* 1, 14-20, doi: https://doi.org/10.3762/bjnano.1.3

Beech, I. B. & Sunner, J. 2004 'Biocorrosion: towards understanding interactions between biofilms and metals'. *Curr Opin Biotechnol,* 15, 181-6, doi: https://doi.org/10.1016/j.copbio.2004.05.001

Behnke, T., Würth, C., Hoffmann, K., Hübner, M., Panne, U. & Resch-Genger, U. 2010 'Encapsulation of Hydrophobic Dyes in Polystyrene Micro- and Nanoparticles via Swelling Procedures'. *Journal of Fluorescence,* 21, 937-944, doi: https://doi.org/10.1007/s10895-010-0632-2

Behnke, T., Würth, C., Laux, E.-M., Hoffmann, K. & Resch-Genger, U. 2012 'Simple strategies towards bright polymer particles via one-step staining procedures'. *Dyes and Pigments,* 94, 247-257, doi: https://doi.org/https://doi.org/10.1016/j.dyepig.2012.01.021

Bekeny, C., Voss, T., Gafsi, H., Gutowski, J., Postels, B., Kreye, M. & Waag, A. 2006 'Origin of the near-band-edge photoluminescence emission in aqueous chemically grown ZnO nanorods'. *Journal of Applied Physics,* 100, doi: https://doi.org/10.1063/1.2390548

Berne, C., Ellison, C. K., Ducret, A. & Brun, Y. V. 2018 'Bacterial adhesion at the single-cell level'. *Nat Rev Microbiol,* 16, 616-627, doi: https://doi.org/10.1038/s41579-018-0057-5

Bhutto, A. A., Vesely, D. & Gabrys, B. J. 2003 'Miscibility and interactions in polystyrene and sodium sulfonated polystyrene with poly(vinyl methyl ether) PVME blends. Part II. FTIR'. *Polymer,* 44, 6627-6631, doi: https://doi.org/10.1016/j.polymer.2003.08.005

Bindels, D. S., Haarbosch, L., Van Weeren, L., Postma, M., Wiese, K. E., Mastop, M., Aumonier, S., Gotthard, G., Royant, A., Hink, M. A. & Gadella, T. W., Jr. 2017 'mScarlet: a bright monomeric red fluorescent protein for cellular imaging'. *Nat Methods,* 14, 53-56, doi: https://doi.org/10.1038/nmeth.4074

Blazevic, D. J., Koepcke, M. H. & Matsen, J. M. 1973 'Incidence and identification of Pseudomonas fluorescens and Pseudomonas putida in the clinical laboratory'. *Appl Microbiol,* 25, 107-10, doi: https://doi.org/10.1128/am.25.1.107-110.1973

Böhmler, J., Haidara, H., Ponche, A. & Ploux, L. 2015 'Impact of Chemical Heterogeneities of Surfaces on Colonization by Bacteria'. *ACS Biomaterials Science & Engineering,* 1, 693-704, doi: https://doi.org/10.1021/acsbiomaterials.5b00151

Bohr, A., Colombo, S. & Jensen, H. 2019 Future of microfluidics in research and in the market. *Microfluidics for Pharmaceutical Applications.*

Boks, N. P., Norde, W., Van Der Mei, H. C. & Busscher, H. J. 2008 'Forces involved in bacterial adhesion to hydrophilic and hydrophobic surfaces'. *Microbiology,* 154, 3122-33, doi: https://doi.org/10.1099/mic.0.2008/018622-0

Bollenl, C. M. L., Lambrechts, P. & Quirynen, M. 1997 'Comparison of surface roughness of oral hard materials to the threshold surface roughness for bacterial plaque retention: A review of the literature'. *Dental Materials,* 13, 258-269, doi: https://doi.org/10.1016/s0109-5641(97)80038-3

Bondarenko, O., Juganson, K., Ivask, A., Kasemets, K., Mortimer, M. & Kahru, A. 2013 'Toxicity of Ag, CuO and ZnO nanoparticles to selected environmentally relevant test organisms and mammalian cells in vitro: a critical review'. *Arch Toxicol,* 87, 1181-200, doi: https://doi.org/10.1007/s00204-013-1079-4

Bos, R., Van Der Mei, H. C. & Busscher, H. J. 1999 'Physico-chemistry of initial microbial adhesive interactions--its mechanisms and methods for study'. *FEMS Microbiol Rev,* 23, 179-230, doi: https://doi.org/10.1111/j.1574-6976.1999.tb00396.x

Bossis, E., Lemanceau, P., Latour, X. & Gardan, L. 2000 'The taxonomy of Pseudomonas fluorescens and Pseudomonas putida: current status and need for revision'. *Agronomie,* 20, 51-63, doi:

Brandenburg, K., Schromm, A. B. & Gutsmann, T. 2010 'Endotoxins: relationship between structure, function, and activity'. *Subcell Biochem,* 53, 53-67, doi: https://doi.org/10.1007/978-90-481-9078-2_3

Brewer, L. R. & Bianco, P. R. 2008 'Laminar flow cells for single-molecule studies of DNA-protein interactions'. *Nat Methods,* 5, 517-25, doi: https://doi.org/10.1038/nmeth.1217

Busscher, H. J., Bos, R. & Van Der Mei, H. C. 1995 'Initial microbial adhesion is a determinant for the strength of biofilm adhesion'. *FEMS Microbiol Lett,* 128, 229-34, doi: https://doi.org/10.1111/j.1574-6968.1995.tb07529.x

Busscher, H. J., Norde, W., Sharma, P. K. & Van Der Mei, H. C. 2010 'Interfacial re-arrangement in initial microbial adhesion to surfaces'. *Current Opinion in Colloid & Interface Science,* 15, 510-517, doi: https://doi.org/10.1016/j.cocis.2010.05.014

Busscher, H. J. & Van Der Mei, H. C. 1995 'Use of Flow Chamber Devices and Image-Analysis Methods to Study Microbial Adhesion'. *Adhesion of Microbial Pathogens,* 253**,** 455-477, doi: https://doi.org/10.1016/S0076-6879(95)53039-8

Busscher, H. J. & Van Der Mei, H. C. 2006 'Microbial adhesion in flow displacement systems'. *Clin Microbiol Rev,* 19**,** 127-41, doi: https://doi.org/10.1128/CMR.19.1.127-141.2006

Camper, A. K., Hayes, J. T., Sturman, P. J., Jones, W. L. & Cunningham, A. B. 1993 'Effects of Motility and Adsorption Rate Coefficient on Transport of Bacteria through Saturated Porous Media'. *Appl Environ Microbiol,* 59**,** 3455-62, doi: https://doi.org/10.1128/aem.59.10.3455-3462.1993

Carniello, V., Peterson, B. W., Van Der Mei, H. C. & Busscher, H. J. 2018 'Physico-chemistry from initial bacterial adhesion to surface-programmed biofilm growth'. *Adv Colloid Interface Sci,* 261**,** 1-14, doi: https://doi.org/10.1016/j.cis.2018.10.005

Caroff, M. & Novikov, A. 2020 'Lipopolysaccharides: structure, function and bacterial identification'. *Ocl,* 27, doi: https://doi.org/10.1051/ocl/2020025

Carroll, D., Holden, N., Gifford, M. L. & Dupuy, L. X. 2020 'Framework for Quantification of the Dynamics of Root Colonization by Pseudomonas fluorescens Isolate SBW25'. *Front Microbiol,* 11**,** 585443, doi: https://doi.org/10.3389/fmicb.2020.585443

Casella, C. R. & Mitchell, T. C. 2008 'Putting endotoxin to work for us: monophosphoryl lipid A as a safe and effective vaccine adjuvant'. *Cell Mol Life Sci,* 65**,** 3231-40, doi: https://doi.org/10.1007/s00018-008-8228-6

Cheng, Y., Feng, G. & Moraru, C. I. 2019 'Micro- and Nanotopography Sensitive Bacterial Attachment Mechanisms: A Review'. *Front Microbiol,* 10**,** 191, doi: https://doi.org/10.3389/fmicb.2019.00191

Choi, C., Song, K. D., Kang, S., Park, J. S. & Choi, W. 2018a 'Optical imaging featuring both long working distance and high spatial resolution by correcting the aberration of a large aperture lens'. *Sci Rep,* 8**,** 9165, doi: https://doi.org/10.1038/s41598-018-27289-1

Choi, D.-C., Jung, S.-Y., Won, Y.-J., Jang, J. H., Lee, J., Chae, H.-R., Ahn, K. H., Lee, S., Park, P.-K. & Lee, C.-H. 2015 'Three-dimensional hydraulic modeling of particle deposition on the patterned isopore membrane in crossflow microfiltration'. *Journal of Membrane Science,* 492**,** 156-163, doi: https://doi.org/10.1016/j.memsci.2015.05.054

Choi, K.-H., Gaynor, J. B., White, K. G., Lopez, C., Bosio, C. M., Karkhoff-Schweizer, R. R. & Schweizer, H. P. 2005 'A Tn7-based broad-range bacterial cloning and expression system'. *Nature Methods,* 2**,** 443, doi: https://doi.org/10.1038/nmeth765

Choi, W., Lee, C., Lee, D., Won, Y. J., Lee, G. W., Shin, M. G., Chun, B., Kim, T.-S., Park, H.-D., Jung, H. W., Lee, J. S. & Lee, J.-H. 2018b 'Sharkskin-mimetic desalination membranes with ultralow biofouling'. *Journal of Materials Chemistry A,* 6**,** 23034-23045, doi: https://doi.org/10.1039/c8ta06125d

Christersson, C. E., Fornalik, M. S., Baier, R. E. & Glantz, P. O. 1987 'In vitro attachment of oral microorganisms to solid surfaces: evaluation of a controlled flow method'. *Scand J Dent Res,* 95**,** 151-8, doi: https://doi.org/10.1111/j.1600-0722.1987.tb01823.x

Conrad, J. C., Gibiansky, M. L., Jin, F., Gordon, V. D., Motto, D. A., Mathewson, M. A., Stopka, W. G., Zelasko, D. C., Shrout, J. D. & Wong, G. C. 2011 'Flagella and pili-mediated near-surface single-cell motility mechanisms in P. aeruginosa'. *Biophys J,* 100**,** 1608-16, doi: https://doi.org/10.1016/j.bpj.2011.02.020

Crawford, R. J., Webb, H. K., Truong, V. K., Hasan, J. & Ivanova, E. P. 2012 'Surface topographical factors influencing bacterial attachment'. *Adv Colloid Interface Sci,* 179-182**,** 142-9, doi: https://doi.org/10.1016/j.cis.2012.06.015

Czyzowska, A. & Barbasz, A. 2020 'A review: zinc oxide nanoparticles - friends or enemies?'. *Int J Environ Health Res*, 1-17, doi: https://doi.org/10.1080/09603123.2020.1805415

David, C. A., Galceran, J., Rey-Castro, C., Puy, J., Companys, E., Salvador, J., Monné, J., Wallace, R. & Vakourov, A. 2012 'Dissolution Kinetics and Solubility of ZnO Nanoparticles Followed by AGNES'. *The Journal of Physical Chemistry C,* 116, 11758-11767, doi: https://doi.org/10.1021/jp301671b

De Carvalho, C. C. C. R. 2018 'Marine Biofilms: A Successful Microbial Strategy With Economic Implications'. *Frontiers in Marine Science,* 5, doi: https://doi.org/10.3389/fmars.2018.00126

Demento, S., Steenblock, E. R. & Fahmy, T. M. 2009 'Biomimetic approaches to modulating the T cell immune response with nano- and micro- particles'. *Annu Int Conf IEEE Eng Med Biol Soc,* 2009, 1161-6, doi: https://doi.org/10.1109/IEMBS.2009.5332625

Deupree, S. M. & Schoenfisch, M. H. 2008 'Quantitative method for determining the lateral strength of bacterial adhesion and application for characterizing adhesion kinetics'. *Langmuir,* 24, 4700-7, doi: https://doi.org/10.1021/la800417g

Díaz, C., Cortizo, M. C., Schilardi, P. L., Saravia, S. G. G. D. & Mele, M. a. F. L. D. 2007 'Influence of the nano-micro structure of the surface on bacterial adhesion'. *Materials Research,* 10, 11-14, doi: https://doi.org/10.1590/s1516-14392007000100004

Djurišić, A. B., Chen, X., Leung, Y. H. & Man Ching Ng, A. 2012 'ZnO nanostructures: growth, properties and applications'. *Journal of Materials Chemistry,* 22, doi: https://doi.org/10.1039/c2jm15548f

Djurišić, A. B., Leung, Y. H., Tam, K. H., Ding, L., Ge, W. K., Chen, H. Y. & Gwo, S. 2006 'Green, yellow, and orange defect emission from ZnO nanostructures: Influence of excitation wavelength'. *Applied Physics Letters,* 88, doi: https://doi.org/10.1063/1.2182096

Dogruoz, N., Goksay, D., Ilhan-Sungur, E. & Cotuk, A. 2009 'Pioneer colonizer microorganisms in biofilm formation on galvanized steel in a simulated recirculating cooling-water system'. *J Basic Microbiol,* 49 Suppl 1, S5-12, doi: https://doi.org/10.1002/jobm.200800250

Donlan, R. M. 2002 'Biofilms: microbial life on surfaces'. *Emerg Infect Dis,* 8, 881-90, doi: https://doi.org/10.3201/eid0809.020063

Duffy, D. C., Mcdonald, J. C., Schueller, O. J. & Whitesides, G. M. 1998 'Rapid Prototyping of Microfluidic Systems in Poly(dimethylsiloxane)'. *Anal Chem,* 70, 4974-84, doi: https://doi.org/10.1021/ac980656z

El-Taboni, F., Caseley, E., Katsikogianni, M., Swanson, L., Swift, T. & Romero-Gonzalez, M. E. 2020 'Fluorescence Spectroscopy Analysis of the Bacteria-Mineral Interface: Adsorption of Lipopolysaccharides to Silica and Alumina'. *Langmuir,* 36, 1623-1632, doi: https://doi.org/10.1021/acs.langmuir.9b02158

Elbourne, A., Coyle, V. E., Truong, V. K., Sabri, Ylias m., Kandjani, A. E., Bhargava, S. K., Ivanova, E. P. & Crawford, R. J. 2019 'Multi-directional electrodeposited gold nanospikes for antibacterial surface applications'. *Nanoscale Advances,* 1, 203-212, doi: https://doi.org/10.1039/c8na00124c

Elimelech, M., Jia, X., Gregory, J. & Williams, R. 1995, *Particle Deposition and Aggregation - Measurement, Modelling and Simulation,* Oxford, Elsevier.

Fang, C. 2019, *An Introduction to Fluid Mechanics,* Cham, Springer International Publishing : Imprint: Springer.

Flemming, H. C. & Wingender, J. 2010 'The biofilm matrix'. *Nat Rev Microbiol,* 8, 623-33, doi: https://doi.org/10.1038/nrmicro2415

Flemming, H. C., Wingender, J., Szewzyk, U., Steinberg, P., Rice, S. A. & Kjelleberg, S. 2016 'Biofilms: an emergent form of bacterial life'. *Nat Rev Microbiol,* 14, 563-75, doi: https://doi.org/10.1038/nrmicro.2016.94

Fomsgaard, A. 1990 'Antibodies to lipopolysaccharides: Some diagnostic and protective aspects'. *Apmis,* 98, 5-38, doi: https://doi.org/10.1111/j.1600-0463.1990.tb05699.x

Fux, C. A., Costerton, J. W., Stewart, P. S. & Stoodley, P. 2005 'Survival strategies of infectious biofilms'. *Trends Microbiol,* 13, 34-40, doi: https://doi.org/10.1016/j.tim.2004.11.010

Gadelmawla, E. S., Koura, M. M., Maksoud, T. M. A., Elewa, I. M. & Soliman, H. H. 2002 'Roughness parameters'. *Journal of Materials Processing Technology,* 123, 133-145, doi: https://doi.org/10.1016/s0924-0136(02)00060-2

Galdamez-Martinez, A., Santana, G., Guell, F., Martinez-Alanis, P. R. & Dutt, A. 2020 'Photoluminescence of ZnO Nanowires: A Review'. *Nanomaterials (Basel),* 10, doi: https://doi.org/10.3390/nano10050857

Gallardo-Moreno, A. M., González-Martín, M. L., Bruque, J. M., Pérez-Giraldo, C. & Gómez-García, A. C. 2002 'Temperature influence on the physicochemical surface properties and adhesion behaviour of Enterococcus faecalis to glass and silicone'. *Journal of Adhesion Science and Technology,* 16, 1215-1223, doi: https://doi.org/10.1163/156856102320256855

Gao, S. Y., Li, H. D., Yuan, J. J., Li, Y. A., Yang, X. X. & Liu, J. W. 2010 'ZnO nanorods/plates on Si substrate grown by low-temperature hydrothermal reaction'. *Applied Surface Science,* 256, 2781-2785, doi: https://doi.org/10.1016/j.apsusc.2009.11.028

Gao, Z., Li, H., Chen, X. & Zhang, H. P. 2015 'Using confined bacteria as building blocks to generate fluid flow'. *Lab Chip,* 15, 4555-62, doi: https://doi.org/10.1039/c5lc01093d

Garcia-Salinas, M. J., Romero-Cano, M. S. & De Las Nieves, F. J. 2000 'Zeta potential study of a polystyrene latex with variable surface charge: influence on the electroviscous coefficient'. *Trends in Colloid and Interface Science Xiv,* 115, 112-116, doi: https://doi.org/10.1007/3-540-46545-6_23

Garrett, T. R., Bhakoo, M. & Zhang, Z. 2008 'Bacterial adhesion and biofilms on surfaces'. *Progress in Natural Science,* 18, 1049-1056, doi: https://doi.org/10.1016/j.pnsc.2008.04.001

Ge, X., Leng, Y., Lu, X., Ren, F., Wang, K., Ding, Y. & Yang, M. 2015 'Bacterial responses to periodic micropillar array'. *J Biomed Mater Res A,* 103, 384-96, doi: https://doi.org/10.1002/jbm.a.35182

Gharpure, S. & Ankamwar, B. 2020 'Synthesis and Antimicrobial Properties of Zinc Oxide Nanoparticles'. *J Nanosci Nanotechnol,* 20, 5977-5996, doi: https://doi.org/10.1166/jnn.2020.18707

Gnauck, A., Lentle, R. G. & Kruger, M. C. 2016 'The Characteristics and Function of Bacterial Lipopolysaccharides and Their Endotoxic Potential in Humans'. *Int Rev Immunol,* 35, 189-218, doi: https://doi.org/10.3109/08830185.2015.1087518

Gomez-Suarez, C., Busscher, H. J. & Van Der Mei, H. C. 2001 'Analysis of bacterial detachment from substratum surfaces by the passage of air-liquid interfaces'. *Appl Environ Microbiol,* 67, 2531-7, doi: https://doi.org/10.1128/AEM.67.6.2531-2537.2001

Gonzalez, G., Roppolo, I., Pirri, C. F. & Chiappone, A. 2022 'Current and emerging trends in polymeric 3D printed microfluidic devices'. *Additive Manufacturing,* 55, doi: https://doi.org/10.1016/j.addma.2022.102867

Graham, M. V., Mosier, A. P., Kiehl, T. R., Kaloyeros, A. E. & Cady, N. C. 2013 'Development of antifouling surfaces to reduce bacterial attachment'. *Soft Matter,* 9, doi: https://doi.org/10.1039/c3sm50584g

Greene, L. E., Law, M., Goldberger, J., Kim, F., Johnson, J. C., Zhang, Y., Saykally, R. J. & Yang, P. 2003 'Low-temperature wafer-scale production of ZnO nanowire arrays'. *Angew Chem Int Ed Engl,* 42, 3031-4, doi: https://doi.org/10.1002/anie.200351461

Halder, P., Hossain, N., Pramanik, B. K. & Bhuiyan, M. A. 2021 'Engineered topographies and hydrodynamics in relation to biofouling control-a review'. *Environ Sci Pollut Res Int,* 28, 40678-40692, doi: https://doi.org/10.1007/s11356-020-10864-3

Halder, P., Nasabi, M., Jayasuriya, N., Shimeta, J., Deighton, M., Bhattacharya, S., Mitchell, A. & Bhuiyan, M. A. 2014 'An assessment of the dynamic stability of microorganisms on patterned surfaces in relation to biofouling control'. *Biofouling,* 30, 695-707, doi: https://doi.org/10.1080/08927014.2014.914177

Halder, P., Nasabi, M., Lopez, F. J. T., Jayasuriya, N., Bhattacharya, S., Deighton, M., Mitchell, A. & Bhuiyan, M. A. 2013 'A novel approach to determine the efficacy of patterned surfaces for biofouling control in relation to its microfluidic environment'. *Biofouling,* 29, 697-713, doi: https://doi.org/10.1080/08927014.2013.800192

Harper, J. C., Brozik, S. M., Brinker, C. J. & Kaehr, B. 2012 'Biocompatible microfabrication of 3D isolation chambers for targeted confinement of individual cells and their progeny'. *Anal Chem,* 84, 8985-9, doi: https://doi.org/10.1021/ac301816c

Hasselmann, N. F. & Horn, W. 2018 'Attachment of microstructures to single bacteria by two-photon patterning of a protein based hydrogel'. *Biomedical Physics & Engineering Express,* 4, doi: https://doi.org/10.1088/2057-1976/aaafb7

Hawi, S., Goel, S., Kumar, V., Pearce, O., Ayre, W. N. & Ivanova, E. P. 2022 'Critical Review of Nanopillar-Based Mechanobactericidal Systems'. *ACS Applied Nano Materials,* 5, 1-17, doi: https://doi.org/10.1021/acsanm.1c03045

Hechemy, K., Stevens, R. W. & Gaafar, H. A. 1976 'Antigen distribution in a latex suspension and its relationship to test sensitivity'. *J Clin Microbiol,* 4, 82-6, doi: https://doi.org/10.1128/jcm.4.1.82-86.1976

Hermansson, M. 1999 'The DLVO theory in microbial adhesion'. *Colloids and Surfaces B-Biointerfaces,* 14, 105-119, doi: https://doi.org/10.1016/S0927-7765(99)00029-6

Herrmann, R., Garcia-Garcia, F. J. & Reller, A. 2014 'Rapid degradation of zinc oxide nanoparticles by phosphate ions'. *Beilstein J Nanotechnol,* 5, 2007-15, doi: https://doi.org/10.3762/bjnano.5.209

Hesse, R. 2018 *Unifit 2018* [Online]: Unifit Scientific Software GmbH, Available: https://www.unifit-software.de [Accessed 01.06. 2023].

Heumann, D. & Roger, T. 2002 'Initial responses to endotoxins and Gram-negative bacteria'. *Clin Chim Acta,* 323, 59-72, doi: https://doi.org/10.1016/s0009-8981(02)00180-8

Hizal, F., Choi, C. H., Busscher, H. J. & Van Der Mei, H. C. 2016 'Staphylococcal Adhesion, Detachment and Transmission on Nanopillared Si Surfaces'. *ACS Appl Mater Interfaces,* 8, 30430-30439, doi: https://doi.org/10.1021/acsami.6b09437

Hizal, F., Zhuk, I., Sukhishvili, S., Busscher, H. J., Van Der Mei, H. C. & Choi, C. H. 2015 'Impact of 3D Hierarchical Nanostructures on the Antibacterial Efficacy of a Bacteria-Triggered Self-Defensive Antibiotic Coating'. *ACS Appl Mater Interfaces,* 7, 20304-13, doi: https://doi.org/10.1021/acsami.5b05947

Hori, K. & Matsumoto, S. 2010 'Bacterial adhesion: From mechanism to control'. *Biochemical Engineering Journal,* 48, 424-434, doi: https://doi.org/10.1016/j.bej.2009.11.014

Hsu, L. C., Fang, J., Borca-Tasciuc, D. A., Worobo, R. W. & Moraru, C. I. 2013 'Effect of micro- and nanoscale topography on the adhesion of bacterial cells to solid surfaces'. *Appl Environ Microbiol,* 79, 2703-12, doi: https://doi.org/10.1128/AEM.03436-12

Huang, M. H., Wu, Y., Feick, H., Tran, N., Weber, E. & Yang, P. 2001 'Catalytic Growth of Zinc Oxide Nanowires by Vapor Transport'. *Advanced Materials,* 13, 113-116, doi: https://doi.org/10.1002/1521-4095(200101)13:2<113::Aid-adma113>3.0.Co;2-h

Huang, Z., Chi-Pong Tsui, G., Deng, Y. & Tang, C.-Y. 2020 'Two-photon polymerization nanolithography technology for fabrication of stimulus-responsive micro/nano-structures for biomedical applications'. *Nanotechnology Reviews,* 9, 1118-1136, doi: https://doi.org/10.1515/ntrev-2020-0073

Ivanova, E. P., Hasan, J., Webb, H. K., Truong, V. K., Watson, G. S., Watson, J. A., Baulin, V. A., Pogodin, S., Wang, J. Y., Tobin, M. J., Lobbe, C. & Crawford, R. J. 2012 'Natural bactericidal surfaces: mechanical rupture of Pseudomonas aeruginosa cells by cicada wings'. *Small,* 8, 2489-94, doi: https://doi.org/10.1002/smll.201200528

Jang, B., Xu, L., Moorthy, M. S., Zhang, W., Zeng, L., Kang, M., Kwak, M., Oh, J. & Jin, J. O. 2017 'Lipopolysaccharide-coated CuS nanoparticles promoted anti-cancer and anti-metastatic effect by immuno-photothermal therapy'. *Oncotarget,* 8, 105584-105595, doi: https://doi.org/10.18632/oncotarget.22331

Jia, R., Unsal, T., Xu, D., Lekbach, Y. & Gu, T. 2019 'Microbiologically influenced corrosion and current mitigation strategies: A state of the art review'. *International Biodeterioration & Biodegradation,* 137, 42-58, doi: https://doi.org/10.1016/j.ibiod.2018.11.007

Jiang, W., Mashayekhi, H. & Xing, B. 2009 'Bacterial toxicity comparison between nano- and micro-scaled oxide particles'. *Environ Pollut,* 157, 1619-25, doi: https://doi.org/10.1016/j.envpol.2008.12.025

Kääriäinen, M. L., Weiss, C. K., Ritz, S., Pütz, S., Cameron, D. C., Mailänder, V. & Landfester, K. 2013 'Zinc release from atomic layer deposited zinc oxide thin films and its antibacterial effect on Escherichia coli'. *Applied Surface Science,* 287, 375-380, doi: https://doi.org/10.1016/j.apsusc.2013.09.162

Kaehr, B. & Shear, J. B. 2009 'High-throughput design of microfluidics based on directed bacterial motility'. *Lab Chip,* 9, 2632-7, doi: https://doi.org/10.1039/b908119d

Kaplan, J. B. 2010 'Biofilm dispersal: mechanisms, clinical implications, and potential therapeutic uses'. *J Dent Res,* 89, 205-18, doi: https://doi.org/10.1177/0022034509359403

Katsikogianni, M. G. & Missirlis, Y. F. 2010 'Interactions of bacteria with specific biomaterial surface chemistries under flow conditions'. *Acta Biomater,* 6, 1107-18, doi: https://doi.org/10.1016/j.actbio.2009.08.006

Kazzaz, J., Singh, M., Ugozzoli, M., Chesko, J., Soenawan, E. & O'hagan, D. T. 2006 'Encapsulation of the immune potentiators MPL and RC529 in PLG microparticles enhances their potency'. *J Control Release,* 110, 566-73, doi: https://doi.org/10.1016/j.jconrel.2005.10.010

Kim, J., Park, H. D. & Chung, S. 2012 'Microfluidic approaches to bacterial biofilm formation'. *Molecules,* 17, 9818-34, doi: https://doi.org/10.3390/molecules17089818

Kimkes, T. E. P. & Heinemann, M. 2020 'How bacteria recognise and respond to surface contact'. *FEMS Microbiol Rev,* 44, 106-122, doi: https://doi.org/10.1093/femsre/fuz029

Kives, J., Orgaz, B. & Sanjose, C. 2006 'Polysaccharide differences between planktonic and biofilm-associated EPS from Pseudomonas fluorescens B52'. *Colloids Surf B Biointerfaces,* 52, 123-7, doi: https://doi.org/10.1016/j.colsurfb.2006.04.018

Kiwi, J. & Nadtochenko, V. 2005 'Evidence for the mechanism of photocatalytic degradation of the bacterial wall membrane at the TiO2 interface by ATR-FTIR and laser kinetic spectroscopy'. *Langmuir,* 21, 4631-41, doi: https://doi.org/10.1021/la046983l

Klemm, P. & Schembri, M. A. 2000 'Bacterial adhesins: function and structure'. *International Journal of Medical Microbiology,* 290, 27-35, doi: https://doi.org/10.1016/s1438-4221(00)80102-2

Knirel, Y. A. 1990 'Polysaccharide antigens of Pseudomonas aeruginosa'. *Crit Rev Microbiol,* 17, 273-304, doi: https://doi.org/10.3109/10408419009105729

Knirel, Y. A., Bystrova, O. V., Kocharova, N. A., Zahringer, U. & Pier, G. B. 2006 'Conserved and variable structural features in the lipopolysaccharide of Pseudomonas aeruginosa'. *J Endotoxin Res,* 12, 324-36, doi: https://doi.org/10.1179/096805106X118906

Koch, B., Jensen, L. E. & Nybroe, O. 2001 'A panel of Tn7-based vectors for insertion of the gfp marker gene or for delivery of cloned DNA into Gram-negative bacteria at a neutral chromosomal site'. *Journal of Microbiological Methods,* 45, 187-195, doi: https://doi.org/10.1016/s0167-7012(01)00246-9

Kolodziejczak-Radzimska, A. & Jesionowski, T. 2014 'Zinc Oxide-From Synthesis to Application: A Review'. *Materials (Basel),* 7, 2833-2881, doi: https://doi.org/10.3390/ma7042833

Koo, H., Allan, R. N., Howlin, R. P., Stoodley, P. & Hall-Stoodley, L. 2017 'Targeting microbial biofilms: current and prospective therapeutic strategies'. *Nat Rev Microbiol,* 15, 740-755, doi: https://doi.org/10.1038/nrmicro.2017.99

Korber, D. R., Lawrence, J. R. & Caldwell, D. E. 1994 'Effect of Motility on Surface Colonization and Reproductive Success of Pseudomonas fluorescens in Dual-Dilution Continuous Culture and Batch Culture Systems'. *Appl Environ Microbiol,* 60, 1421-9, doi: https://doi.org/10.1128/aem.60.5.1421-1429.1994

Krsmanovic, M., Biswas, D., Ali, H., Kumar, A., Ghosh, R. & Dickerson, A. K. 2021 'Hydrodynamics and surface properties influence biofilm proliferation'. *Adv Colloid Interface Sci,* 288, 102336, doi: https://doi.org/10.1016/j.cis.2020.102336

Kumar, A., Karig, D., Acharya, R., Neethirajan, S., Mukherjee, P. P., Retterer, S. & Doktycz, M. J. 2012 'Microscale confinement features can affect biofilm formation'. *Microfluidics and Nanofluidics,* 14, 895-902, doi: https://doi.org/10.1007/s10404-012-1120-6

Labuda, A., Kocun, M., Lysy, M., Walsh, T., Meinhold, J., Proksch, T., Meinhold, W., Anderson, C. & Proksch, R. 2016 'Calibration of higher eigenmodes of cantilevers'. *Rev Sci Instrum,* 87, 073705, doi: https://doi.org/10.1063/1.4955122

Lam, J. S., Taylor, V. L., Islam, S. T., Hao, Y. & Kocincova, D. 2011 'Genetic and Functional Diversity of Pseudomonas aeruginosa Lipopolysaccharide'. *Front Microbiol,* 2, 118, doi: https://doi.org/10.3389/fmicb.2011.00118

Landau, L. D. & Lifshitz, E. M. 1987 Ideal Fluids. *Fluid Mechanics.*

Lee, Y.-J., Sounart, T. L., Scrymgeour, D. A., Voigt, J. A. & Hsu, J. W. P. 2007 'Control of ZnO nanorod array alignment synthesized via seeded solution growth'. *Journal of Crystal Growth,* 304, 80-85, doi: https://doi.org/10.1016/j.jcrysgro.2007.02.011

Lee, Y. K., Won, Y.-J., Yoo, J. H., Ahn, K. H. & Lee, C.-H. 2013 'Flow analysis and fouling on the patterned membrane surface'. *Journal of Membrane Science,* 427, 320-325, doi: https://doi.org/10.1016/j.memsci.2012.10.010

Lei, L., Chen, J., Liao, W. & Liu, P. 2020 'Determining the Different Mechanisms Used by Pseudomonas Species to Cope With Minimal Inhibitory Concentrations of Zinc via Comparative Transcriptomic Analyses'. *Front Microbiol,* 11, 573857, doi: https://doi.org/10.3389/fmicb.2020.573857

Li, J., Busscher, H. J., Swartjes, J. J., Chen, Y., Harapanahalli, A. K., Norde, W., Van Der Mei, H. C. & Sjollema, J. 2014 'Residence-time dependent cell wall deformation of different Staphylococcus aureus strains on gold measured using surface-enhanced-fluorescence'. *Soft Matter,* 10, 7638-46, doi: https://doi.org/10.1039/c4sm00584h

Li, J., Busscher, H. J., Van Der Mei, H. C., Norde, W., Krom, B. P. & Sjollema, J. 2011 'Analysis of the contribution of sedimentation to bacterial mass transport in a parallel plate flow chamber: part II: use of fluorescence imaging'. *Colloids Surf B Biointerfaces,* 87, 427-32, doi: https://doi.org/10.1016/j.colsurfb.2011.06.002

Li, J., Srinivasan, S., He, G. N., Kang, J. Y., Wu, S. T. & Ponce, F. A. 2008 'Synthesis and luminescence properties of ZnO nanostructures produced by the sol–gel method'. *Journal of Crystal Growth,* 310, 599-603, doi: https://doi.org/10.1016/j.jcrysgro.2007.11.054

Li, W., Thian, E. S., Wang, M., Wang, Z. & Ren, L. 2021 'Surface Design for Antibacterial Materials: From Fundamentals to Advanced Strategies'. *Adv Sci (Weinh),* 8, e2100368, doi: https://doi.org/10.1002/advs.202100368

Lin, C.-F., Lin, C.-K., Liu, Y.-J., Chiang, C.-H., Pan, M.-J., Baldeck, P. P. & Lin, C.-L. 2014 'Laser-induced cross-linking GFP-AcmA' bioprobe for screening Gram-positive bacteria on a biochip'. *RSC Adv.,* 4, 62882-62887, doi: https://doi.org/10.1039/c4ra12600a

Lin, N., Valiei, A., Mckay, G., Nguyen, D., Tufenkji, N. & Moraes, C. 2022 'Microfluidic Study of Bacterial Attachment on and Detachment from Zinc Oxide Nanopillars'. *ACS Biomater Sci Eng,* 8, 3122-3131, doi: https://doi.org/10.1021/acsbiomaterials.2c00233

Ling, J. F., Graham, M. V. & Cady, N. C. 2012 'EFFECT OF TOPOGRAPHICALLY PATTERNED POLY(DIMETHYLSILOXANE) SURFACES ON Pseudomonas aeruginosa ADHESION AND BIOFILM FORMATION'. *Nano LIFE,* 02, doi: https://doi.org/10.1142/s1793984412420044

Linklater, D. P., Baulin, V. A., Juodkazis, S., Crawford, R. J., Stoodley, P. & Ivanova, E. P. 2021 'Mechano-bactericidal actions of nanostructured surfaces'. *Nat Rev Microbiol,* 19, 8-22, doi: https://doi.org/10.1038/s41579-020-0414-z

Liu, J., Huang, X., Li, Y., Sulieman, K. M., Sun, F. & He, X. 2006 'Selective growth and properties of zinc oxide nanostructures'. *Scripta Materialia,* 55, 795-798, doi: https://doi.org/10.1016/j.scriptamat.2006.07.010

Liu, Z., E, L., Ya, J. & Xin, Y. 2009 'Growth of ZnO nanorods by aqueous solution method with electrodeposited ZnO seed layers'. *Applied Surface Science,* 255, 6415-6420, doi: https://doi.org/10.1016/j.apsusc.2009.02.030

Luan, Y., Liu, S., Pihl, M., Van Der Mei, H. C., Liu, J., Hizal, F., Choi, C.-H., Chen, H., Ren, Y. & Busscher, H. J. 2018 'Bacterial interactions with nanostructured surfaces'. *Current Opinion in Colloid & Interface Science,* 38, 170-189, doi: https://doi.org/10.1016/j.cocis.2018.10.007

Macková, A., Malinský, P., Jagerová, A., Mikšová, R., Lalik, O., Nekvindová, P., Mistrík, J., Marvan, P., Sofer, Z., Holý, V., Schutter, J. D., Kentsch, U., Azarov, A. & Galeckas, A. 2022 'Energetic Au ion beam implantation of ZnO nanopillars for optical response modulation'. *Journal of Physics D: Applied Physics,* 55, doi: https://doi.org/10.1088/1361-6463/ac5486

Makarona, E., Peter, B., Szekacs, I., Tsamis, C. & Horvath, R. 2016 'ZnO Nanostructure Templates as a Cost-Efficient Mass-Producible Route for the Development of Cellular Networks'. *Materials (Basel),* 9, doi: https://doi.org/10.3390/ma9040256

Malinauskas, M., Zukauskas, A., Hasegawa, S., Hayasaki, Y., Mizeikis, V., Buividas, R. & Juodkazis, S. 2016 'Ultrafast laser processing of materials: from science to industry'. *Light Sci Appl,* 5, e16133, doi: https://doi.org/10.1038/lsa.2016.133

Margalit, E., Leshansky, A. & Freger, V. 2013 'Modeling and analysis of hydrodynamic and physico-chemical effects in bacterial deposition on surfaces'. *Biofouling,* 29, 977-89, doi: https://doi.org/10.1080/08927014.2013.823483

Mcclaine, J. W. & Ford, R. M. 2002 'Characterizing the adhesion of motile and nonmotile Escherichia coli to a glass surface using a parallel-plate flow chamber'. *Biotechnol Bioeng,* 78, 179-89, doi: https://doi.org/10.1002/bit.10192

Mcdonald, J. C., Duffy, D. C., Anderson, J. R., Chiu, D. T., Wu, H., Schueller, O. J. A. & Whitesides, G. M. 2000 'Fabrication of microfluidic systems in poly(dimethylsiloxane)'. *Electrophoresis,* 21, 27-40, doi: https://doi.org/10.1002/(sici)1522-2683(20000101)21:1<27::Aid-elps27>3.0.Co;2-c

Mceldowney, S. 1994 'Effect of cadmium and zinc on attachment and detachment interactions of Pseudomonas fluorescens H2 with glass'. *Applied and Environmental Microbiology,* 60, 2759-2765, doi: https://doi.org/10.1128/AEM.60.8.2759-2765.1994

Meinders, J. M., Van Der Mei, H. C. & Busscher, H. J. 1995 'Deposition Efficiency and Reversibility of Bacterial Adhesion under Flow'. *Journal of Colloid and Interface Science,* 176, 329-341, doi: https://doi.org/10.1006/jcis.1995.9960

Meißner, T., Oelschlägel, K. & Potthoff, A. 2014 'Implications of the stability behavior of zinc oxide nanoparticles for toxicological studies'. *International Nano Letters,* 4, doi: https://doi.org/10.1007/s40089-014-0116-5

Mercier-Bonin, M., Adoue, M., Zanna, S., Marcus, P., Combes, D. & Schmitz, P. 2009 'Evaluation of adhesion force between functionalized microbeads and protein-coated stainless steel using shear-flow-induced detachment'. *J Colloid Interface Sci,* 338, 73-81, doi: https://doi.org/10.1016/j.jcis.2009.06.019

Meyer, J. M. & Abdallah, M. A. 1978 'The Fluorescent Pigment of Pseudomonas fluorescens: Biosynthesis, Purification and Physicochemical Properties'. *Journal of General Microbiology,* 107, 319-328, doi: https://doi.org/10.1099/00221287-107-2-319

Moezzi, A., Mcdonagh, A. M. & Cortie, M. B. 2012 'Zinc oxide particles: Synthesis, properties and applications'. *Chemical Engineering Journal,* 185-186, 1-22, doi: https://doi.org/10.1016/j.cej.2012.01.076

Mory, M. 2013, *Fluid mechanics for chemical engineering,* London Hoboken, N.J, Wiley.

Mostoni, Milana, Credico, D'arienzo & Scotti 2019 'Zinc-Based Curing Activators: New Trends for Reducing Zinc Content in Rubber Vulcanization Process'. *Catalysts,* 9, doi: https://doi.org/10.3390/catal9080664

Mueller, R. F., Characklis, W. G., Jones, W. L. & Sears, J. T. 1992 'Characterization of initial events in bacterial surface colonization by two Pseudomonas species using image analysis'. *Biotechnol Bioeng,* 39, 1161-70, doi: https://doi.org/10.1002/bit.260391113

Naderi, A., Bhattacharjee, N. & Folch, A. 2019 'Digital Manufacturing for Microfluidics'. *Annu Rev Biomed Eng,* 21, 325-364, doi: https://doi.org/10.1146/annurev-bioeng-092618-020341

National Institute for Occupational Safety and Health 2021 *Zinc oxide* [Online], Available: https://www.cdc.gov/niosh/npg/npgd0675.html [Accessed 13.09.2021].

Naumann, D., Schultz, C., Sabisch, A., Kastowsky, M. & Labischinski, H. 1989 'New insights into the phase behaviour of a complex anionic amphiphile: architecture and dynamics of bacterial deep rough lipopolysaccharide membranes as seen by FTIR, X-ray, and molecular modelling techniques'. *Journal of Molecular Structure,* 214, 213-246, doi: https://doi.org/10.1016/0022-2860(89)80015-8

Ng, H. T., Chen, B., Li, J., Han, J., Meyyappan, M., Wu, J., Li, S. X. & Haller, E. E. 2003 'Optical properties of single-crystalline ZnO nanowires on m-sapphire'. *Applied Physics Letters,* 82, 2023-2025, doi: https://doi.org/10.1063/1.1564870

O'toole, G., Kaplan, H. B. & Kolter, R. 2000 'Biofilm formation as microbial development'. *Annu Rev Microbiol,* 54, 49-79, doi: https://doi.org/10.1146/annurev.micro.54.1.49

Owens, N. F., Gingell, D. & Rutter, P. R. 1987 'Inhibition of Cell-Adhesion by a Synthetic-Polymer Adsorbed to Glass Shown under Defined Hydrodynamic Stress'. *Journal of Cell Science,* 87, 667-675, doi:

Pan, Z. W., Dai, Z. R. & Wang, Z. L. 2001 'Nanobelts of semiconducting oxides'. *Science,* 291, 1947-9, doi: https://doi.org/10.1126/science.1058120

Pearton, S. J., Norton, D. P., Ip, K., Heo, Y. W. & Steiner, T. 2003 'Recent progress in processing and properties of ZnO'. *Superlattices and Microstructures,* 34, 3-32, doi: https://doi.org/10.1016/s0749-6036(03)00093-4

Pentz, J. T. & Lind, P. A. 2021 'Forecasting of phenotypic and genetic outcomes of experimental evolution in Pseudomonas protegens'. *PLoS Genet,* 17, e1009722, doi: https://doi.org/10.1371/journal.pgen.1009722

Perera-Costa, D., Bruque, J. M., Gonzalez-Martin, M. L., Gomez-Garcia, A. C. & Vadillo-Rodriguez, V. 2014 'Studying the influence of surface topography on bacterial adhesion using spatially organized microtopographic surface patterns'. *Langmuir,* 30, 4633-41, doi: https://doi.org/10.1021/la5001057

Petronis, S., Berntsson, K., Gold, J. & Gatenholm, P. 2000 'Design and microstructuring of PDMS surfaces for improved marine biofouling resistance'. *J Biomater Sci Polym Ed,* 11, 1051-72, doi: https://doi.org/10.1163/156856200743571

Peula-Garcia, J. M., Molina-Bolivar, J. A., Velasco, J., Rojas, A. & Galisteo-Gonzalez, F. 2002 'Interaction of bacterial endotoxine (lipopolysaccharide) with latex particles: application to latex agglutination immunoassays'. *J Colloid Interface Sci,* 245, 230-6, doi: https://doi.org/10.1006/jcis.2001.7958

Piazza, M., Colombo, M., Zanoni, I., Granucci, F., Tortora, P., Weiss, J., Gioannini, T., Prosperi, D. & Peri, F. 2011 'Uniform lipopolysaccharide (LPS)-loaded magnetic nanoparticles for the investigation of LPS-TLR4 signaling'. *Angew Chem Int Ed Engl,* 50, 622-6, doi: https://doi.org/10.1002/anie.201004655

Ping, L., Birkenbeil, J. & Monajembashi, S. 2013 'Swimming behavior of the monotrichous bacterium Pseudomonas fluorescens SBW25'. *FEMS Microbiol Ecol,* 86, 36-44, doi: https://doi.org/10.1111/1574-6941.12076

Pousti, M., Zarabadi, M. P., Abbaszadeh Amirdehi, M., Paquet-Mercier, F. & Greener, J. 2018 'Microfluidic bioanalytical flow cells for biofilm studies: a review'. *Analyst,* 144, 68-86, doi: https://doi.org/10.1039/c8an01526k

Prasad, P., Sachan, S., Suman, S., Swayambhu, G. & Gupta, S. 2018 'Regenerative Core-Shell Nanoparticles for Simultaneous Removal and Detection of Endotoxins'. *Langmuir,* 34, 7396-7403, doi: https://doi.org/10.1021/acs.langmuir.8b00978

Rainey, P. B. & Bailey, M. J. 1996 'Physical and genetic map of the Pseudomonas fluorescens SBW25 chromosome'. *Molecular Microbiology,* 19, 521-533, doi: https://doi.org/10.1046/j.1365-2958.1996.391926.x

Rath, H., Stumpp, S. N. & Stiesch, M. 2017 'Development of a flow chamber system for the reproducible in vitro analysis of biofilm formation on implant materials'. *PLoS One,* 12, e0172095, doi: https://doi.org/10.1371/journal.pone.0172095

Rather, M. A., Gupta, K., Bardhan, P., Borah, M., Sarkar, A., Eldiehy, K. S. H., Bhuyan, S. & Mandal, M. 2021 'Microbial biofilm: A matter of grave concern for human health and food industry'. *J Basic Microbiol,* 61, 380-395, doi: https://doi.org/10.1002/jobm.202000678

Redondo-Nieto, M., Barret, M., Morrissey, J., Germaine, K., Martinez-Granero, F., Barahona, E., Navazo, A., Sanchez-Contreras, M., Moynihan, J. A., Muriel, C., Dowling, D., O'gara, F., Martin, M. & Rivilla, R. 2013 'Genome sequence reveals that Pseudomonas fluorescens F113 possesses a large and diverse array of systems for rhizosphere function and host interaction'. *Bmc Genomics,* 14, doi: https://doi.org/10.1186/1471-2164-14-54

Reed, R. B., Ladner, D. A., Higgins, C. P., Westerhoff, P. & Ranville, J. F. 2012 'Solubility of nano-zinc oxide in environmentally and biologically important matrices'. *Environ Toxicol Chem,* 31, 93-9, doi: https://doi.org/10.1002/etc.708

Rhodes, M. E. 1959 'The Characterization of Pseudomonas fluorescens'. *Journal of General Microbiology,* 21, 221-263, doi: https://doi.org/10.1099/00221287-21-1-221

Richardson, J. J. & Lange, F. F. 2009 'Controlling Low Temperature Aqueous Synthesis of ZnO. 1. Thermodynamic Analysis'. *Crystal Growth & Design,* 9, 2570-2575, doi: https://doi.org/10.1021/cg900082u

Rietschel, E. T., Kirikae, T., Schade, F. U., Mamat, U., Schmidt, G., Loppnow, H., Ulmer, A. J., Zähringer, U., Seydel, U., Di Padova, F., Schreier, M. & Brade, H. 1994 'Bacterial endotoxin: molecular relationships of structure to activity and function'. *The FASEB Journal,* 8, 217-225, doi: https://doi.org/https://doi.org/10.1096/fasebj.8.2.8119492

Rijnaarts, H. H. M., Norde, W., Lyklema, J. & Zehnder, A. J. B. 1999 'DLVO and steric contributions to bacterial deposition in media of different ionic strengths'. *Colloids and Surfaces B: Biointerfaces,* 14, 179-195, doi: https://doi.org/10.1016/s0927-7765(99)00035-1

Romling, U. & Balsalobre, C. 2012 'Biofilm infections, their resilience to therapy and innovative treatment strategies'. *J Intern Med,* 272, 541-61, doi: https://doi.org/10.1111/joim.12004

Rutter, P. & Leech, R. 1980 'The deposition of Streptococcus sanguis NCTC 7868 from a flowing suspension'. *J Gen Microbiol,* 120, 301-7, doi: https://doi.org/10.1099/00221287-120-2-301

Saier, M. H. 2019 Bacterial and Archaeal Cell Membranes. *Reference Module in Life Sciences.*

Santore, M. M. 2022 'Interplay of physico-chemical and mechanical bacteria-surface interactions with transport processes controls early biofilm growth: A review'. *Adv Colloid Interface Sci,* 304, 102665, doi: https://doi.org/10.1016/j.cis.2022.102665

Scales, B. S., Dickson, R. P., Lipuma, J. J. & Huffnagle, G. B. 2014 'Microbiology, genomics, and clinical significance of the Pseudomonas fluorescens species complex, an unappreciated colonizer of humans'. *Clin Microbiol Rev,* 27, 927-48, doi: https://doi.org/10.1128/CMR.00044-14

Scheuerman, T. R., Camper, A. K. & Hamilton, M. A. 1998 'Effects of Substratum Topography on Bacterial Adhesion'. *J Colloid Interface Sci,* 208, 23-33, doi: https://doi.org/10.1006/jcis.1998.5717

Schippers, A., Hedrich, S., Vasters, J., Drobe, M., Sand, W. & Willscher, S. 2014 'Biomining: metal recovery from ores with microorganisms'. *Adv Biochem Eng Biotechnol,* 141, 1-47, doi: https://doi.org/10.1007/10_2013_216

Schumacher, J. F., Long, C. J., Callow, M. E., Finlay, J. A., Callow, J. A. & Brennan, A. B. 2008 'Engineered nanoforce gradients for inhibition of settlement (attachment) of swimming algal spores'. *Langmuir,* 24, 4931-7, doi: https://doi.org/10.1021/la703421v

Selimis, A., Mironov, V. & Farsari, M. 2015 'Direct laser writing: Principles and materials for scaffold 3D printing'. *Microelectronic Engineering,* 132, 83-89, doi: https://doi.org/10.1016/j.mee.2014.10.001

Senevirathne, S. W. M. a. I., Hasan, J., Mathew, A., Woodruff, M. & Yarlagadda, P. K. D. V. 2021 'Bactericidal efficiency of micro- and nanostructured surfaces: a critical perspective'. *RSC Advances,* 11, 1883-1900, doi: https://doi.org/10.1039/d0ra08878a

Sharma, D., Misba, L. & Khan, A. U. 2019 'Antibiotics versus biofilm: an emerging battleground in microbial communities'. *Antimicrob Resist Infect Control,* 8, 76, doi: https://doi.org/10.1186/s13756-019-0533-3

Sharma, S. & Conrad, J. C. 2014 'Attachment from flow of Escherichia coli bacteria onto silanized glass substrates'. *Langmuir,* 30, 11147-55, doi: https://doi.org/10.1021/la502313y

Sheng, X., Ting, Y. P. & Pehkonen, S. O. 2008 'The influence of ionic strength, nutrients and pH on bacterial adhesion to metals'. *J Colloid Interface Sci,* 321, 256-64, doi: https://doi.org/10.1016/j.jcis.2008.02.038

Shurbaji, S., Al-Ruweidi, M., Ali, F. H., Benslimane, F. M. & Yalcin, H. C. 2020 'Application of a Flow-Induced Stress Wave and Investigation of Associated Injuries on Cell Monolayers Using a Parallel Plate Flow Chamber'. *Methods Protoc,* 3, doi: https://doi.org/10.3390/mps3040065

Simões, M., Simões, L. C. & Vieira, M. J. 2010 'A review of current and emergent biofilm control strategies'. *LWT - Food Science and Technology,* 43, 573-583, doi: https://doi.org/10.1016/j.lwt.2009.12.008

Sjollema, J., Busscher, H. J. & Weerkamp, A. H. 1988 'Deposition of oral streptococci and polystyrene latices onto glass in a parallel plate flow cell'. *Biofouling,* 1, 101-112, doi: https://doi.org/10.1080/08927018809378100

Sjollema, J., Busscher, H. J. & Weerkamp, A. H. 1989 'Real-time enumeration of adhering microorganisms in a parallel plate flow cell using automated image analysis'. *Journal of Microbiological Methods,* 9, 73-78, doi: https://doi.org/10.1016/0167-7012(89)90057-2

Skelly, R. R., Munkenbeck, P. & Morrison, D. C. 1979 'Stimulation of T-independent antibody responses by hapten-lipopolysaccharides without repeating polymeric structure'. *Infect Immun,* 23, 287-93, doi: https://doi.org/10.1128/iai.23.2.287-293.1979

Song, J. & Lim, S. 2007 'Effect of Seed Layer on the Growth of ZnO Nanorods'. *The Journal of Physical Chemistry C,* 111, 596-600, doi: https://doi.org/10.1021/jp0655017

Spark, A. J., Law, D. W., Ward, L. P., Cole, I. S. & Best, A. S. 2017 'Effect of Pseudomonas fluorescens on Buried Steel Pipeline Corrosion'. *Environmental Science & Technology,* 51, 8501-8509, doi: https://doi.org/10.1021/acs.est.7b00437

Sperandeo, P., Martorana, A. M. & Polissi, A. 2019 Lipopolysaccharide Biosynthesis and Transport to the Outer Membrane of Gram-Negative Bacteria. *In:* KUHN, A. (ed.) *Bacterial Cell Walls and Membranes.* Cham: Springer International Publishing.

Squires, T. M. & Quake, S. R. 2005 'Microfluidics: Fluid physics at the nanoliter scale'. *Reviews of Modern Physics,* 77, 977-1026, doi: https://doi.org/10.1103/RevModPhys.77.977

Stoodley, P. & Warwood, B. K. 2003 Use of flow cells and annular reactors to study biofilms. *In:* LENS, P., O'FLAHERTY, V., MORAN, A., STOODLEY, P. & MAHONY, T. (eds.) *Biofilms in Industry, Medicine and Environmental Biotechnology.* IWA Publishing.

Sugioka, K. & Cheng, Y. 2014 'Femtosecond laser three-dimensional micro- and nanofabrication'. *Applied Physics Reviews,* 1, doi: https://doi.org/10.1063/1.4904320

Sun, J., Ge, J., Liu, W., Wang, X., Fan, Z., Zhao, W., Zhang, H., Wang, P. & Lee, S.-T. 2012 'A facile assay for direct colorimetric visualization of lipopolysaccharides at low nanomolar level'. *Nano Research,* 5, 486-493, doi: https://doi.org/10.1007/s12274-012-0234-1

Thompson, I. P., Lilley, A. K., Ellis, R. J., Bramwell, P. A. & Bailey, M. J. 1995 'Survival, Colonization and Dispersal of Genetically-Modified Pseudomonas-Fluorescens Sbw25 in the Phytosphere of Field-Grown Sugar-Beet'. *Bio-Technology,* 13, 1493-1497, doi: https://doi.org/10.1038/nbt1295-1493

Tu, J., Yeoh, G. H. & Liu, C. 2018, *Computational Fluid Dynamics - A Practical Approach (3rd Edition),* Saint Louis, Elsevier.

Upadhyay, A. & Srivastava, S. 2014 'Mechanism of zinc resistance in a plant growth promoting Pseudomonas fluorescens strain'. *World J Microbiol Biotechnol,* 30, 2273-82, doi: https://doi.org/10.1007/s11274-014-1648-6

Valiei, A., Kumar, A., Mukherjee, P. P., Liu, Y. & Thundat, T. 2012 'A web of streamers: biofilm formation in a porous microfluidic device'. *Lab Chip,* 12, 5133-7, doi: https://doi.org/10.1039/c2lc40815e

Valiei, A., Lin, N., Mckay, G., Nguyen, D., Moraes, C., Hill, R. J. & Tufenkji, N. 2022 'Surface Wettability Is a Key Feature in the Mechano-Bactericidal Activity of Nanopillars'. *ACS Appl Mater Interfaces,* 14, 27564-27574, doi: https://doi.org/10.1021/acsami.2c03258

Van Beelen, P. & Fleuren-Kemilä, A. K. 1997 'Influence of pH on the toxic effects of zinc, cadmium, and pentachlorophenol on pure cultures of soil microorganisms'. *Environmental Toxicology and Chemistry,* 16, 146-153, doi: https://doi.org/10.1002/etc.5620160208

Van Oss, C. J. 1989 'Energetics of cell-cell and cell-biopolymer interactions'. *Cell Biophys,* 14, 1-16, doi: https://doi.org/10.1007/bf02797387

Van Oss, C. J. 1993 'Acid—base interfacial interactions in aqueous media'. *Colloids and Surfaces A: Physicochemical and Engineering Aspects,* 78, 1-49, doi: https://doi.org/10.1016/0927-7757(93)80308-2

Vayssieres, L. 2003 'Growth of Arrayed Nanorods and Nanowires of ZnO from Aqueous Solutions'. *Advanced Materials,* 15, 464-466, doi: https://doi.org/10.1002/adma.200390108

Vayssieres, L., Keis, K., Lindquist, S.-E. & Hagfeldt, A. 2001 'Purpose-Built Anisotropic Metal Oxide Material: 3D Highly Oriented Microrod Array of ZnO'. *The Journal of Physical Chemistry B,* 105, 3350-3352, doi: https://doi.org/10.1021/jp010026s

Vergés, M. A., Mifsud, A. & Serna, C. J. 1990 'Formation of rod-like zinc oxide microcrystals in homogeneous solutions'. *J. Chem. Soc., Faraday Trans.,* 86, 959-963, doi: https://doi.org/10.1039/ft9908600959

Vesper, S. J. 1987 'Production of Pili (Fimbriae) by Pseudomonas fluorescens and Correlation with Attachment to Corn Roots'. *Appl Environ Microbiol,* 53, 1397-405, doi: https://doi.org/10.1128/aem.53.7.1397-1405.1987

Wagner, P., Hegner, M., Guentherodt, H.-J. & Semenza, G. 2002 'Formation and in Situ Modification of Monolayers Chemisorbed on Ultraflat Template-Stripped Gold Surfaces'. *Langmuir,* 11, 3867-3875, doi: https://doi.org/10.1021/la00010a043

Wahab, R., Ansari, S. G., Kim, Y.-S., Seo, H.-K. & Shin, H.-S. 2007 'Room temperature synthesis of needle-shaped ZnO nanorods via sonochemical method'. *Applied Surface Science,* 253, 7622-7626, doi: https://doi.org/10.1016/j.apsusc.2007.03.060

Waheed, S., Cabot, J. M., Macdonald, N. P., Lewis, T., Guijt, R. M., Paull, B. & Breadmore, M. C. 2016 '3D printed microfluidic devices: enablers and barriers'. *Lab Chip,* 16, 1993-2013, doi: https://doi.org/10.1039/c6lc00284f

Wang, H., Cai, L., Li, Y., Xu, X. & Zhou, G. 2018 'Biofilm formation by meat-borne Pseudomonas fluorescens on stainless steel and its resistance to disinfectants'. *Food Control,* 91, 397-403, doi: https://doi.org/10.1016/j.foodcont.2018.04.035

Wang, J. & Gao, L. 2003 'Wet chemical synthesis of ultralong and straight single-crystalline ZnO nanowires and their excellent UV emission properties'. *Journal of Materials Chemistry,* 13, doi: https://doi.org/10.1039/b307565f

Wang, X., Ma, X., Church, J., Jung, S., Son, Y., Lee, W. H. & Cho, H. J. 2017 'ZnO nanoflakes as a template for in-situ electrodeposition of nanostructured cobalt electrodes as amperometric phosphate sensors'. *Materials Letters,* 192, 107-110, doi: https://doi.org/10.1016/j.matlet.2016.12.047

Wang, Y., Da Silva Domingues, J. F., Subbiahdoss, G., Van Der Mei, H. C., Busscher, H. J. & Libera, M. 2014 'Conditions of lateral surface confinement that promote tissue-cell integration and inhibit biofilm growth'. *Biomaterials,* 35, 5446-52, doi: https://doi.org/10.1016/j.biomaterials.2014.03.057

Wang, Z. L. 2004 'Zinc oxide nanostructures: growth, properties and applications'. *Journal of Physics: Condensed Matter,* 16, R829-R858, doi: https://doi.org/10.1088/0953-8984/16/25/r01

Wang, Z. L. 2008 'Splendid one-dimensional nanostructures of zinc oxide: a new nanomaterial family for nanotechnology'. *ACS Nano,* 2, 1987-92, doi: https://doi.org/10.1021/nn800631r

Wei, T., Tang, Z., Yu, Q. & Chen, H. 2017 'Smart Antibacterial Surfaces with Switchable Bacteria-Killing and Bacteria-Releasing Capabilities'. *ACS Appl Mater Interfaces,* 9, 37511-37523, doi: https://doi.org/10.1021/acsami.7b13565

Weisse, S., Heydt, M., Maier, T., Schulz, S., Spatz, J. P., Grunze, M., Haraszti, T. & Rosenhahn, A. 2011 'Flow conditions in the vicinity of microstructured interfaces studied by holography and implications for the assembly of artificial actin networks'. *Phys Chem Chem Phys,* 13, 13395-402, doi: https://doi.org/10.1039/c1cp20153k

Whitfield, C. & Trent, M. S. 2014 'Biosynthesis and export of bacterial lipopolysaccharides'. *Annu Rev Biochem,* 83, 99-128, doi: https://doi.org/10.1146/annurev-biochem-060713-035600

Wu, S., Zhang, B., Liu, Y., Suo, X. & Li, H. 2018 'Influence of surface topography on bacterial adhesion: A review (Review)'. *Biointerphases,* 13, 060801, doi: https://doi.org/10.1116/1.5054057

Wu, W. I., Rezai, P., Hsu, H. H. & Selvaganapathy, P. R. 2013 Materials and methods for the microfabrication of microfluidic biomedical devices. *Microfluidic Devices for Biomedical Applications.*

Yang, H., Wang, S., Li, C. & Li, H. 2021 'Three-Dimensional Numerical Simulations and Antifouling Mechanism of Microorganisms on Microstructured Surfaces'. *Processes,* 9, doi: https://doi.org/10.3390/pr9020319

Yang, J., Bos, R., Belder, G. F., Engel, J. & Busscher, H. J. 1999 'Deposition of Oral Bacteria and Polystyrene Particles to Quartz and Dental Enamel in a Parallel Plate and Stagnation Point Flow Chamber'. *J Colloid Interface Sci,* 220, 410-418, doi: https://doi.org/10.1006/jcis.1999.6539

Yu, L., Guo, F., Liu, S., Yang, B., Jiang, Y., Qi, L. & Fan, X. 2016 'Both oxygen vacancies defects and porosity facilitated NO2 gas sensing response in 2D ZnO nanowalls at room temperature'. *Journal of Alloys and Compounds,* 682, 352-356, doi: https://doi.org/10.1016/j.jallcom.2016.05.053

Yu, Q., Wu, Z. & Chen, H. 2015 'Dual-function antibacterial surfaces for biomedical applications'. *Acta Biomater,* 16, 1-13, doi: https://doi.org/10.1016/j.actbio.2015.01.018

Zhang, Y., Ram, M. K., Stefanakos, E. K. & Goswami, D. Y. 2012 'Synthesis, Characterization, and Applications of ZnO Nanowires'. *Journal of Nanomaterials,* 2012, 1-22, doi: https://doi.org/10.1155/2012/624520

Zhong, L., Song, Y. & Zhou, S. 2020 'The Effectiveness of Nafion-Coated Stainless Steel Surfaces for Inhibiting Bacillus Subtilis Biofilm Formation'. *Applied Sciences,* 10, doi: https://doi.org/10.3390/app10145001

Zhu, Z., Andelman, T., Yin, M., Chen, T.-L., Ehrlich, S. N., O'brien, S. P. & Osgood, R. M. 2005 'Synchrotron x-ray scattering of ZnO nanorods: Periodic ordering and lattice size'. *Journal of Materials Research,* 20, 1033-1041, doi: https://doi.org/10.1557/jmr.2005.0134

7   List of Publications and Conference Contributions

Publications in connection with the doctorate:

- <u>Jan David Schutter</u>, Ievgeniia Topolniak, Ozlem Ozcan, "Microhydrodynamic Effects of 3D Microstructured Surfaces on Bacterial Attachment Behavior", *in preparation*.

- Anna Macková, Petr Malinský, Adéla Jagerová, Romana Mikšová, Ondrej Lalik, Pavla Nekvindová, Jan Mistrík, Petr Marvan, Zdenek Sofer, Václav Holý, <u>Jan David Schutter</u>, Ulrich Kentsch, Alexander Azarov and Augustinas Galeckas, 2022, "Energetic Au ion beam implantation of ZnO nanopillars for optical response modulation", *Journal of Physics D: Applied Physics,* 55, doi: 10.1088/1361-6463/ac5486

- <u>Jan David Schutter</u>, Karl Eberhardt, Anna Maria Elert, Jörg Radnik, Daniel Geißler, Ozlem Ozcan, 2023, "Synthesis and Characterization of Lipopolysaccharide (LPS) Anchored Polystyrene Microparticles as a Synthetic Model System for Attachment Studies", *Colloids and Surfaces B: Biointerfaces,* 226, doi: 10.1016/j.colsurfb.2023.113301
    - Part III of this thesis based on the preceding scientific journal publication and sections have been adopted.

Further publications:

- Macková, A. Jagerová, O. Lalik, R. Mikšová, J. Mistrík, D. Poustka, V. Holý, <u>J. D. Schutter</u>, U. Kentsch, A. Azarov, A. Galeckas, 2023"Combined Au/Ag nanoparticle creation in ZnO nanopillars by ion implantation for optical response modulation and photocatalysis", *Applied Surface Science,* 610, doi: 10.1016/j.apsusc.2022.155556

- Maren Erdmann, Sherin Kleinbub, Volker Wachtendorf, <u>Jan David Schutter</u>, Ute Niebergall, Martin Böhning, Andrea Koerdt, 2020 "Photo-oxidation of PE-HD affecting polymer/fuel interaction and bacterial attachment",*npj Materials Degradation*, 4(1), doi: 10.1038/s41529-020-0122-1

- Nina Wurzler, <u>Jan D. Schutter</u>, Ralph Wagner, Matthias Dimper, Vasile-Dan Hodoroaba, Dirk Lützenkirchen-Hecht, Ozlem Ozcan, 2020, "Preconditioning of AISI 304 stainless steel surfaces in the presence of flavins—Part II: Effect on biofilm formation and

microbially influenced corrosion processes", *Materials and Corrosion*, 72(6), doi: 10.1002/maco.202012192

- Nina Wurzler, Jan David Schutter, Ralph Wagner, Matthias Dimper, Dirk Lützenkirchen-Hecht , Ozlem Ozcan, 2020, "Abundance of Fe(III) during cultivation affects the microbiologically influenced corrosion (MIC) behaviour of iron reducing bacteria *Shewanella putrefaciens*", *Corrosion Science*, 174, doi: 10.1016/j.corsci.2020.108855

- Nina Wurzler , Jan David Schutter, Ralph Wagner, Matthias Dimper, Dirk Lützenkirchen-Hecht, Ozlem Ozcan, 2020, "Trained to corrode: Cultivation in the presence of Fe(III) increases the electrochemical activity of iron reducing bacteria – An in situ electrochemical XANES study", *Electrochemistry Communications*, 112, doi: 10.1016/j.elecom.2020.106673

Conference presentations:

- Jan David Schutter, Franziska Pietsch, Frank Schreiber, Andrea Koerdt, Ozlem Ozcan, "Effect of Surface Topography and Chemistry on the Attachment of Bacteria on Solid Surfaces", *EUROCORR 9.–13.9 2019, Sevilla, Spain.*

- Jan David Schutter, Matthias Schenderlein, Brian Pauw, Ozlem Ozcan, "Role of Surface Chemistry and Topography on the Bacterial Adhesion on Solid Surfaces", *ECASIA 15.– 20.9. 2019, Dresden, Germany*

8 Appendix

8.1 Technical Drawings
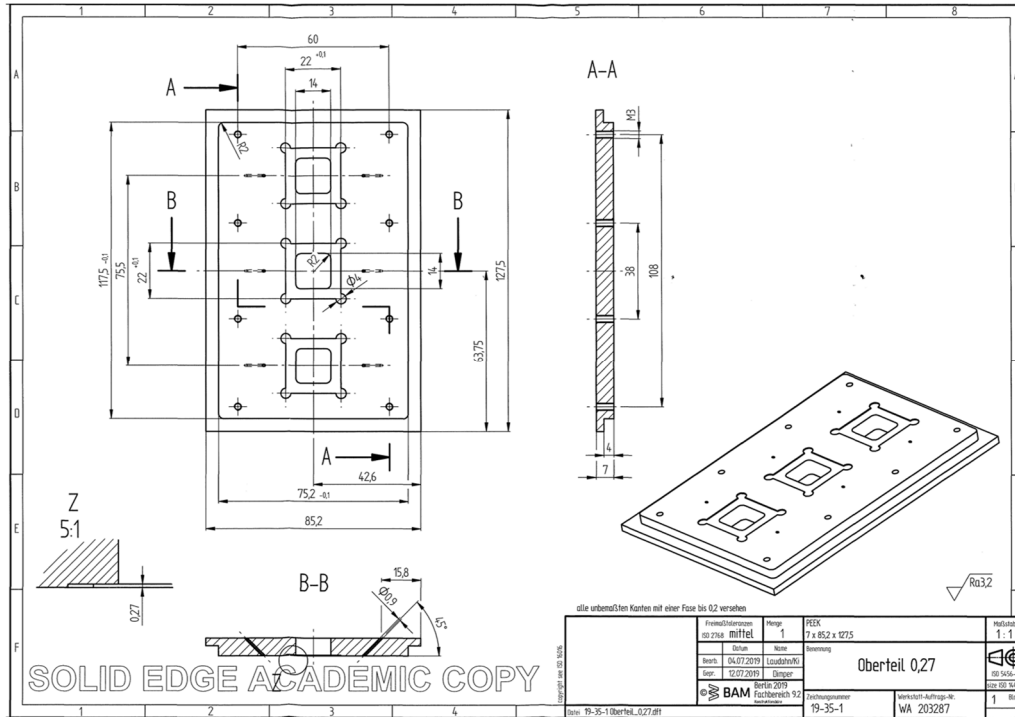
Figure 8-1: Technical drawing of the main component of the flow chamber.
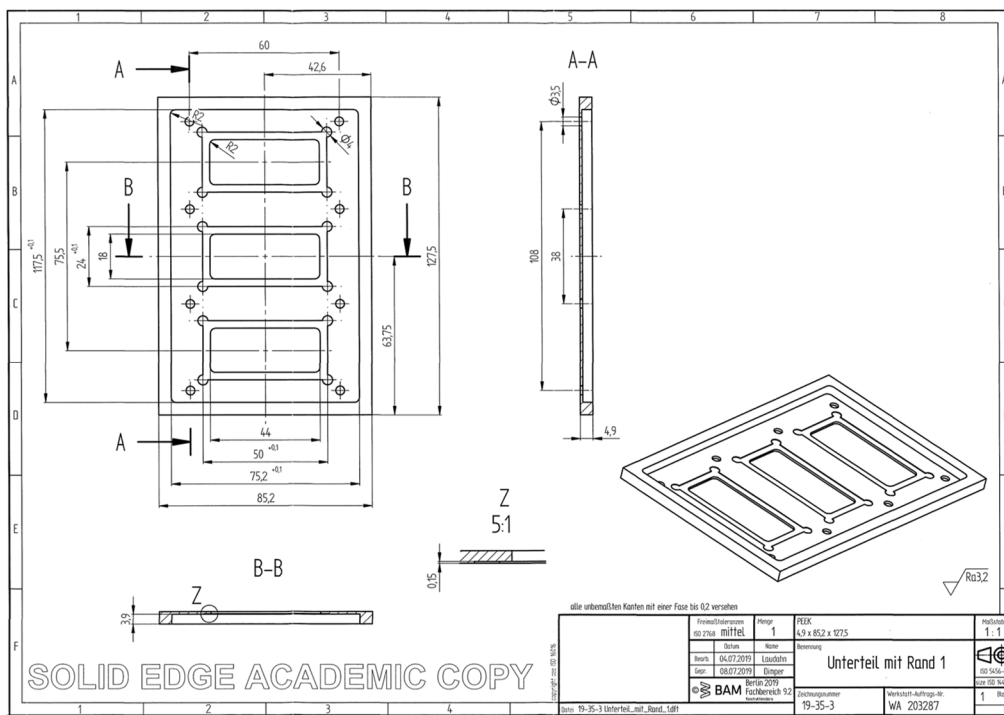
Figure 8-2: Technical drawing of the frame of the flow chamber. The frame can be mounted on the main component. However, it was not used in the final version of the flow chamber since a satisfactory sealing of the flow channels was not possible.
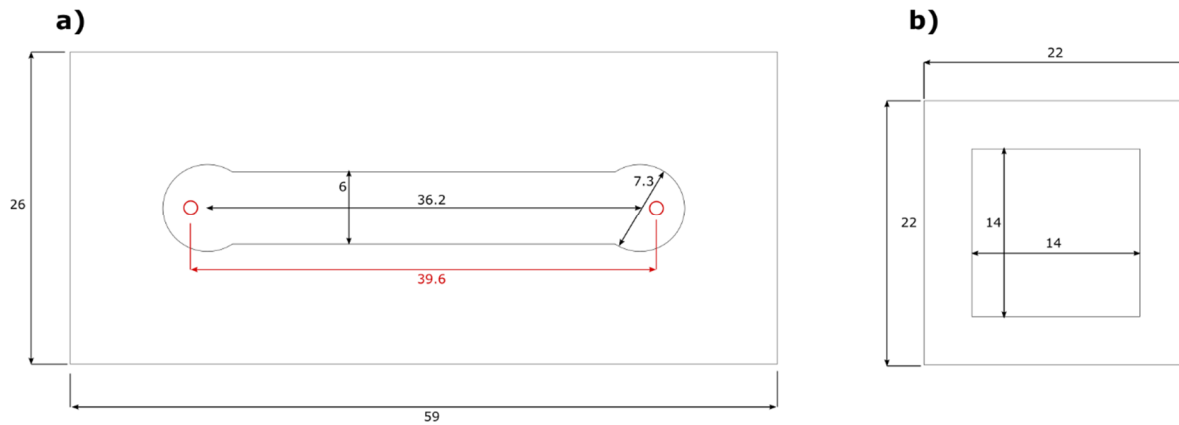
Figure 8-3: Channel element for laser cutter template (a). The red circles are the inlet and outlet position of the flow chamber main component and were not included in the final template. The template was composed of 36 single channel elements. Sealing for the top coverslip (b). The cutting lines should have a thickness of 0.1 pt in the pdf file. An Elastosil film on PET foil of DIN A4 dimensions was cut out. All dimensions are in mm.

8.2 ImageJ Macro Script

```
// for Fiji 1.53c, IJ1 Macro Language, save as .ijm file, import 16-bit greyscale tif-image-stacks with
Plugins>Bio-Formats>Bio-Formats-Importer

macro "mask count" {
    print("---------");
    setBatchMode(false);
    bmode = false;                          //batch mode(true) runs much faster, however no observation is
                                            possible
    Idimension = (1/(211.2*211.2))*1000000.0; //Reciprocal of single image dimension in µm x µm converted to
                                            mm^2
    borderwidth = 5;                        //Half of the border region width in px, 9.67 pixel/µm 5 pixel
                                            approximatly 0.5 µm
    allStackTitles=newArray(nImages+1);     //Create an array of the size depending on opened windows+1
    nStacks=0;
    for (i=1; i<=nImages; i++) {            //This loop fills the array allStackTitles with the names of
                                               the opened stack windows.
        if (nSlices>1) {                    //it will be later needed for choosing the correct image
            selectImage(i);
            allStackTitles[nStacks]=getTitle();
            nStacks++;
        }
    }
    allStackTitles[nStacks] = "none";           //Adds a "none" to allStackTitles and thus a corresponding
                                                selection option.
    if (nStacks <1){ exit("No Stack Window Open")}; //Checks if at least one proper stack window exists
    cropname = split(allStackTitles[0], "_");    //Creates an array to split the long names of the stack
                                                windows into parts - used for saving output later

    Dialog.create("Select count image and mask-image");    //Creates and opens a prompt to choose the correct
                                                stack-window and some options
    Dialog.addChoice("count image stack", allStackTitles)
    Dialog.addChoice("mask image stack", allStackTitles, allStackTitles[allStackTitles.length-1])
    if(lengthOf(cropname) >= 4) {
        Dialog.addString("Output-file", cropname[0] + "_" + cropname[1] + "_"  + cropname[2] + "_" +
cropname[3] + ".txt",30)
    }
    else{Dialog.addString("Output-file", cropname[0]  + ".txt",25)}
    Dialog.addCheckbox("Process with Find Maxima", false); //if checked another function will be  evoked
                                                later, which deals with additional UV-channel stack image
    Dialog.show()
    countfile = Dialog.getChoice();      //countfile = image stack window of the bacteria/fluorescence channel
    maskfile = Dialog.getChoice();              //maskfile = image stack window of the UV channel
    filename = Dialog.getString();          //User defined filename of the output file
    filestring = checkfile(filename);   //Evokes function checkfile and modifies the filename if applicable
    process_type = Dialog.getCheckbox();

    if (countfile == "none") {
        exit("No count image stack was choosen!")
    }
```

```
    if(countfile==maskfile){                    //Checks if the user has accidentally selected the same stack window
                                                       multiple times
        exit("Count image and mask image are the same! Abort now.");
    }


    setBatchMode(bmode);            //Based on the user selection, either functions are called to determine the
                                          cell count per image or the cell count on different substrates
        if(maskfile == "none" && process_type == 0){     // per image or the cell count on different substrates
            print("no mask-file selected. Just count cells on " + countfile);
            count(countfile);                          //count function prepares the images
            process_count("count-stack");         //Total cell count of the bacteria in the prepared image
            }
        if(maskfile == "none" && process_type == 1)
            {
            print("no mask-file selected. Just count cells on " + countfile + " with Find Maxima function");
            count(countfile);
            process_count_maxima("count-stack_maxima");
            }
        else{
            mask(maskfile);                          //mask function prepares the UV channel images
            count(countfile);
            if(process_type == 0){
                process("mask-stack","count-stack");   //Counts bacteria with Analyze Particles function,
                                              better if the bacteria covering area should be determined
                }
            else{
                process_maxima("mask-stack","count-stack_maxima"); //Counts  bacteria  with  Find  Maxima
                                          function, prefered for counting bacteria on different surface types
                }                                          //, more accurate for actual bacterial number
        }
}

function checkfile(arg) {                                    //Checks if the output-file exists and creates in case a
                                          new one with the suffix "-i"
i=1;
file = getDirectory("current") + arg;
while (File.exists(file) == 1) {
        cropstring = split(file, ".");
        file = cropstring[0] + "-" + d2s(i,0) + "." + cropstring[1];
        i++;
        }
        print("new filestring: " + file);
        return file;
}

function getArea() {            //Function to extract the area occupied by bacter after evoking run("Analyze
                                          Particles...")
//selectWindow("Summary of count-stack");            //The window "Summary of count-stack" will be automatically
                                                       created by imageJ, check if it exists
selectWindow("Results");text = getInfo();         //Extracts  the  information  directly  from  the  line  in
                                          "Summary of count-stack"
lines = split(text, "\n");
columns = split(lines[lines.length-1], "\t");
return columns[2];                          //Bacterial area information is stored in second column
}

function mask(arg){                          //Prepares  images  of  the  channel  stack  with  areas  of  different
                                          types and heterogeneity like arrays of ZnO nanorods
    selectWindow(arg);
    getDimensions(mwidth, mheight, mchannels, mslices, mframes); //get informations of the maskfile
    print("process mask");
    run("Select None");                          //repeals any accidantly made selection
    run("Subtract Background...", "rolling=10 sliding stack");
    //run("Multiply...", "value=1.5 stack");    // if necessary, increases the brightness of all images
    run("8-bit");                          // 8-bit is later needed for thresholding
    //setBatchMode(true);            // if the surface was not properly clean sometimes removing outliers
                                          helps
    //run("Remove Outliers...", "radius=10 threshold=10 which=Bright stack");//radius 20 takes maybe to much,
                                                       better radius 10
    //setBatchMode(bmode);
    waitForUser("UV channel has sufficient contrast and brightness for further process?");   //Sometimes
        single images have to be brightend manually: use Multiplication and Gamma for this, can be done while
        promt is open
    run("Select None");

    if (mframes != 1) {     //Bio-Formats put slices into time frame - correction is necessary
        print("switch frames to slices - mask-stack:", arg);
        print("order=xyczt(default) channels=1 "+d2s(mframes,0)+" frames=1 display=Grayscale");
        print("order=xyczt(default) channels=1 slices=" +d2s(mframes,0)+ " frames=1 display=Grayscale");
        run("Stack to Hyperstack...", "order=xyczt(default) channels=1 slices=" +d2s(mframes,0)+ " frames=1
display=Grayscale");
        run("Re-order Hyperstack ...", "channels=[Channels (c)] slices=[Slices (z)] frames=[Slices (z)]");
        run("Hyperstack to Stack");
    }

    waitForUser("Measure threshold?");                //Robust  Automatic  Threshold  needs  a  correct  threshold,
                                          differences might result from image acquisition software of the microscope
    run("Select None");            //Measure threshold with:  select an area in the background, "measure" and
                                          take the stddev
```

```
    Dialog.create("Settings for Robust Automatic Threshold");        //creates  and  opens  a  prompt  for  the
                                                                Robust Automatic Threshold Selection (RATS)
    Dialog.addString("Noise:", "2")
    Dialog.addString("Lambda:", "2")
    Dialog.addString("min Leaf Size:", "1000")
    Dialog.show();
    threshold =  Dialog.getString();
    lambda =  Dialog.getString();
    min =  Dialog.getString();
    ratsettings = "noise=" + threshold + " lambda=" + lambda +" min=" + min;
    print(ratsettings);
    getDimensions(mwidth, mheight, mchannels, mslices, mframes);
    print("new ",arg, " dimensions are (width px , height px, channels, slices, frames):", mwidth, mheight,
mchannels, mslices, mframes);
    for (i = 1; i<=mslices; i++) {              //since RATS cannot process stack, a loop is necessary
        selectWindow(arg);
        setSlice(i);
        run("Robust Automatic Threshold Selection", ratsettings);
        if(i==1){
            rename("mask-stack");
        }
        else {
            slicename = d2s(i, 0) + "-slice";
            rename(slicename);
            run("Concatenate...", "  title=mask-stack image1=mask-stack image2=&slicename"); //"&"    before
                                                        imagename to select the content of "slicename"
        }

    }
    selectWindow("mask-stack");              // in  the  final  mask-stack,  ZnO  nanorods  have  to  be  white,
                                                interspaces have to be black
    print("mask-stack was created");
    run("Select None");
}

function count(arg) {        //Function count prepares the greyscale image stack with bacteria
    selectWindow(arg);
    getDimensions(cwidth, cheight, cchannels, cslices, cframes); //Get informations of the countfile
    print("process count images");
    selectWindow(arg);
    print("cwidth=", cwidth, " cheight=", cheight, " cchannels=", cchannels," cslices=", cslices, " cframes=",
cframes);
    if (cframes != 1) {              //Bio-Formats put slices into time frame - correction is necessary
            print("switch frames to slices - count-stack:", arg);
            run("Stack to Hyperstack...", "order=xyczt(default) channels=1 slices="+d2s(cframes,0)+" frames=1
display=Grayscale");
            run("Re-order  Hyperstack  ...",  "channels=[Channels  (c)]  slices=[Slices  (z)]  frames=[Slices
(z)]");
            run("Hyperstack to Stack");
    }
    getDimensions(cwidth, cheight, cchannels, cslices, cframes);
    print("new ",arg, " dimensions are (width px , height px, channels, slices, frames):", cwidth, cheight,
cchannels, cslices, cframes);

    run("Subtract Background...", "rolling=50 stack");
    run("8-bit");

    if (process_type == 0){          //Process Maxima needs no binarized image, this is for the user defined
                                        function process() working with "Analyse particles"
        waitForUser("Measure threshold?");
        run("Select None");
        Dialog.create("Settings for Robust Automatic Threshold");
        Dialog.addString("Noise:", "2")    // default for mask: Noise5,Lambda2,Min leaf size 1000; for only
                                        count: Noise10 ,Lambda3,Min leaf size 500
        Dialog.addString("Lambda:", "2")
        Dialog.addString("Min. leaf size:", "1000")
        Dialog.show();
        threshold =  Dialog.getString();
        lambda =  Dialog.getString();
        min =  Dialog.getString();
        ratsettings = "noise=" + threshold + " lambda=" + lambda +" min=" + min;
        print(ratsettings);
        for (i = 1; i<=cslices; i++) {
            selectWindow(arg);
            setSlice(i);
            run("Robust Automatic Threshold Selection", ratsettings);
            if(i==1){
                    rename("count-stack");
            }
            else {
                slicename = d2s(i, 0) + "-slice";
                rename(slicename);
                run("Concatenate...",  "    title=count-stack  image1=count-stack  image2=&slicename");//"&"
                            before imagename to select the content of "slicename"
            }

        }
        rename("count-stack");
        print("count-stack was created");
        run("Invert", "stack");
```

```
            waitForUser("OK?");
            selectWindow("count-stack");
            run("Watershed", "stack");           //Separates cells that stick together, needs a black background and
                                                    white bacteria, may cause problems
            selectWindow("count-stack");
            run("Select None");
        }
        else{
            waitForUser("Prepare image stack for Find Maxima function?");//Sometimes single images have to be
                            brightend manually: use Multiplication and Gamma for this, can be done while promt
                            is open
            rename("count-stack_maxima");
            run("Select None");
        }
}

function process_count(argc){                              //If the user choosed no background-area channel, only total
                                            bacteria counting of the bacteria/fluorescence channel will be done
        selectWindow(argc);                               //Selects the bacteria/fluorescence channel image stack
        run("Select None");                               //Repeals all existing selections in the stack
        getDimensions(width, height, channels, slices, frames);
        run("Measure");
        countimageArea = getResult("Area", nResults-1); //Gets the area in px^2 from run("Measure") output
        print("countimageArea (px): " + countimageArea);
        datafile = File.open(filestring);                 //Creates a data output file
        print("datas will be writen in:", filestring);
                print(datafile,"#slicenumber; totalcount; total %Area; bacteria off rods %Area;"); //Comment line
                                                    in the first row in the output file
        for (i = 1; i <= slices; i++) {
            selectWindow(argc);
            setSlice(i);
            run("Analyze Particles...", "size=10-900 circularity=0.20-1.00 show=Nothing display clear summarize
slice");
            totalcount = nResults();      //Total bacteria count from run("Analyze Particles...") stored in variable
            count_totalArea = parseFloat(getArea())/countimageArea*100;           //Percantage  area  which  is
                                                    occupied by bacteria
            print("In slice ", i, " total:", totalcount, " total %Area: ", count_totalArea);
            string = d2s(i, 0) + ";" + d2s(totalcount,0) + ";" +  d2s(count_totalArea,3) + ";" ;
            print(datafile,string);              //Inserts the string above with all results of image i as one row
                                                    into the output data file
        }
        File.close(datafile);
}

function process_count_maxima(argc){      //If the user choosed no background-area channel, only total bacteria
                                    counting of the bacteria/fluorescence will be done with find maxima function
        selectWindow(argc);                               //Selects the bacteria/fluorescence channel image stack
        run("Select None");                               //Repeals all existing selections in the stack
        getDimensions(width, height, channels, slices, frames);
        run("Measure");
        countimageArea = getResult("Area", nResults-1); //Gets the area in px^2 from run("Measure") output
        print("countimageArea (px): " + countimageArea);

        waitForUser("Evaluate the threshold for Find Maxima function");//Evaluate of threshold can be done by
                            evoking and testing the Find Maxima function manually, it has a preview function
        Dialog.create("Type threshold for Find Maxima function");       //Creates a prompt where the user can
                                                    insert the threshold value for the Find Maxima function
        Dialog.addString("threshold","50",5);
        Dialog.show();
        maxima_threshold = Dialog.getString();
        print("Proceed with maxima_threshold: ", maxima_threshold);


        datafile = File.open(filestring);                 //Creates a data output file
        print("datas will be writen in:", filestring);
        print(datafile,"#slicenumber; totalcount; total %Area; bacteria off rods %Area;");       //Comment  line
                                                    in the first row in the output file
        for (i = 1; i <= slices; i++) {
            selectWindow(argc);
            setSlice(i);
            run("Select None");
            run("Find Maxima...", "prominence=" + d2s(maxima_threshold,0) + " output=Count"); //Total bacteria
                                                    count in image i, settings may be adapted
            totalcount = parseFloat(getResult("Count", nResults-1));      //Total bacteria count from run("Find
                                                    Maxima...") stored in variable
            count_totalArea = parseFloat(getArea())/countimageArea*100; //Percantage area which is occupied by
                                        bacteria – however not realiable in combination with "Find Maximu" function
            print("In slice ", i, " total:", totalcount, " total %Area: ", count_totalArea);
            string = d2s(i, 0) + ";" + d2s(totalcount,0) + ";" +  d2s(count_totalArea,3) + ";" ;
            print(datafile,string);       //Inserts the string above with all results of image i as one row into the
                                        output data file
        }
        File.close(datafile);
}


function process(argm,argc){                //Coounts bacteria with Analyze particles if process_type==0, if it
                                        is not checked, no border region will be considered
        selectWindow(argm);                               //Selects the UV channel image stack
        run("Select None");                               //Repeals all existing selections in the stack
```

```
    getDimensions(width, height, channels, slices, frames); //Gets stack properties for later calculations
    run("Measure");
    maskArea = getResult("Area", nResults-1);        //Gets the area in px^2 from run("Measure") output
    print("properties of mask-stack: width = ", width, " px, height =", height, " px, channels =", channels,
", slices =", slices, ", frames = ", frames);
    print("maskArea (px):", maskArea);
    selectWindow(argc);                              //Selects the bacteria/fluorescence channel image stack
    run("Select None");
    run("Measure");
    countimageArea = getResult("Area", nResults-1); //Gets the area in px^2 from run("Measure") output
    datafile = File.open(filestring);               //Creates a data output file
    print("datas will be writen in:", filestring);
    print(datafile,"#slicenumber; totalcount; bacteria on rods; bacteria between rods; bacteria total %Area;
bacteria on rods %Area; bacteria off rods %Area; Fraction MaskArea; Fraction Interspace Area; normalized
baceria on rods; normalized bacteria off rods"); //Comment line in the first row in the output file
        for (i = 1; i <= slices; i++) {            //Loop for counting bacteria on each image
            selectWindow(argc);
            setSlice(i);
            run("Analyze  Particles...",  "size=10-900  circularity=0.20-1.00  show=Nothing  display  clear
summarize slice");  //Total bacteria count in image i, settings may be adapted
            totalcount = nResults();                //Stores output of run("Analyze particles...") in variable
            count_totalArea = parseFloat(getArea())/countimageArea*100; //Percantage area which is occupied
                                                        by bacteria

            selectWindow(argm);
            setSlice(i);
                run("Create Selection");  //Creates a mask selection of ZnO nanorod array in image i of the
                                UV stack
                run("Measure");
                MaskArea_fraction = parseFloat(getResult("Area", nResults-1))/(maskArea);   //Gets the ZnO
                                nanorod array area in px^2 from run("Measure") output
                run("Make Inverse");                //Inverses the selection to create a mask selection of the
                                interspace area
                run("Measure");
                VoidArea_fraction  =  parseFloat(getResult("Area",  nResults-1))/(maskArea);  //Gets  the
                                interspace area in px^2 from run("Measure") output

            selectWindow(argc);
                run("Restore Selection");           //Transfers the mask selection of the interspace area to
                                bacteria/fluorescence channel of the same image i
                run("Analyze  Particles...",  "size=10-900  circularity=0.2-1.00  show=Nothing  display  clear
summarize slice"); //Bacteria count in the interspaces
                bacoffrods = nResults();            //Stores output of run("Analyze particles..." in variable
                    bacoffrodsArea = parseFloat(getArea())/countimageArea*100; //Percantage area which
                                is occupied by bacteria in interspaces
                normalized_bacoffrods = bacoffrods/VoidArea_fraction;       //Normalizes the counted cells in
                                the interspace to mm^2
                baconrods = totalcount-bacoffrods;  //Calculates the bacteria count on the ZnO nanorods
                baconrodsArea = count_totalArea-bacoffrodsArea;     //Calculates the percantage area which is
                                occupied by bacteria on the ZnO nanorods
                normalized_baconrods = baconrods/MaskArea_fraction; //Calculate the cell caount on the ZnO
                                nanorods and normalizes to mm^2

            print("In slice ", i, " total:", totalcount, ", bacteria on rods:", baconrods,", bacteria off
rods:",  bacoffrods, " \n total %Area: ", count_totalArea, " bacteria on rods %Area: ", baconrodsArea, "
bacteria off rods %Area: ", bacoffrodsArea, " \n Fraction MaskArea :", MaskArea_fraction, "Fraction Interspace
Area", VoidArea_fraction );
            string = d2s(i, 0) + ";" + d2s(totalcount,0) + ";" + d2s(baconrods,0) + ";" + d2s(bacoffrods,0)
+";"  +  d2s(count_totalArea,3)  +  ";"  +  d2s(baconrodsArea,3)  +  ";"  +  d2s(bacoffrodsArea,3)  +  ";"  +
d2s(MaskArea_fraction,3)  +  ";"  +  d2s(VoidArea_fraction,3)  +   ";"  +  d2s(normalized_baconrods,0)  +  ";"  +
d2s(normalized_bacoffrods,0);
            print(datafile,string);             //Inserts the string above with all results of image i as one row
                                into the output data file
        }
        File.close(datafile);
}

function process_maxima(argm,argc){         //Coounts bacteria if process_type==1, if it is checked, a border
                                region will be considered
    selectWindow(argm);                              //Selects the UV channel image stack
    run("Select None");                              //Repeals all existing selections in the stack
    getDimensions(width, height, channels, slices, frames); //Gets stack properties for later calculations
    run("Measure");
    maskArea = getResult("Area", nResults-1);        //Gets the area in px^2 from run("Measure") output
    print("properties of mask-stack: width = ", width, " px, height =", height, " px, channels =", channels,
", slices =", slices, ", frames = ", frames);
    print("maskArea (px):", maskArea);
    selectWindow(argc);                              //Selects the bacteria/fluorescence channel image stack
    run("Select None");
    run("Measure");
    countimageArea = getResult("Area", nResults-1); //Gets the area in px^2 from run("Measure") output
    waitForUser("Evaluate the threshold for Find Maxima function"); //Evaluate of threshold can be done by
                    evoking and testing the Find Maxima function manually, it has a preview function
    Dialog.create("Type threshold for Find Maxima function");//Creates a prompt where the user can insert the
                                            threshold value for the Find Maxima function
    Dialog.addString("threshold","55",5);
    Dialog.show();
    maxima_threshold = Dialog.getString();
    print("Proceed with maxima_threshold: ", maxima_threshold);
    datafile = File.open(filestring);               //Creates a data output file
```

```
    print("datas will be writen in:", filestring);
    print(datafile,"#slicenumber; totalcount; bacteria on rods; fraction bacteria on rods; bacteria between
rods; fraction bacteria between rods; bacteria on borders; fraction bacteria on borders; fraction MaskArea;
fraction Interspace Area; fraction Border Area; normalized baceria on rods; normalized per Area baceria on
rods; normalized bacteria off rods; normalized per Area baceria off rods; normalized bacteria on border;
normalized per Area baceria on border"); //Comment line in the first row in the output file
    for (i = 1; i <= slices; i++) {                    //Loop for counting bacteria on each image
        selectWindow(argc);
        setSlice(i);
        run("Select None");
        run("Find Maxima...", "prominence=" + d2s(maxima_threshold,0) + " output=Count"); //Total bacteria
                                                 count in image i, settings may be adapted
        totalcount = parseFloat(getResult("Count", nResults-1));    //Stores output of run("Find Maxima...")
                                                 in variable

        selectWindow(argm);
        setSlice(i);
            run("Create Selection");        //Creates a mask selection of ZnO nanorod array in image i of the
                                             UV stack
            run("Make Inverse");  //Make Inverse two times in order to avoid image edge selection effects
            run("Enlarge...", "enlarge=" + d2s(borderwidth,0)); //Includes border region in selection
            run("Make Inverse");
            run("Measure");
            MaskArea_fraction = parseFloat(getResult("Area", nResults-1))/(maskArea); //Gets the ZnO  nanord
                                             array area in px^2 from run("Measure") output

        selectWindow(argc);                              //Select image i of bacteria/fluorescence channel
            run("Restore Selection");               //Transfers the mask selection of the UV channel area to
                                             bacteria/fluorescence channel of the same image i
            run("Find Maxima...", "prominence=" + d2s(maxima_threshold,0) + " output=Count");
                                             //Bacteria count on ZnO nanord arrays minus border region
            baconrods = parseFloat(getResult("Count", nResults-1)); //Stores output of run("Find Maxima...")
                                                 in variable
            normalized_baconrods = baconrods/MaskArea_fraction;     //Normalizes the counted cells on the ZnO
                                             nanorod arrays to mm^2

        selectWindow(argm);                          //Switch back to UV channel stack image i
            run("Create Selection");      //Creates a mask selection of interspace in image i of the UV stack
            run("Enlarge...", "enlarge=" + d2s(borderwidth,0)); //Includes border region in selection
            run("Make Inverse");
            run("Measure");
            VoidArea_fraction = parseFloat(getResult("Area", nResults-1))/(maskArea);        //Gets      the
                                             interspace area in px^2 from run("Measure") output

        selectWindow(argc);
            run("Restore Selection");       //Transfers  the  mask  selection  of  the  UV  channel  area  to
                                             bacteria/fluorescence channel of the same image i
            run("Find Maxima...", "prominence=" + d2s(maxima_threshold,0) + " output=Count");
            bacoffrods = parseFloat(getResult("Count", nResults-1));      //Bacteria    count    in    the
                                             interspace minus border region
            normalized_bacoffrods = bacoffrods/VoidArea_fraction;  //Normalizes  the  counted  cells  in  the
                                             interspace to mm^2
        baconborder = totalcount-baconrods-bacoffrods; //Calculates the bacteria count in the border region
        border_fraction = 1-VoidArea_fraction-MaskArea_fraction;    //calculates the area of the border region
                                             for normalization
        normalized_baconborder = baconborder/border_fraction;        //Normalizes  the  counted  cells  in  the
                                             border regioin to mm^2
        print("In slice ", i, " total:", totalcount, ", bacteria on rods:", baconrods,", bacteria off rods:",
bacoffrods, ", bacteria on border:", baconborder, " \n Fraction MaskArea :", MaskArea_fraction, "Fraction
Interspace Area", VoidArea_fraction );
        string  =  d2s(i,  0)  +  ";"  +  d2s(totalcount,0)  +    ";"  +  d2s(baconrods,0)  +   ";"  +
d2s(baconrods/totalcount,3)  +  ";"  +  d2s(bacoffrods,0)  +  ";"  +  d2s(bacoffrods/totalcount,3)  +  ";"  +
d2s(baconborder,0)   +   ";"   +   d2s(baconborder/totalcount,3)   +   ";"   +   d2s(MaskArea_fraction,3)   +   ";"   +
d2s(VoidArea_fraction,3)  +   ";"  +  d2s(border_fraction,3)  +   ";"  +  d2s(normalized_baconrods,0)  +  ";"  +
d2s(normalized_baconrods*Idimension,0)      +      ";"      +      d2s(normalized_bacoffrods,0)      +      ";"      +
d2s(normalized_bacoffrods*Idimension,0)     +      ";"      +      d2s(normalized_baconborder,0)      +      ";"      +
d2s(normalized_baconborder*Idimension,0);
        print(datafile,string);  //Inserts the string above with all results of image i as one row into the
                                 output data file
    }
    File.close(datafile);
}
```